To the Graduate Council:

I am submitting herewith a dissertation written by Darnell Carlton Worley II entitled "Damage Assessment and Progression in a Polyisocyanurate Based Continuous Swirl Mat Composite." I have examined the final copy of this dissertation for form and content and recommend that it be accepted in partial fulfillment of the requirements for the degree of Doctor of Philosophy, with a major in Polymer Engineering.

Roberto Benson

Roberto S. Benson, Major Professor

We have read this dissertation
and recommend its acceptance:

John D. Landes

John D. Landes

Jack F. Fellers

Jack F. Fellers

Peter K. Liaw

Peter K. Liaw

Kevin Kit

Kevin Kit

Accepted for the Council:

Associate Vice Chancellor and
Dean of the Graduate School

Damage Assessment and Progression in a Polyisocyanurate Based Continuous Swirl Mat Composite

A Dissertation
Presented for the
Doctor of Philosophy Degree
The University of Tennessee, Knoxville

Darnell Carlton Worley II
May 1999

To My Family

The times in life when the world seems to be against you and the hopes for tomorrow seem to fade with every passing thought are often met by the things and events in life that we cherish most, for me it is my God and Family. For no one can give us the unconditional love that God has given through his Son's death and resurrection, however, he has given us a glimpse of love like the love that a wife ***chooses*** to give her husband or the love that comes from the one who nurtured you before you knew you were you. What about the kind of love an elder brother, who on no choosing of his own, gives up his youth to take on the responsibility a father should have? Or what about the love from sisters? The older ones love you like they are your mother while the younger one gives you the respect a father earns from his devotion to her. However, the love that comes from nephews and nieces is different because they yearn for your attention, much like a child running for a parent when being lost comes to an end. Was it I that said the world seemed to be against me? No, that was just a passing thought.

Wife:	**Erika A. Worley**
Mother:	**Mitzi M. (Heibel) Worley**
Brother:	**Joe Worley**
Sisters:	**Nita F. Worley**
	Shelah R. (Worley) Lyles
	Donna E. Worley (Candy)
Nephews:	**Larnell Worley**
	Tory Worley
	James D. Hockett
	Amir Worley
Niece:	**Ashton Nicole Amaba**
	Brianna Amaba
	Aleyah Lyles
Sister (2)	**Eileen A. Amaba**

I LOVE YOU ALL…

ACKNOWLEDGMENTS

Durability of Lightweight Composite Structures Project is sponsored by the U.S. Department of Energy's (DOE's) Lightweight Materials Program. The project at ORNL is part of a cooperative effort between DOE and the Automotive Materials Partnership of the United States Council for Automotive Research (USCAR). The project is being coordinated with the Automotive Composites Consortium (ACC). DOE opened a subcontract with the University of Tennessee to participate in the development of this material.

I would like to thank Dr. Jim Corum for his support in this work as well as Dr. William Simpson Jr. I would like to also thank Mike Neal, Stephen Steiner, Gregory L. Jones, Doug Fielden, Larry Smith, Raymond Bellamy, Sandra Maples and Carla Lawrence. I would also like to thank my professors Roberto S. Benson, John F. Fellers, John Landes, Peter Liaw, Paul J. Phillips, Donald Bogue, Kevin Kit and Spiro Alexandratos who have provided an opportunity to grow as an engineer.

ABSTRACT

This research conducted in conjunction with Oak Ridge National Laboratories and the Automotive Composite Consortium, ACC, was motivated by the desire to reduce vehicle weight for increased efficiency. At present, there are no databases of failure mechanisms, experimental procedures to study failure, mathematical expressions for empirical or theoretical prediction of properties of a continuous swirl mat composite, CSMC. Therefore, to contribute to the increased utilization of this class of materials the following research was performed. This research enabled the failure mechanism to be formulated, development of a method to quantify failure based on ultrasonic attenuation maps, and the prediction of the fracture toughness parameter K_{IC}.

The use of scanning electron microscopy, light microscopy, and real-time tensile loading showed that the CSMC failed in a brittle mode. These techniques also provided imaging information as to how a dominant crack propagates in the presence of a continuously swirled E-glass mat reinforcement and voids. This evaluation enabled a reconstruction of failure in order to demonstrate a possible failure mechanism. The aforementioned techniques revealed that the dominant crack follows the fiber/matrix interface, but may be influenced by the presence of voids. Voids have the tendency of luring the growing crack away from the interface. A growing crack would, however, return to a fiber/matrix interface until complete failure occurred.

Another aspect of this work was the quantification of progressive damage using ultrasound. Comparisons were made between ultrasonic attenuation maps for unloaded and sequentially loaded specimens. The sequential loads were applied at different

percentages of the ultimate tensile strength, UTS. This technique provided attenuation maps for a series of specimens with a controlled degree of damage, which showed an increase in attenuation with an increase in percent UTS.

Fracture toughness experiments yielded an average K_{IC} value of 17.1 MPa$\sqrt{m}$, while the prediction of the fracture toughness parameter, K_{IC}, was achieved by combining K-solution expressions for in-line and parallel crack configurations while evaluating the needed stress, σ, using of the "Rule of Mixtures". The average void length was used as the crack length, which was obtained by light microscopy in conjunction with NIH™ software. The predicted K_{IC} value at 40% glass fiber and void orientations of 45°, 30° and 25° was 11.4 MPa$\sqrt{m}$, 17.0 MPa$\sqrt{m}$ and 18.6 MPa$\sqrt{m}$, respectively.

TABLE OF CONTENTS

I. INTRODUCTION *1*

II STATEMENT OF THE PROBLEM *3*

III HYPOTHESIS *4*

IV. BACKGROUND *5*

4.1 Introduction to Composites 5
4.1.1 Composites 5

4.2 Fiber Reinforced Composites 7
4.2.1 Glass Fiber 7
4.2.2 Glass Fiber Fabrication 11
4.2.3 Polymer Matrix 12
4.2.4 Composite Interface 12
4.2.5 Mechanical Response of Composites 15

4.3 Composite Fabrication Techniques 20

4.4 Composites and Damage 23
4.4.1 Damage Associated with Composites 23
4.4.2 Continuous Swirl Mat Composites 29

4.5 Damage Assessment Techniques 35
4.5.1 Ultrasonic C-Scan 35
4.5.2 Light-Transmission Microscopy 42

4.6 Scanning Electron Microscopy 43

4.7 Image Analysis 45

V. THEORETICAL AND EMPIRICAL APPROACHES *48*

5.1 Mathematics of Material Failure 48
5.1.1 Rule of Mixture 48
5.1.2 Fracture Mechanics 50
5.1.3 Linear Elastic Fracture 52
5.1.4 K-Solutions 60

VI. EXPERIMENTAL *61*

6.1 Sample Preparation 61

6.2 Testing 61
6.2.1 Ultrasound 61
6.2.2 Image Analysis 62
6.2.3 Tensile Loading 62
6.2.4 Horizontal Hydraulic Tensile Tester 63
6.2.5 Creep Loading 63
6.2.6 Fatigue 63
6.2.7 Fracture Toughness 65
6.2.8 Void Volume 65

VII. RESULTS *67*

7.1 Mechanical Properties 67
7.1.1 Tensile 67
7.1.2 Creep 67
7.1.3 Fatigue Tests 71

7.2 Ultrasound 73
7.2.1 Ultrasonic C-scan for Tensile specimens 73

7.3 Image Analysis 73
7.3.1 Image Analysis and SEM 79
7.3.2 Image Analysis and Real-time observation 83

7.4 Failure Mechanism 91

7.5 Void Volume 91

7.6 Mathematics of Fracture Toughness 92
7.6.1 Evaluation of Applied Stress 92

7.7 Mathematical Approach to Fracture Toughness, K_{IC} 95

7.8 Experimental Results of Fracture Toughness 97

VIII. DISCUSSION ***109***

8.1 Mechanical Response and Damage Assessment and Progression 109

8.2 Mechanistic Approach to CSMC's and Damage 110
8.2.1 Failure Mechanism 114
8.2.2 The Failure Mechanism and SEM 117
8.2.3 Tensile and Creep 118
8.2.4 Fatigue 123

8.3 C-Scans 125
8.3.1 Ultrasound approach to Damage 125
8.3.2 Tensile Mechanical Response 126

8.4 Evaluation of Fracture Toughness 127

8.5 Fracture Toughness Prediction 132

IX. CONCLUSIONS ***138***

X. FUTURE WORK ***139***

REFERENCES ***140***

APPENDIX ***146***

Appendix A 147

Appendix B 155

Appendix C 157

Appendix D 159

VITAE ***161***

LIST OF TABLES

TABLE 1. FIBERS AND THEIR MECHANICAL PROPERTIES. 8

TABLE 2. GLASS FIBER COMPOSITIONS 9

TABLE 3. MECHANICAL PROPERTIES GLASS FIBER. 10

TABLE 4. SIZINGS AND THEIR UTILITY. 14

TABLE 5. VARIATION OF K_{IC} WITH VOID ANGLE 135

LIST OF FIGURES

FIGURE 1. ACCEPTED VIEW OF SIZING INTERACTION WITH FIBER AND MATRIX................ 16

FIGURE 2. DISCREDITED VIEW OF SIZING INTERACTION WITH FIBER AND MATRIX............ 17

FIGURE 3. THREE FIBER ORIENTATIONS USED IN COMPOSITE REINFORCEMENT................. 19

FIGURE 4. SCHEMATIC OF THE RIM PROCESS. 22

FIGURE 5. SCHEMATIC OF BRITTLE FRACTURE BANDS.. 25

FIGURE 6. SCHEMATIC OF FATIGUE CRACK PROPAGATION.. 26

FIGURE 7. GLASS FIBER REINFORCED POLYESTER SHOWING RIVER PATTERN.................... 27

FIGURE 8. COTTON FIBER PHENOL-FORMALDEHYDE, BRITTLE FRACTURE BANDS 28

FIGURE 9. GLASS FIBER REINFORCED POLYESTER, FIBER BREAKAGE AND PULL-OUT 30

FIGURE 10. GLASS FIBER IN POLYCARBONATE, DEBONDING AND FIBER PULL-OUT. 31

FIGURE 11. GLASS FIBER IN POLYCARBONATE, MATRIX DEGRADATION AND DEBONDING.32

FIGURE 12. SCHEMATIC OF ULTRASONIC C-SCAN 37

FIGURE 13. A-SCAN AND C-SCAN OF AREA 1. 39

FIGURE 14. A-SCAN AND C-SCAN OF AREA 2. 40

FIGURE 15. A-SCAN AND C-SCAN OF AREA 3. 41

FIGURE 16. REAL-TIME VIDEO COLLECTION SETUP. 47

FIGURE 17. THE RULE OF MIXTURES AND SYNERGISM.. 49

FIGURE 18. BASIC MODES OF CRACK SURFACE DISPLACEMENT. 51

FIGURE 19. STRESS FIELD AROUND CRACK TIP FOR DIFFERENT LOADING MODES............. 53

FIGURE 20. MODE I LOADING IN AN INFINITE PLATE. 54

FIGURE 21. PLANAR CONDITIONS TO DETERMINE STRESS DISTRIBUTION ABOUT A CRACK TIP. 57

FIGURE 22. HYDRAULIC TENSILE TESTER AND SETUP. 64

FIGURE 23. TYPICAL STRESS-STRAIN CURVE OF A CSMC IN THE 0° DIRECTION. 68

FIGURE 24. MODULUS REDUCTION AS A FUNCTION OF LOAD LEVEL. 69

FIGURE 25. CREEP RESPONSE IN AIR AT ROOM TEMP AND 50% RH. 70

FIGURE 26. MAXIMUM STRAIN VS. CYCLES TO FAILURE. 72

FIGURE 27. OBSERVED DAMAGE USING OPTICAL MICROGRAPHS WITH INCREASING CYCLES. 74

FIGURE 28. REGIONS OF ACCUMULATED DAMAGE WITH INCREASING CYCLES. 75

FIGURE 29. C-SCANS OF INCREMENTAL UTS TENSILE LOADING. 76

FIGURE 30. C-SCANS OF INCREMENTAL TENSILE LOADING. 77

FIGURE 31. PLOT OF AVERAGE GRAYSCALE VALUE, AGV VS. UTS. 78

FIGURE 32. VOIDS AND FIBER BUNDLE. 80

FIGURE 33. THE INCOMPLETE FIBER WETTING AND SIZING GLOBS PRIOR TO PROCESSING. 81

FIGURE 34. THE GLASS MAT PRIOR TO PROCESSING. 82

FIGURE 35. FRACTURE SURFACE TOP VIEW P21-0-25 1.5 KEV, 70X. 84

FIGURE 36. CONTINUATION OF FRACTURE SURFACE IN FIGURE 29 P21-0-25, 70X. 85

FIGURE 37. VOID ON FRACTURE SURFACE P21-0-25, 1.5 KEV, 300X. 86

FIGURE 38. RIVER PATTERN ON FRACTURE SURFACE, P21-0-25, 1.5 KEV 300X. 87

FIGURE 39. INITIAL OBSERVATION OF CRACK FORMATION. 88

FIGURE 40. CONTINUATION OF CRACK GROWTH AND DAMAGE FORMATION. 89

FIGURE 41. CONTINUATION OF CRACK GROWTH AND DAMAGE FORMATION. 90

FIGURE 42. K_{IC} PREDICTED AS A FUNCTION OF FIBER VOLUME FRACTION. 98

FIGURE 43. THREE DIMENSIONAL PLOT WITH A VOID ORIENTATION ANGLE OF 25°. 99

FIGURE 44. THREE DIMENSIONAL PLOT WITH A VOID ORIENTATION ANGLE OF 30°. 100

FIGURE 45. THREE DIMENSIONAL PLOT WITH A VOID ORIENTATION ANGLE OF 45°. 101

FIGURE 46. COMPOSITE PLOT OF 25°, 30° AND 45° VOID ORIENTATIONS. 102

FIGURE 47. THE EFFECT OF VOID VOLUME ON K_{IC} AT A FIBER FRACTION OF 0.2. 103

FIGURE 48. THE EFFECT OF VOID VOLUME ON K_{IC} AT A FIBER FRACTION OF 0.4. 104

FIGURE 49. THE EFFECT OF VOID VOLUME ON K_{IC} AT A FIBER FRACTION OF 0.6. 105

FIGURE 50. THE EFFECT OF VOID VOLUME ON K_{IC} AT A FIBER FRACTION OF 0.8. 106

FIGURE 51. A REPRESENTATIVE LOAD VS. DISPLACEMENT CURVE FOR K_{IC} EVALUATION. 107

FIGURE 52. FIBER ORIENTATION RELATIVE TO APPLIED LOAD. 111

FIGURE 53. SWIRL MAT ORIENTATION SIMPLIFIED. 112

FIGURE 54. FAILURE MECHANISM FOR CSMC. 116

FIGURE 55. CRACK PROPAGATION THROUGH VOIDS AND ALONG BUNDLE. 121

FIGURE 56. THE OPENED CRACK THROUGH VOIDS AND ALONG BUNDLE. 122

FIGURE 57. PARALLEL CRACKS. 129

FIGURE 58. IN-LINE CRACKS 130

FIGURE 59. FRACTURE TOUGHNESS AS A FUNCTION OF FIBER FRACTION, VOID ORIENTATION AND A CONSTANT VOID VOLUME OF 12%. 133

FIGURE 60. COMPARISON OF POLYISOCYANURATE K_{IC} WITH POLYESTER, EPOXY AND PE. 137

I. INTRODUCTION

The polymer composite industry has found its strength in its ability to replace other materials. The composite industry in the mid to late 1990's has out performed the general economy. The United States was expected to make shipments in '97 of 3.42 billion lbs. of composite materials, which is approximately a 6.1% increase from the previous year.[1] It was revealed in Modern Plastics, ***November '97 issue,*** that the increase in growth occurred in transportation, construction, consumer products, and electrical and electronic markets.[2] Composite materials are unique in that they can be tailored for specific application. The tailoring of these materials is a matter of understanding the relationship between fiber properties (reinforcement), polymer properties (matrix), and the interface enabling the interaction between the reinforcement and matrix.

The application of composite materials based on glass and polymer fiber mats are being used in automotive panels, beam fabrication, thin wall veneer panels, and other end products. However, the majority of research performed is on traditional composite materials, that is, uniaxially oriented plies, short and long fibers uniaxially, biaxially, and randomly oriented. Traditional composites have a considerably large knowledge base concerning failure, failure criterion, and predictive tools to measure different mechanical properties. Recent development in the technologies for the formation of fibrous glass and polymer webs and mats have enabled the introduction of nonwoven, continuous strand, and short and long fiber mat composites. These new reinforcement configurations produce materials with unique properties making them suitable for a variety of applications. As the mat composite industry continues to expand, the need for a scientific understanding of this class of composite materials becomes essential for long term success. Therefore, the objective of this research was to study damage formation and progression, experimental techniques applicable to damage assessment, and the development of a mathematical tool to predict the linear elastic fracture parameter, K_{IC}, for Continuous Swirl Mat Composites, CSMC.

II STATEMENT OF THE PROBLEM

The purpose of this research is to determine based on microscopy techniques, the possible mechanism of failure for a continuous swirl mat composite, CSMC. Also, to develop a mathematical approach to evaluate the fracture toughness, K_{IC}, for CSMC, and to advance the use of ultrasonic attenuation as a quantitative tool in the assessment of damage progression. This study was conducted on a polyisocyanurate matrix reinforced with a continuous swirl mat composed of bundles of monofilament E-glass fibers.

III HYPOTHESIS

First, it is hypothesized that damage in the form of fiber debonding, breakage, pullout, and defects (voids) in the CSMC can be observed using microscopy and/or ultrasonic techniques. These techniques provide information concerning the failure mechanism. **Secondly**, Quantification of ultrasonic attenuation maps could be done by using a computer algorithm to calculate the average grayscale value, AGV. It is expected that the AGV decreases with an increase in attenuation for each incrementally loaded specimen. **Finally**, the combining of crack configuration expressions by Tada with modification to account for the presence of voids and void orientation with respect to the loading direction may enabled the prediction of the linear elastic fracture mechanics parameter, K_{IC}.

IV. BACKGROUND

4.1 Introduction to Composites

4.1.1 Composites

Composite materials are defined in general as the combining of two or more materials on the microscopic, molecular or macroscopic scale. A broad definition of what composites are results in a variety of material combinations as well as individual component geometry. Reasons for adding a second or third component to a homogeneous material vary due to application. For example, some composites contain oriented or randomly oriented fibers, glass beads, flakes of metal or mica, or sawdust just to name a few. Most composites are designed to increase mechanical properties, some are designed for dimensional stability, increase aesthetics, and to lower cost of the end product.

Fiber reinforced composites are designed to take advantage of the high strength to weight ratio of the fiber, and are known to include a variety of fiber configurations. These configurations deal primarily with the characteristics of the fiber, that is, whether it is a monofilament or multi-filament bundle or yarn, whether it contains continuous or discontinuous strands. Also, whether the fibers are preformed into a prepreg, a mat, or a roving, and finally, how these fibers are aligned.

Fiber alignment is defined based on the direction in which the long axis of the fiber is oriented relative to other fibers. For example, uniaxially oriented composites mean that the long axis of all the fibers are aligned in a single direction, such as 0° or 90°

relative to the applied load; where as biaxial orientation has fibers aligned in two different directions; these two directions are not necessarily orthogonal to one another. However, for mat composites a rather unconventional orientation is given for the mat. In the case of a CSM there is no preferred orientation, hence the mat is essentially random. However, due to the bias, of the glass mat, the take up direction is considered the 0° direction and perpendicular to that direction would be the 90° directions. When tests were performed on CSM they were done in accordance with the conveyance or take-up direction, that is either 0° or 90°. The composite in the present study is that of a continuous swirl mat composite in which the swirled strands are multi-filament bundles randomly oriented.

Fibrous fabrics and mats being constructed within a polymer matrix is not a new concept. However, since the inception of mat reinforced composites there has been a lack of scientific data from which a designer could make reasonable engineering decisions for its use. This resulted in a class of materials that were never optimized for design. Only in recent years has fabric composites re-emerged as a competitor for metals. The fabric/mat composite research community is developing ways in which this class of composites can be evaluated. The following sections will address the general as well as some specific issues of fiber composites. The hope in presenting this material is to provide enough background for a greater understanding of the importance and placement of this research.

4.2 Fiber Reinforced Composites

In the continuing effort to achieve lighter weight materials while maintaining high strength many companies are utilizing composite materials. There are five basic factors to consider when using such a composite: 1) fiber type and 2) fiber orientation; 3) resin; 4) manufacturing process; and 5) performance and cost. The first two factors influence the physical properties of the composite, whereas the materials selection, design, and composite fabrication process influence the last two factors.[3] One of the foremost composite types is that of inorganic fiber reinforcements in an organic matrix, commonly glass fibers in a polymer matrix. However, there are a series of other fiber systems available, which use carbon, aramid, and metallic fibers as a reinforcement.

Carbon, aramid, and metallic fiber-reinforced compounds have unique applications. Carbon fiber reinforced systems, such as Carbon/Epoxy, have the ability to provide electrical conductivity, increase thermal conductivity, and good mechanical property retention. Aramid systems, such as Kevlar/Epoxy, have great wear resistance and a low mating-surface wear. The metallic fiber systems are used in some cases for their electrical properties.[4] Yet, they can be found in a variety of applications. The properties of these different fiber types are shown in Table 1.

4.2.1 Glass Fiber

There are several different types of glass fibers that can be used in composite applications as previously mentioned. The most commonly used is E-glass. However, the fiber chosen should depend on the application. Other types of glass fiber and their compositions are shown in Table 2. Table 2 and Table 3 show the chemical and

Table 1. Fibers and their mechanical properties.

Fiber	Tensile Strength (GPa)	Young's Modulus (GPa)	Elongation (%)
Carbon (PAN)[5]			
• Low modulus	3.3	230	1.4
• High modulus	2.4	390	0.6
Kevlar[6]			
• Kevlar 29	3.6	83	4.0
• Kevlar 49	3.6-4.1	131	2.8
• Kevlar 149	3.4	186	2.0
Metallic[7]			
• Boron Tungsten	5.5-7.0	400	1.3-1.7
• Boron Carbon	5.0	400	1.2
• α-alumina	14	390	3.6

Table 2. Glass fiber compositions[8,9,10]

Components	E-glass (%)	S-glass (%)	C-glass (%)
Silicon dioxide	52-56	65	64-68
Aluminum	12-16	25	3-5
Boric Oxide	5-10	•	4-6
Sodium Oxide and Potassium Oxide	0-2	•	7-10
Magnesium	0-5	10	2-4
Calcium Oxide	16-25	•	11-15
Barium Oxide	•	•	0-1
Titanium dioxide	0-1.5	•	•
Iron Oxide	0-0.8	•	0-0.8
Iron	0-1	•	•

Table 3. Mechanical properties glass fiber.

Material	Tensile Strength (MPa)	Young's Modulus (GPa)	Elongation (%)
S-glass	4585	85	~2
C-glass	3310	65	~2
E-glass	1725	69	~2

mechanical differences between E-glass, S-glass and C-glass. E-glass is a calcium aluminoborosilicate based compound with a maximum alkali content of 2%. E-glass is a general-purpose fiber with good strength and high electrical resistance. S-glass compositional make up is magnesium aluminosilicate with very high tensile strength. C-glass is a soda-lime-borosilicate with good chemical resistance in acidic environments[11]. It is readily seen here that the glass composition determines the response of the fiber in a given chemical and mechanical environment. Again, however, E-glass is used most often due to its good balance between electrical and mechanical properties and cost less than S-glass or C-glass.

4.2.2 Glass Fiber Fabrication

"Glass is made by fusing silicates with soda or with potash, lime, or various metallic oxides." There are two basic methods of fabrication common to the production of glass fibers. The older of the processes is "Marble Melt" while direct melt is a more recent process.

The marble melt process starts by producing glass spheres, approximately 2.54 cm in diameter, from the appropriate mixture of constituent components. These glass marbles are melted again, extruded through a spinneret, and drawn at varying take-up speeds to obtain consistent fiber diameters. The "Direct Method" is a one step process that combines constituents in the molten state, which is then extruded through spinnerets and drawn.

Fibers produced from these two processes have diameters ranging from 3-20 μm. However, once fibers are formed they have a very abrasive response to one another and are therefore coated with permanent and non-permanent coatings. The coating protects fibers as well as promotes fiber-fiber and/or fiber-matrix interactions.[12]

4.2.3 Polymer Matrix

The matrix materials used in composites are both thermoplastics and thermosets. The commonly used matrix materials are Epoxy, Polyimide, Polyurethane, Polyester, and Polyvinyl. The matrix serves two distinct purposes: (1) maintaining the fiber reinforcement configuration in the unloaded state and (2) to transfer the applied stresses to the reinforcement during loading. For example, composites used in structural applications, the matrix material displays a greater elongation at break than the reinforcement, which optimizes the tensile load on the fibers. The choice of matrix material is also governed by the nature of the chemical, electrical and/or thermal environments.[7] The unique characteristic of the matrix materials is the presence of amines and carbonyl functional groups or delocalized electron configurations, that interact with the coupling agent on the surface of the reinforcing fiber.

4.2.4 Composite Interface

The science of fiber forming makes fibrous reinforcement a possibility. However, it is the interface between the reinforcement and the polymer matrix that makes the engineering application of composites a reality. The importance of the interface is a realm of science that industries do not particularly like to share due to the fact that a perfect interface results in a perfectly functioning composite. Developing the relationship between the reinforcing component and the matrix is a challenge for every new system of components.

The most contemporary term that describes the basic interfacial component is the word "Sizing". A sizing by definition is a protective coating for the fiber. The term "finishing agent" is used in textiles to mean a sizing.[13] Other terms that are used to mean a sizing is coupling agent and binding agent. It should be noted that a surface treatment is not a sizing.[14,15] However, a well designed sizing does produce a good coating, an interphase region that both the reinforcement and the matrix interact through. Listed in Table 4 are the major uses of a sizing.

In developing fiber sizings the characteristics of importance are compatibility, protection of the fiber and moisture resistance, in the case of glass. There are, however, sizings that do not meet these qualifications and polymer coatings are used as a replacement. The compatibility and protection are not the biggest problem with polymer coatings. The problem with polymer coatings that form good interphase layers is they have functional groups that contribute to the hydrophilic nature of the polymer. The hydrophillicity is a detriment to the interaction of both components and therefore great care must be taken when combining the two.

The theory behind the interaction of the interphase region with both the reinforcement and the matrix has been studied extensively in relation to silanes.[16,17,18] The concept of the sizing producing a simple chemical interaction between the reinforcement and the

Table 4. Sizings and their utility.[19]

Type	Purpose	Example	Remarks
Film forming organics and polymers	To protect reinforcement during processing	Polyvinyl alcohol (PVA), Polyvinyl acetate (PVAc)	The polymer designed to wet-spread, that is, to create an even coat along fiber. It can later be washed off
Adhesion promoters	To improve composite mechanical properties and/or moisture resistance	Silane coupling agents	Principally used on inorganic reinforcement, for example, glass fiber.
Interlayer	To enhance composite properties by creating an interphase between matrix and reinforcement	Elastomeric coating	Not in commercial use.
Chemical Modifiers	React to form protective coating	Silicon carbide on boron fibers	

matrix has been discredited by research into the mechanism of how they function. It was found that the silanes form a polymeric network on the surface of the reinforcement with occasional chemical interaction. The major finding was the network interphase region enabled the matrix material to become entangled with the reinforcement, which was to some degree chemically bonded to the sizing. See Figure 1 and Figure 2 for a conceptual schematic of the discredited and the well-accepted relationship of the sizing with the reinforcement and matrix.

4.2.5 Mechanical Response of Composites

The mechanical properties of a composite are dependent on the mechanical properties of the fiber reinforcement and polymer matrix, the orientation of the fiber reinforcement, and the volume fraction of each component. It is known that as the volume fraction of glass fiber in a composite increases there is a corresponding response in practically every mechanical property.[20] For example, if all the fibers are placed parallel to each other, that is, they are uniaxially oriented, the tensile strength and modulus are maximized in that direction, and the composite is anisotropic. If half the fibers are arranged perpendicular to the other half, that is a cross-ply, they are biaxially oriented, then the tensile strength is at a maximum in those two directions. However, the tensile strength in either direction of a cross-ply composite is less than the uniaxial case, due to the load bearing capacity of the fibers perpendicular to the loading direction. This fiber arrangement also leads to an anisotropic composite. If the fibers are arranged in

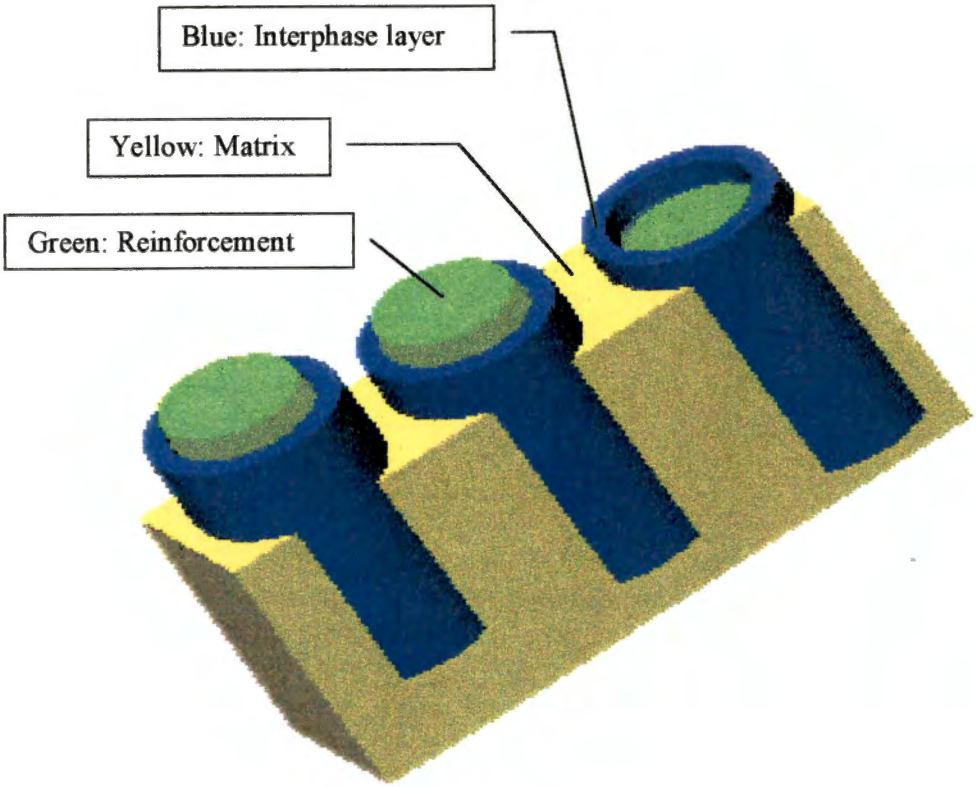

Figure 1. Accepted view of sizing interaction with fiber and matrix.

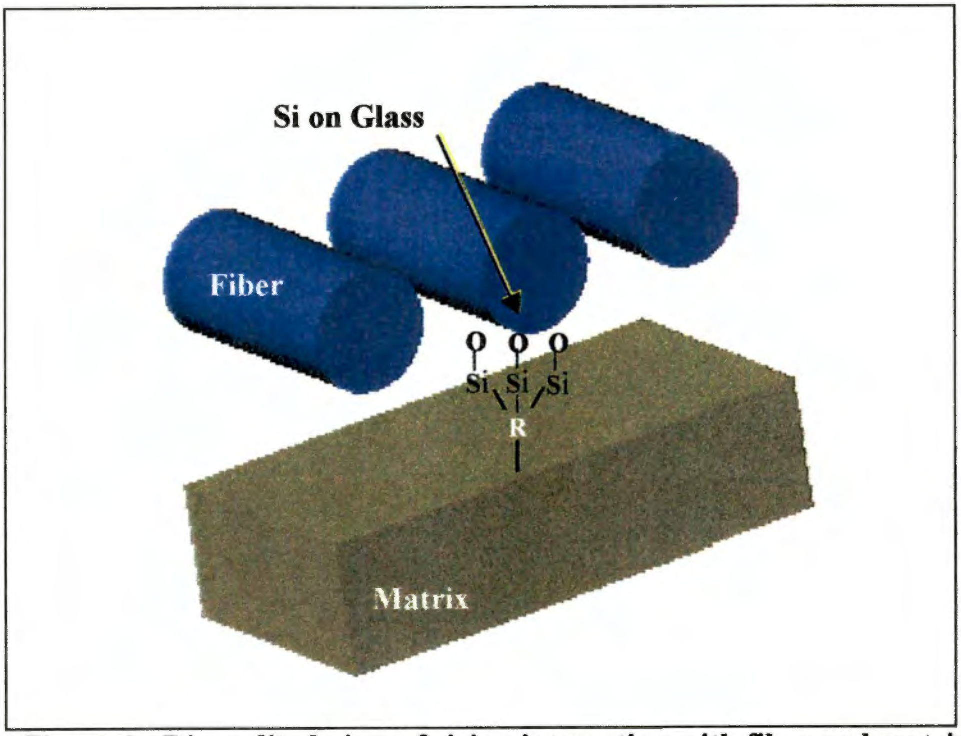

Figure 2. Discredited view of sizing interaction with fiber and matrix.

three-dimensions or randomly, then the tensile strength and modulus of the composite is nearly isotropic or possibly transversely isotropic. The effect of randomly oriented fibers in three dimensions is a reduction in the overall mechanical properties in comparison to the same system with uniaxially oriented fibers. This degradation in properties was shown from research by M.M. Schwartz [21] to be approximately a third for the comparison of three dimensional randomly oriented fibers to uniaxially oriented fibers.

An equation which takes into account the importance of fiber orientation relative to the applied load is shown in Equation 1 where $\sigma_{B\theta}$ is the overall breaking stress of the composite with a given fiber orientation relative to the applied load. Three other parameters necessary to carry out the calculation are the longitudinal, σ_{BL}, and transverse tensile strengths, σ_{BT}, and the shear strength, σ_{BS}.[22]

$$\boxed{\frac{1}{\sigma_{B\theta}^2} = \frac{\cos^4\theta}{\sigma_{BL}^2} + \left(\frac{1}{\sigma_{BS}^2} - \frac{1}{\sigma_{BL}^2}\right)\cos^2\theta\sin^2\theta + \frac{\sin^4\theta}{\sigma_{BT}^2}}$$

Equation 1

The angular dependence is shown by theta, θ, in the above expression. An example of different fiber orientations is illustrated in Figure 3. For the case of single plies, theta in Tsai's expression would refer to the fiber angle relative to the loading direction. That is theta would have a value of θ=0° when the fibers are parallel to the loading direction, and when the fibers were perpendicular to the loading direction θ=90°.

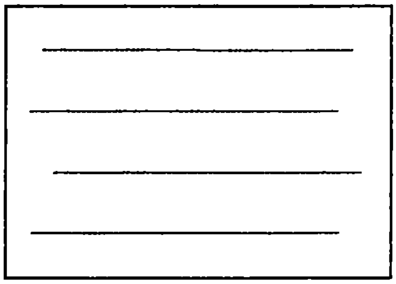

One-Dimensional (Parallel) Orientation

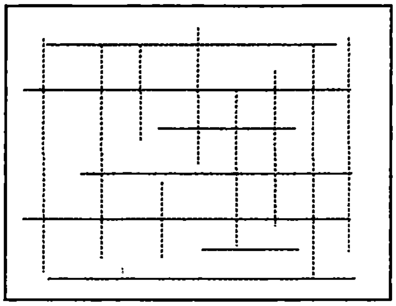

Two-Dimensional (Perpendicular) Orientation

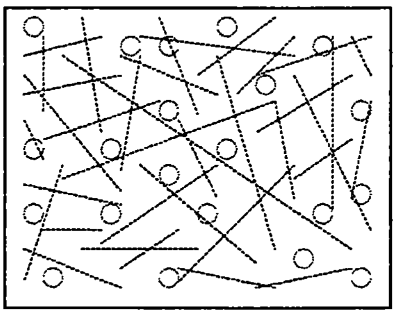

Three-Dimensional (Random) Orientation

Figure 3. Three fiber orientations used in composite reinforcement[7]

The capacity of a composite to redistribute stresses is dependent on complimentary interactions between the reinforcement and matrix. However, the composite can only perform this important function, if the reinforcement and matrix interact effectively at the interface. For some composites, this interaction may be achieved simply through contact of the matrix and the fibers, while other composites require a chemical coupling agents to create the most effective adhesion between the two constituents. The coupling agent is usually in the form of a couplant sizing on the fiber surface. This surface treatment, or sizing, is designed to strengthen the interfacial bonding between matrix and reinforcement.[7] With the proper adhesion between fiber and matrix, the interfacial bonding is considered strong and shear-resistant. When a tensile load is applied to the composite, stresses are redistributed to the reinforcement via the interface. The shear strength of the fiber/matrix interfacial bonding limits the strength of the composite, regardless of the individual tensile strengths of the fiber or the matrix. The presence of voids or the lack of good interfacial adhesion will severely decrease the efficiency of the reinforcement by impeding proper distribution of the stresses within the composite. Insufficient interfacial bonding will cause instabilities around the fibers, enabling the formation of microcracks that initiates failure.

4.3 Composite Fabrication Techniques

There are a variety of different composite molding techniques such as compression molding, resin transfer molding, RTM just to name a couple.

Compression molding is the most technologically developed processing techniques, which is often referred to as sheet molding compound, SMC. SMC refers to the material compound used, which is a polymeric sheet with either a continuous or randomly oriented reinforcement. This technique can produce parts of various sizes and applications. The primary application for this technique is found in the automotive industry for the manufacturing of grille opening panels, exterior panels and hoods. Another technique is Resin Transfer Molding, RTM. This technique is different to the SMC technique in that the reinforcement is placed in the mold, the mold is closed and then the resin injected. In the case of thermosets, the resin is allowed to cure before removal from the mold. This technique is similar to that of reaction injection molding, RIM, however, the distinction is made with RIM due to the use of two components that react in the mold cavity.

The use of Reaction Injection Molding, RIM, evolved due to the desire to produce complex plastic parts rapidly from low viscosity monomers or oligomers. The RIM process, as shown in Figure 4 permits the mixing these materials through a process called "Impingement Mixing" prior to entering the mold. Mixing occurs in the mixhead where two or more reactants flowing at high pressure approximately 100 to 200 bars (1500 to 3000 psi), into the mixhead. The flow rate of the reactants is controlled to ensure the correct stoichiometry for reactants. At the point of mixing the polymerization process begins and the mold is filled.

Structural Reaction Injection Molding, SRIM, is similar to RIM process with one major difference. The structural component is placed in the mold prior to filling. These structural components are generally reinforcements of various types. In this research the reinforcement is a five (5) layer mat of continuously swirled E-glass fibers.

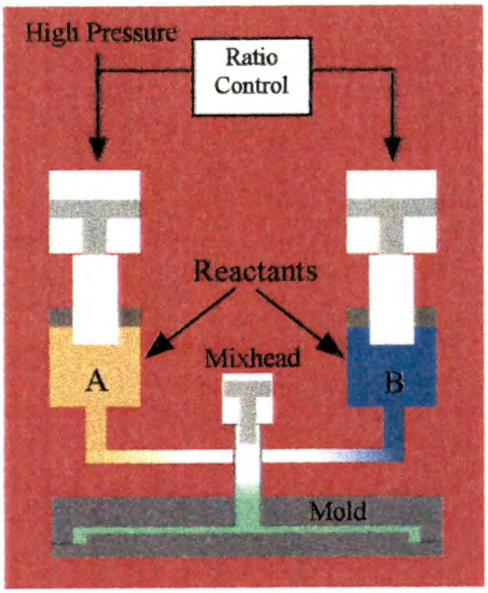

Figure 4. Schematic of the RIM process.

Some advantages of the RIM process are: 1) The energy savings due to low temperature, during processing; 2) Low equipment cost; 3) Produces complex geometric shapes quickly.[23] The disadvantages of the RIM process are: 1) The off gassing of the reactants can cause the product to have voids; 2) The flow of matrix in the mold is often controlled by the fiber orientation. This results at times in density differences.

4.4 Composites and Damage

4.4.1 Damage Associated with Composites

The application of composites are found in numerous areas in engineering design, which introduces composites to different types of loading conditions, such as tensile, creep and fatigue. This type of mechanical loading produces localized and accumulated damage, while environmental exposure can produce damage induced by chemical interaction with fiber, matrix and interface.[24, 25, 26]

The mechanical damage, associated with composite failures, can be categorized as four mechanisms, which can occur simultaneously. These four mechanisms occur in both brittle and ductile composites. These are generally described as matrix cracking, fiber breakage, fiber/matrix interfacial debonding, and fiber pullout. Prolonged exposure to harsh environments can produce its own characteristic damage and/or accelerate or pacify the known damage mechanisms.

The damage associated with the matrix is cracking. The known failure of a polymeric matrix material is chain breakage due to its inability to withstand a given load. Damage in the matrix appear as cracks which range from microcracks, observable only under magnification, to macrocracks, which can be observed with the naked eye.[27] The damage features observed for brittle and fatigue failure are shown in Figure 5 and Figure 6. These schematic representations of polymer fracture surfaces, show brittle fracture bands and fatigue crack propagation, respectively.

Figure 7 is an SEM image of a glass fiber reinforced polyester composite, displaying a river pattern as the fan-shaped matrix distortion on the right edge. Figure 8 is an SEM image of a cotton fiber filled phenol-formaldehyde sample, showing matrix distortion as step-like formations which are brittle fracture bands. The brittle fracture bands and river patterns can be used to find the origin of the failure. The fracture spreads out from the point of origin much like the spreading open of a fan, where the point of convergence of the fan's arm is the point of initiation.

Fiber breakage, evident over an entire fracture surface and possibly internally, is discernible by the distinct snapping of fiber bundles and monofilaments. Fiber/matrix interfacial debonding occurs within the material and on the fracture surface, distinguishable by areas where fiber bundles were apparently lying at a time prior to failure. Fiber/matrix debonding occurs when the fiber and matrix are no longer physically in contact with each other. This phenomenon occurs at varying degrees with fiber breakage, matrix cracking and fiber pullout. Fiber pullout results when, under load, the fiber debonds from the matrix material due to failure of the interface. An obvious consequence of fiber debonding, breakage and pullout is that the composite loses its ability to effectively transfer stresses from the matrix to the reinforcement. Therefore, the mechanical properties of the composite, such as strength and stiffness, are greatly

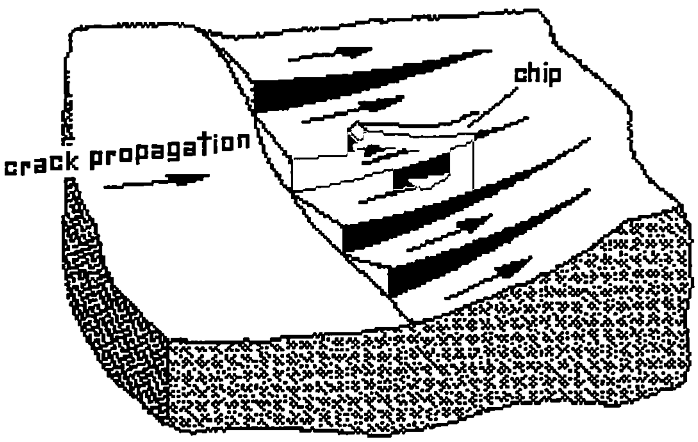

Figure 5. Schematic of brittle fracture bands[28]

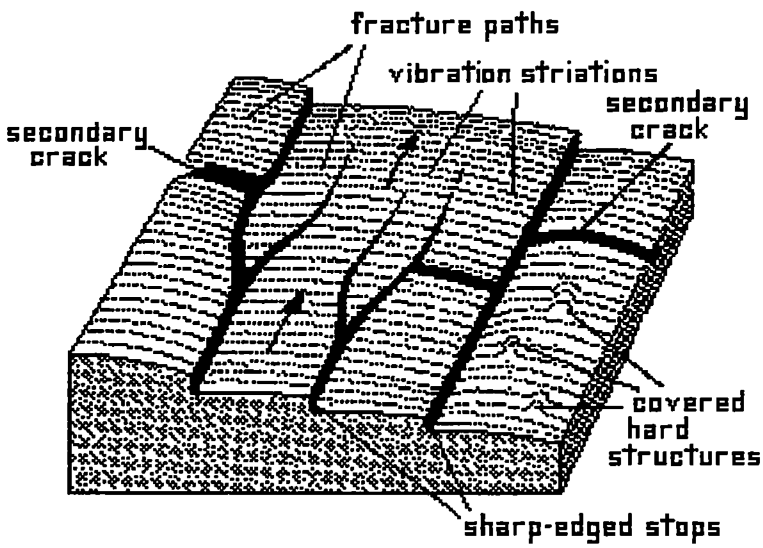

Figure 6. Schematic of fatigue crack propagation[16]

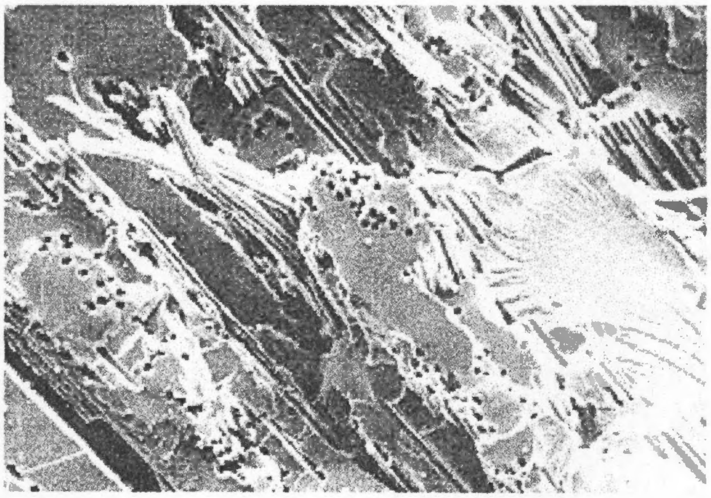

Figure 7. Glass fiber reinforced polyester showing river pattern[16]

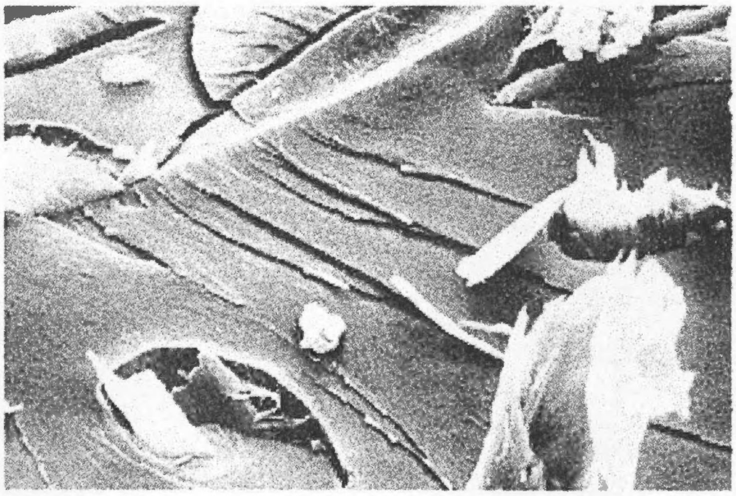

Figure 8. Cotton fiber phenol-Formaldehyde, brittle fracture bands[16]

reduced, and the material cannot perform the functions for which it was designed. Figure 9 is an SEM image of a glass fiber reinforced polyester composite that displays breakage and pullout of the glass fiber bundles. Figure 10 is a SEM image showing the fracture surface of glass fiber reinforced polycarbonate where evidence of fiber/matrix debonding and fiber pullout can be seen. The arrow in Figure 10 indicates the place where a fiber was lying prior to failure but debonded and pulled away from the surface during fracture. The damage usually associated with exposure to harsh environments can be characterized as degradation of the matrix material, environmental attack on the fiber reinforcement, and a degradation of the fiber/matrix interface. Disruption of the transfer of stresses from the matrix to the fiber reinforcement, similar to that resulting from mechanical damage, can occur as a result of environmental exposure. Hence, environmental damage can also seriously impair the mechanical performance of the composite material. Figure 11 is a SEM micrograph of glass fiber reinforced polycarbonate that was exposed to carbon tetrachloride while under stress. The matrix shows some degradation in the form of feathery structures on the matrix fracture surfaces. The fibers appear to be clean on the surface, indicating that they easily debond from the matrix and pulled out during failure.

4.4.2 Continuous Swirl Mat Composites

There is a considerable amount of material available in the literature concerning the characterization of composite materials. The bulk of the information revolves around composite laminates. Composite laminates consist of a lay-up of directed fibers, which have poor transverse properties. The failure of such configurations dominates the

Figure 9. Glass fiber reinforced polyester, fiber breakage and pull-out [16]

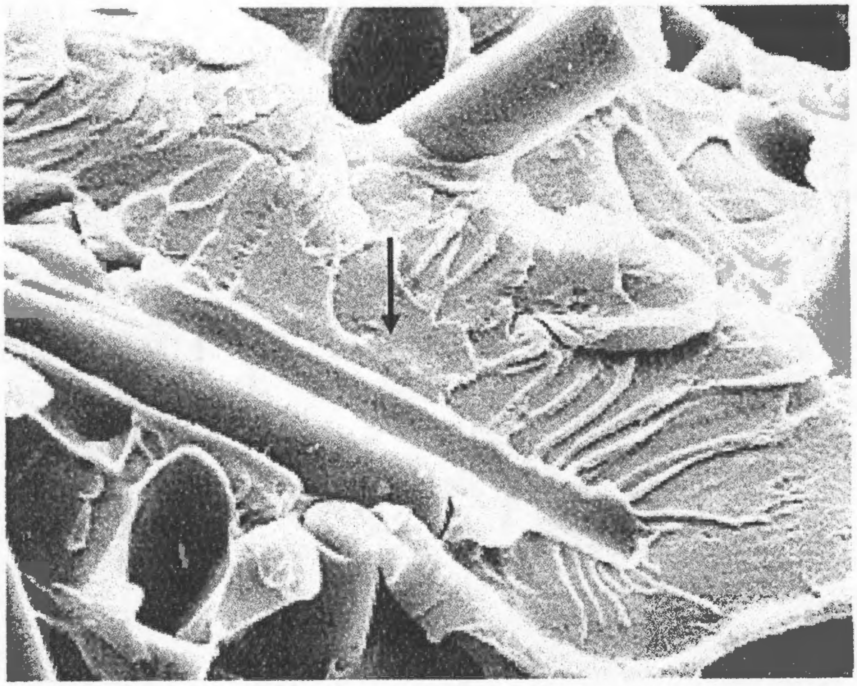

Figure 10. Glass fiber in polycarbonate, debonding and fiber pull-out.[16]

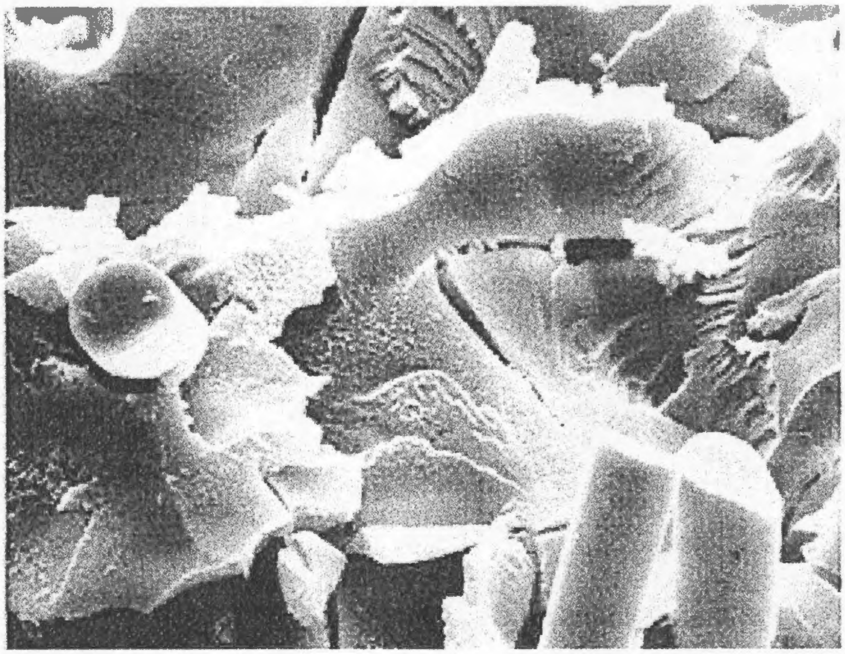

Figure 11. Glass fiber in polycarbonate, matrix degradation and debonding.[16]

research literature available for composites. There are, however, other composite types available such as sheet molding compound, (SMC), and continuous swirl mats, (CSM). SMC composites, which consist primarily of oriented short fibers, pressed between two polymeric outer layers.

Continuous swirl glass mat composites, CSMC, consist of a polymer matrix reinforced with a continuous monofilament or multi-filament strands. These strands are mechanically laid as a single layer mat and coated, in some cases, with a thermoplastic coupler or other coupling agent. The nearly isotropic loading characteristic of the CSMC makes it suitable for various applications where three-dimensional load considerations are needed. The ability to mold the CSMC's into complex parts makes it a desirable reinforcement where conformability is required.[7] Currently, CSMC are used to manufacture safety helmets, luggage, electrical parts, machine housings, and automotive parts.

A few independent studies have been performed to determine the mechanical behavior of composites, using a CSMC reinforcement with the Reaction Injection Molded, RIM, and thermoplastic matrices. Matrices studied were polypropylenes and polyamides.[29,30,31,32] In these studies, the focus was on static and dynamic loadings of notched samples for analysis using fracture mechanics. However, some nondestructive test methods, such as acoustic emission and infrared thermograph, have been used to observe failure events and damage zone development in these CSMC's.[8,33,34]

Stokes[35, 36, 37] and Karger-Kocsis[38,39], performed some work on CSMC. The research by Stokes revolved around the mechanical characterization of that particular system.[40] Stokes work was directed at understanding and characterizing changes in modulus and tensile strength. The modulus measurements were made on 0.5 in. wide specimens. The modulus was measured every 0.5 in. along the gauge length of the specimen to determine how much variation in modulus could be expected for these type of materials. It was determined that the modulus could vary by a factor of 2 for adjacent 0.5 in. areas, and by a factor of 3 over an entire plaque. Stokes stated that the materials were essentially homogeneous, but on a large scale.

J. Karger-Kocsis[41, 42] performed additional studies on a mat composite. The objective of this work was to provide designers with design parameters for polyamides and polypropylenes reinforced by a CSM. His investigation looked at static and dynamic test of notched specimens. His studies enabled the surface to be examined after failure. The studies included the correlation of acoustic emission events with individual failure events. Other studies were performed by Owen et. al. [43, 44], their work reflected an in-depth study of the tensile, fatigue, and fracture toughness response of chopped short fiber laminates. The system in study was a polyester resin with an E-glass reinforcement. This work showed that fatigue loading was more damaging than continuous steady loading. It was also shown that an increase in glass fiber volume fraction increased the UTS, but had only a small effect on fatigue strength at 10^4 cycles. And finally, the loss in modulus at the onset of cracking was around 10%.[45]

Recently, new composites, employing the CSMC reinforcement, have been developed that incorporate cross-linked polyurethanes and polyureas for specific structural parts, providing desired strength and weight reductions. For the last three years, the Durability of Lightweight Composite Structures for Automotive Applications Project, undertaken at ORNL, has set about to characterize a CSMC composite material. This project has involved the study of mechanical behavior under tensile, fatigue, creep, and low-energy impact of a swirl E-glass mat reinforcement with a cross-linked polyurethane composite.[46, 47]

4.5 Damage Assessment Techniques

As the application of composites increase, a better method to identify the presence of damage in these materials become more desirable. Nondestructive test methods commonly used to qualify and determine damage in metallic materials are not necessarily useful when dealing with nonmetallics. Therefore, while some methods can be modified, new methods must be developed. The optically aided visual inspection of composites remains the best technique for detecting surface damage. Internal damage, however, must be found using some cross-sectional image interpretation such as Magnetic Resonance Imaging, MRI, or a cross-sectional averaging of a given signal such as Ultrasound. The transmission of energy in the form of sound waves to detect internal flaws is the technique known as ultrasonic inspection. For non-opaque materials, the transmitted signal can be as simple as light enabling some internal features to be resolvable.

4.5.1 Ultrasonic C-Scan

To describe ultrasonics physically, a sample is bombarded by compression waves via a liquid medium. This energy form is ultrasound, inaudible to the human ear due to the high frequency of the waves. In order to determine the wavelength of the ultrasound, the velocity of the propagating wave must be divided by its frequency. This is important for the detection of internal flaws in a material because the detection limit for a flaw is on the order of one wavelength. If the wavelength is larger than an internal flaw, that flaw will not scatter the ultrasonic pulse and therefore, eludes detection. Additionally, ultrasound propagating velocity differs from one material to another. The wavelength of the ultrasonic pulse is longer in those materials, which allow faster propagation of the ultrasound.[48]

C-scan ultrasonics is a nondestructive test method that is evolving as a tool for composite evaluation with the development of increasingly more powerful computers. Specifically, the C-scan method involves the mapping of ultrasonic echoes that are reflected back from a flat or nearly flat sample. Figure 12 represents a schematic of a typical C-scan ultrasonic apparatus.[17]

In Figure 12, the probe emits the ultrasonic pulse, which propagate through a coupling medium, usually water, in a scanning tank to the specimen. Echo #1 is known as the front-side echo. This is the ultrasound wave reflected from the front surface of the specimen back to the probe in twice the travel time as the initial wave. The reflected wave amplitude is less due to attenuation of the wave in the coupling medium, from wave spreading, and some transmittance of the incident sound into the sample. Echo #2 is the backside echo or that which the back surface reflects toward the probe. This echo arrives later and with less amplitude than Echo #1 because only some of the wave travels back through the sample and the water before reaching the probe. Some of the back surface

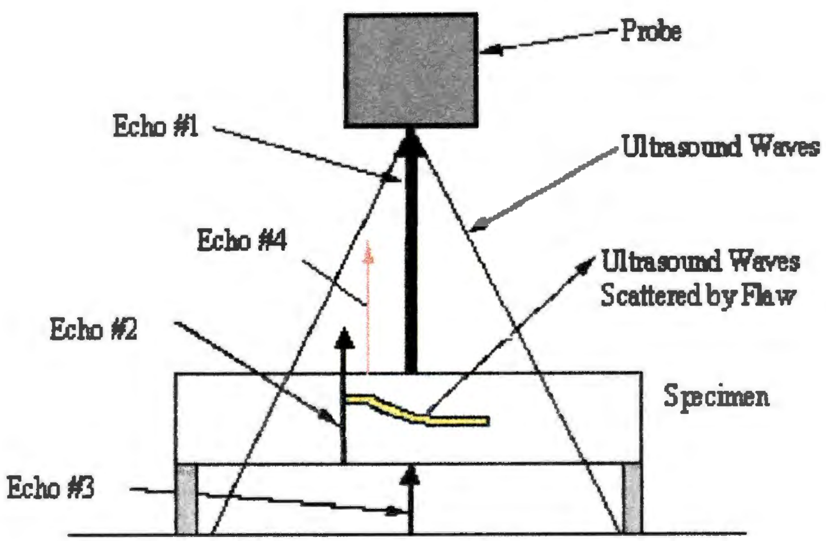

Figure 12. Schematic of Ultrasonic C-scan 17

reflected waves bounces back from the front surface to remain inside the sample, and some of the wave is transmitted completely through the sample. Tank-bottom echo is that which is reflected back from the bottom of the tank after traveling through the couplant and sample twice and is represented by Echo #3. This echo will arrive much later than the first two echoes and with only a fraction of the original ultrasound wave. Most of the echo will remain in the specimen, having encountered the front and back surfaces again on the return path back to the probe.[17]

Should the ultrasound wave encounter any flaws within the sample, the probe may pick up reflections of the wave as Echo #4. This echo will only represent that part of the wave that is reflected from flaws approximately perpendicular to the incident wave. Any flaws or sections of flaws, which are not more or less perpendicular to the incident wave, will only serve to scatter the wave in directions that will remain undetected. All of the echoes detected by the probe make up the pulse echo profile, and there exists such a profile for each sampling point, encountered during scanning of the

specimen. The typical profiles, as shown in Figure 13, Figure 14 and Figure 15, for the pulse echo signal are known as an A-scan. The A-scan is an oscilloscope display of the echoes. The x-axis represents time of flight of the pulse, which is converted into distance traveled by the pulse. The y-axis represents the amplitude of the echoes. The A-scan image shown in Figure 13 has two large signals one at 59.5μs and 62.5μs. These two signals refer to front surface and back surface reflections. If there were flaws within the thickness, there would be peaks to represent those reflections. For example, Figure 14 has a peak near the back surface signal, which represents a flaw near the back surface,

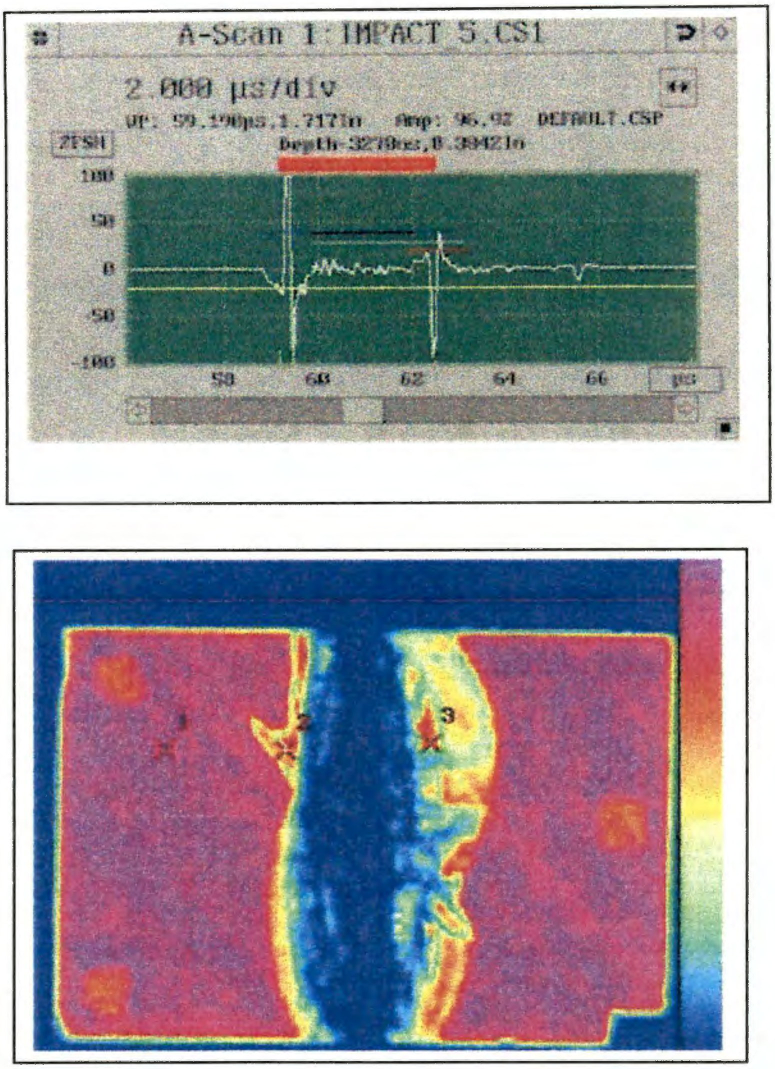

Figure 13. A-scan and C-scan of area 1.

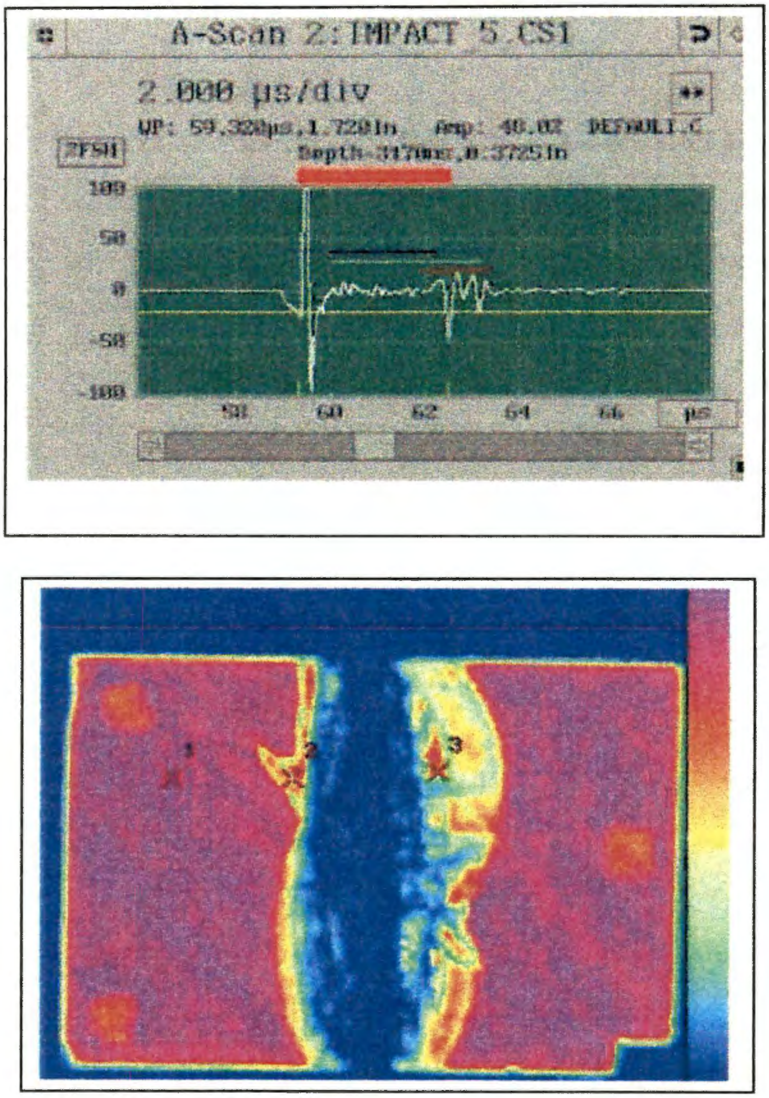

Figure 14. A-scan and C-scan of area 2.

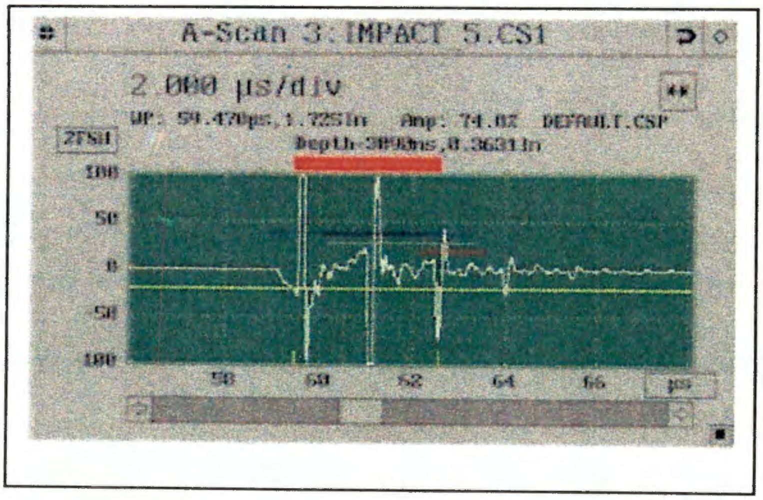

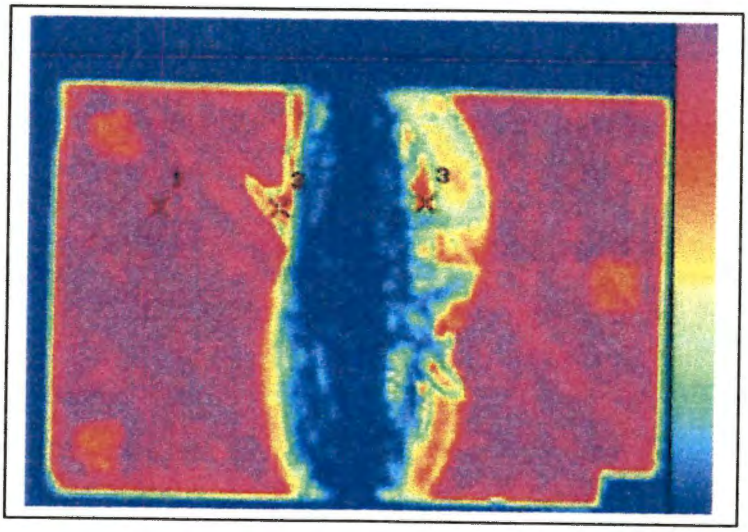

Figure 15. A-scan and C-scan of area 3.

while Figure 15 has a large peak between the front and back surface signals. This peak represents a flaw at the center of the specimen.

In more advanced ultrasonic systems, there exists the ability to set an arbitrary number of gates after the experiment. This, in turn, allows the generation of arbitrary echo time slices from which the corresponding maximum amplitudes can be obtained. The three dimensionally assembled amplitude maps are termed C-scans. These amplitude maps specify the location and other information about discontinuities, which represent echo-generating interfaces, through the sample.[17] Shown in Figure 13, Figure 14 and Figure 15 are C-scans. The areas labeled as 1, 2 and 3 in the C-scan corresponds to the A-scan shown above it. Notice in each of the A-scans generated for the labeled areas that the flaw produces a signal between the front and back surface reflections.

Detection and measurement of flaws depends on their attenuation of the transmitted sound waves. The images gathered, using the C-scan ultrasonic method, are a map of the specimen that displays, usually in grayscale, its internal features. Flaws in the specimen, when using grayscale colors, generally appear as dark areas due to scattering of the transmitted sound waves. By comparing the pre- and post-test C-scan images of a sample, sustained damage will appear as darkening of certain areas in the post-test image.[17]

4.5.2 Light-Transmission Microscopy

Light-Transmission Microscopy (LTM) is another test method, used on composites, of which the nondestructive benefits are currently being realized. This technique is very simple in operation, yet it can reveal many internal details about a material that can have a direct influence on service life. In LTM, a high intensity light source is placed on one side of a relatively translucent composite sample, such that the light is transmitted directly through the specimen. The microscope is adapted to a video camera or a video microscope. From this set-up it is possible to detect internal features, such as void spaces, fiber orientation, and any defects due to processing or form as a result of mechanical testing or service.[49] Highly advanced computer systems and specialized acquisition software have been developed that enable the examination of polymer composite samples before and after mechanical testing. A comparison of pre- and post-test images provides for the determination of damage sustained on a subsurface level. This same configuration is also utilized in real-time evaluations, which will be discussed in later. Depending on the reason for using this technique, possible limitations of LTM arise mostly in relating image resolution to depth-of-focus. Generally, some image resolution is sacrificed in order to focus deeper into the specimen's interior. This problem can sometimes be alleviated by the utilization of lenses with greater magnifying capability.

4.6 Scanning Electron Microscopy

The use of Scanning Electron Microscopy, SEM, to examine polymer-based composite materials has certain advantages. At low operating voltages, approximately 1 to 1.5 KeV, polymers and polymer-matrix composites may be viewed without the addition of conductive coatings, which can decrease the amount of detectable surface detail. This is significant when searching for defects or damage on a test specimen or fractured sample. On the other hand, the lack of a conductive coating on the polymer specimen can lead to the disadvantage of increased charging on the specimen surface. This charging results when there is a build-up on the specimen surface of an excess charge that cannot bleed off in the case of a non-conductive sample. If SEM operating conditions are adjusted such that the secondary and back scattered electron emissions balance the incident beam current, then the occurrence of charging is kept to a minimum. There is an incident beam energy at which this condition holds true, known as E_2, which is a function of the electron beam energy, E_0, and the atomic number, Z, of the specimen examined. Since polymers are generally of lower atomic numbers than metallic materials, the E_2 is also lower. Further, charging may then be categorized two ways:

1. If $E_2 < E_0$, then the specimen is experiencing negative charging, characterized by an extremely bright image; there are too many secondary electrons being detected as they are repelled by the specimen surface.

2. If $E_2 > E_0$, then the specimen is experiencing positive charging, characterized by a very dark image; there are too few secondary electrons being detected as they migrate back to the specimen surface and eventually balance the charge on the surface.[50]

Another effective means of eliminating specimen charging is to operate the SEM in the backscattered electron mode rather than secondary electron mode. In the backscattered electron mode, the incident beam penetrates the specimen surface more deeply than in the secondary electron mode, and approximately half the incident beam energy is reflected back as backscattered electrons into the same hemisphere as the original beam. A detector specifically designed to impede and collect backscattered electrons is used, and the specimen chamber is purged with a gas, usually nitrogen, during scanning. The incident electrons may ionize the gas molecules after which the positive ions are attracted to the negatively charged specimen surface, neutralizing charging effects. Additionally, as the gas pressure is increased, the incident beam current/voltage can be increased to values that would normally be too great for use on non-conductive materials, usually around 20 KeV. This advantage enables the operator to achieve greater resolution while imaging the specimen surface.[51]

4.7 Image Analysis

The use of imaging techniques with microscopy and/or video microscopy provides an approach to collecting optical data at varying magnifications as the events occur. The observation of surface and subsurface defects can be identified and recorded. The recorded images can then be inspected or video reviewed several times. The common characteristics of failure can be applied to the development of a failure mechanism for this CSMC. Still images were obtained and used to provide a more in depth analysis of a single event or a series of events.

There are several digitizing techniques available to produce images of specimens under investigation. The images provide at times a dearth of information. Besides still images, systems enabling video collection of different processes in real time have been established as a way to observe more details not obtainable by still photos.

Figure 16 is a schematic representation of the video collection system design in our laboratory, which utilized video microscopy with variable magnification. Image analysis is a general term used to describe the interpretation of still or video images. The interpretation, however, can range from making physical measurements to describing a failure process.

Image analysis of digitized C-Scans amplitude maps was developed in our laboratory. This technique provides application to the integration of color or grayscale for damaged specimens. This provides a relatively easy and cost effective way to evaluate the overall damage state of a given specimen in a reasonable amount of time.

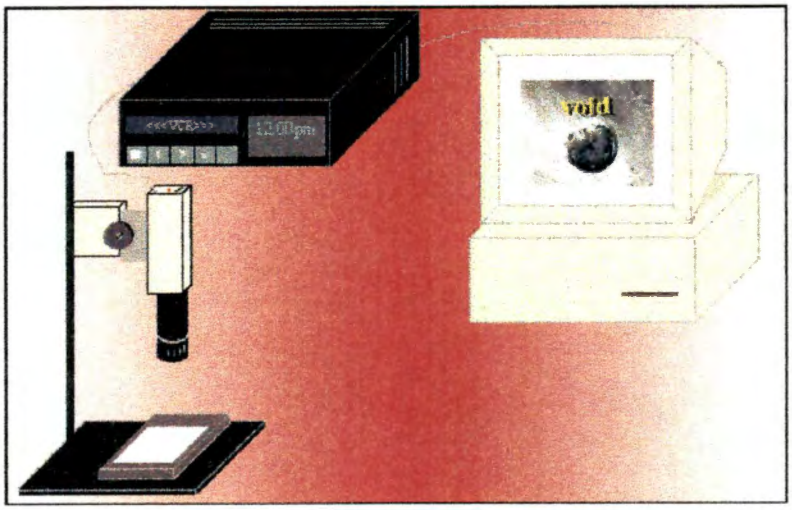

Figure 16. Real-time video collection setup.

V. THEORETICAL AND EMPIRICAL APPROACHES

5.1 Mathematics of Material Failure

5.1.1 Rule of Mixture

A specimen composed of more than one component has a mechanical response due to the contribution of each component's individual characteristic. The "Rule of Mixtures" is a empirical approach that describes the individual contribution of each component based on weight or volume fraction. As shown in Equation 2, the property being evaluated is 'P' and the weight or volume fraction of that component is 'φ' while 1 and 2 represent each component. In the case of composites, it is generally accepted that the fiber reinforcement is 1 and the matrix is 2. It should be noted that this equation describes a linear relationship between the property of interest and the volume fraction of each component and is shown graphically in Figure 17.

$$\boxed{P_T = P_1\phi_1 + P_2\phi_2} \quad \textbf{Equation 2}$$

However, a linear relationship does not always occur in blended or composite systems due to the effect of synergism Equation 3, which is represented empirically as 'I'. The effect of synergism is shown graphically in Figure 17, which shows that if I=0, the system is additive obeying the Rule of Mixtures. However, if I<0, the system is non-synergistic and a reduction in properties relative to the linear Rule of Mixture is expected, and for I>0, the system is synergistic and an increase in properties is expected.

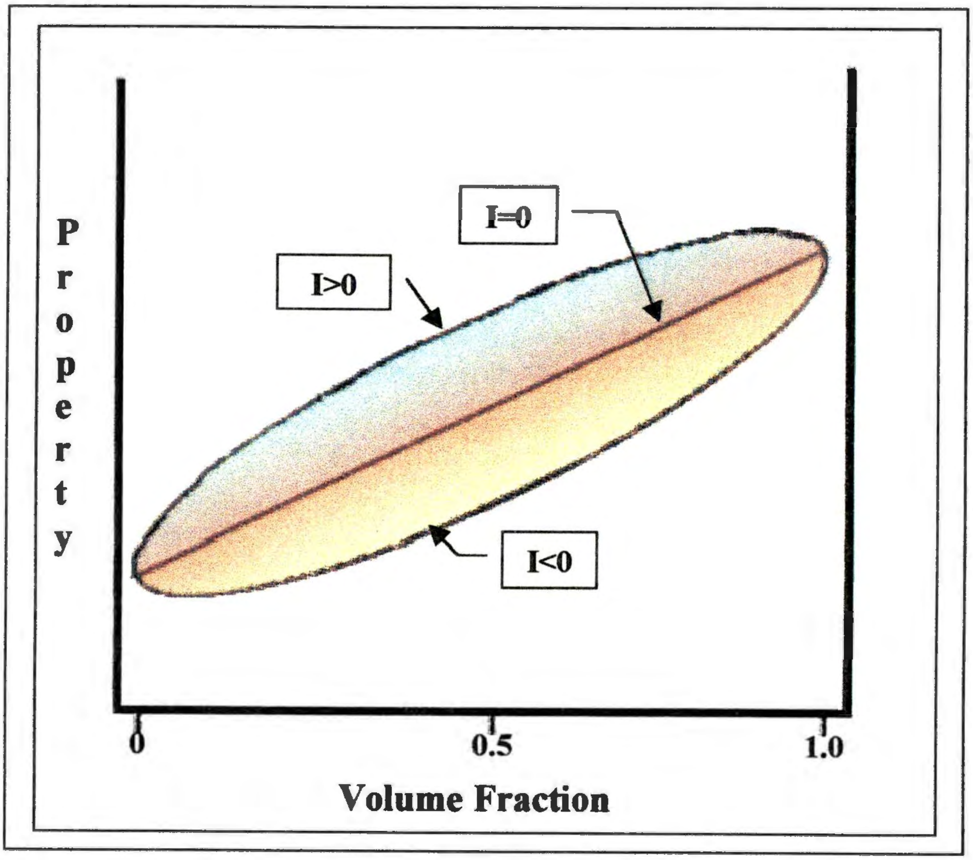

Figure 17. The Rule of Mixtures and synergism.

$$\boxed{P_T = P_1\phi_1 + IP_2\phi_2} \quad \textbf{Equation 3}$$

Where: $I = 4P_{12} - 2P_1 - 2P_2$

The Rule of Mixtures has been widely used to predict various mechanical properties such as stress, strain and modulus.[52,53] It has been applied to glass filled, fiber reinforced and polymer blended systems.

5.1.2 Fracture Mechanics

The use of fracture mechanics deals primarily with the effect a crack-like flaw has on the failure characteristics of a material under load. Linear elastic Fracture Mechanics, LEFM, is a mathematical approach that describes the fracture toughness parameter 'K' for materials that are linear elastic, that is, is has a linear stress-strain curve. The importance of the fracture toughness parameter is that it provides a way to evaluate the relationship between the applied stress and the flaw length. The evaluation of 'K' can be performed for a series of modes that a defect may undergo. The fracture toughness calculations are separated into three categories, Mode I, Mode II and Mode III, each describing the type of loading that is present around the crack tip. A sketch of each mode relative to the surface of the crack is shown in Figure 18. Mode I loading occurs when the crack surfaces move directly apart from one another. This mode is referred to as an opening mode. Mode II type loading is a sliding mode in which the surfaces of the crack slide over one another perpendicular to the leading edge of the crack tip. The final loading

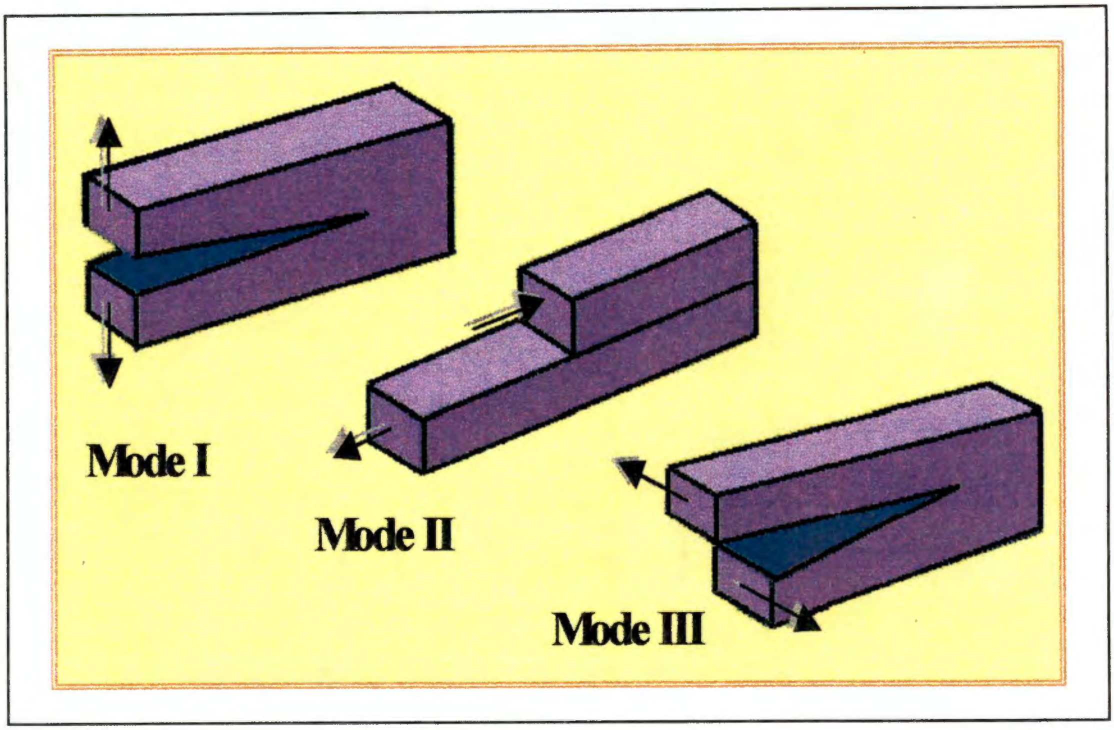

Figure 18. Basic Modes of Crack Surface Displacement.

Mode III describes a tearing mode in which the crack surfaces move away from each other parallel to the leading edge of the crack tip. The subscript of the stress intensity factor K_I, K_{II} and K_{III} represents the mode being evaluated. The stress intensity factor of a given mode describes the stress field that emanates from the tip of the crack under load. The stress field associated with each loading type is shown pictorially in Figure 19. The propagation of the crack is dependent upon the stress field reaching a critical state defined by the remotely applied load.

5.1.3 Linear Elastic Fracture

In the early 1920's Griffith[54,55] performed a set of experiments to evaluate the fracture strength of glass specimens containing small flaws. He concluded that the stress needed to cause failure decreased with an increase flaw size. He then developed an expression relating the critical stress, σ_{cr}, derived from an elliptical crack using the Inglis[56] strain energy solution to the flaw size shown in Equation 4:

$$\boxed{\sigma_{cr} = \sqrt{\frac{2E\gamma_S}{\pi a}}} \quad \textbf{Equation 4}$$

Where 'γ_s' is the crack surface energy of the material, 'E' is the elastic modulus, and 'a' is half the crack length of the center notch plate shown in Figure 20. The model is restricted to linearly elastic materials at absolute zero temperature. It does not account for the decrease of elastic moduli at higher stresses or the possible influence of other cracks in the specimen. At the time, these limitations were acceptable for many brittle materials and glasses where the mechanical behavior of the material at the use

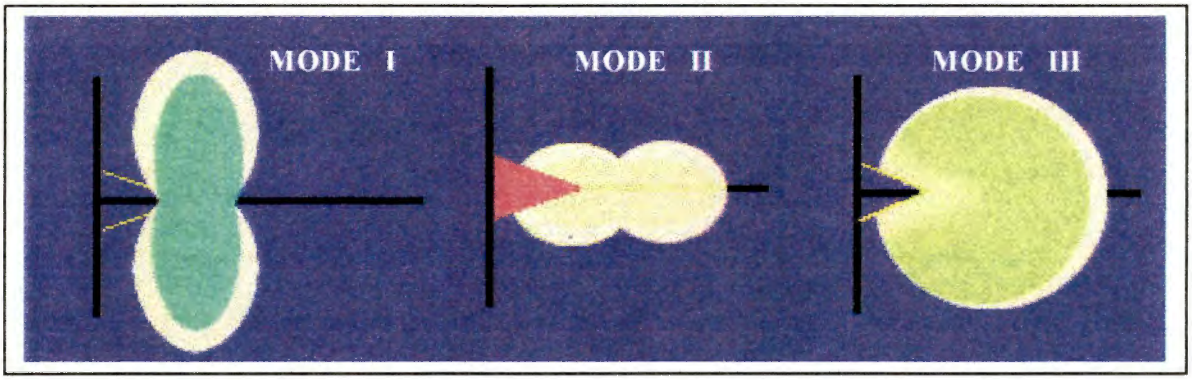

Figure 19. Stress field around crack tip for different loading modes.

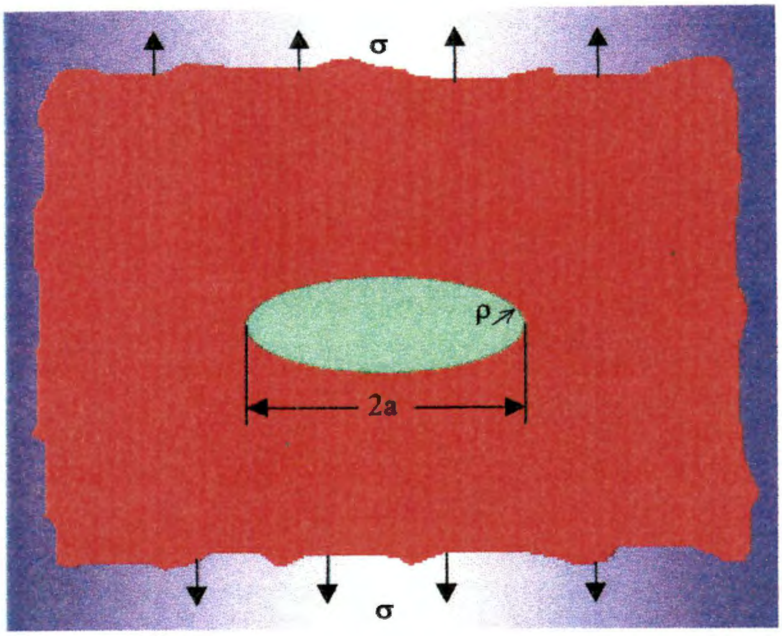

Figure 20. Mode I loading in an infinite plate.

temperature is similar to its behavior at extremely low temperatures (approaching absolute zero).

Bartenev and Zuyev[57] also noted that the time dependence of the mechanical properties of the material is not taken into account because of the temperature restriction. They pointed out a further shortcoming was that the definition of the critical stress was based on an energy balance which occurs only at equilibrium when the speed of the crack propagation is zero. It was noted that during crack growth, a large dissipation of energy occurs in the form of heat. On a more practical level, surface energy and other energy measurements were difficult to determine and of little practical use. Although there were limitations to the Griffith criteria, the energy model served as a basis for further studies in fracture mechanics using the stress field approach.

One of the more limiting disadvantages of the linear elastic analysis was that the model predicts infinite stresses at the crack tip when, in fact, plastic deformation occurs when the yield stress is exceeded. The plastic deformation precedes fracture and is a highly nonlinear elastic type behavior. To correct the linear elastic model, Orowan[58] modify the Griffith criteria to account for the energy associated with plastic deformation. The result was:

$$\boxed{\sigma_c = \sqrt{2E\frac{(\gamma_s + \gamma_p)}{\pi a}}} \qquad \textbf{Equation 5}$$

where γ_p is the plastic deformation energy term and

$$\boxed{\gamma_p >> \gamma_s}$$

In an independent study of the thermodynamics of fracture, Irwin[59] calculated a similar expression:

$$\boxed{\sigma = \sqrt{\frac{EG}{\pi a}}} \quad \textbf{Equation 6}$$

where 'G' is the strain energy release rate dU/da. The value of 'G' is therefore related to the plastic energy and the surface energy by $G = 2\,(\gamma_p+\gamma_s)$. In both studies, linear elastic energy balance models were modified to account for crack tip plasticity.

Although the energy balance models were theoretically correct, their applicability to design and engineering problems was limited. The studies did not lead to an understanding of material properties because they require a specific knowledge of flaw geometry and how stresses were applied to the flaw. Furthermore, it was difficult to measure and calculate surface energies and strain energy release rates during the design process if the location of flaws could be anywhere on the structure.

To address these shortcomings, it was desirable to develop a material parameter, which could describe the fracture properties of a material in various loading configurations. The analysis of the crack tip stresses lead to the material parameter, K, the stress intensity factor.

To determine the stress field Irwin substituted a Westergaard[60] stress function into equations of equilibrium for planar conditions. The model for this case is shown in Figure 21. The model determines stresses in two dimensions (x, y) with respect to an origin at the crack tip (r, θ). The results of the substitution are given by Broek:[61]

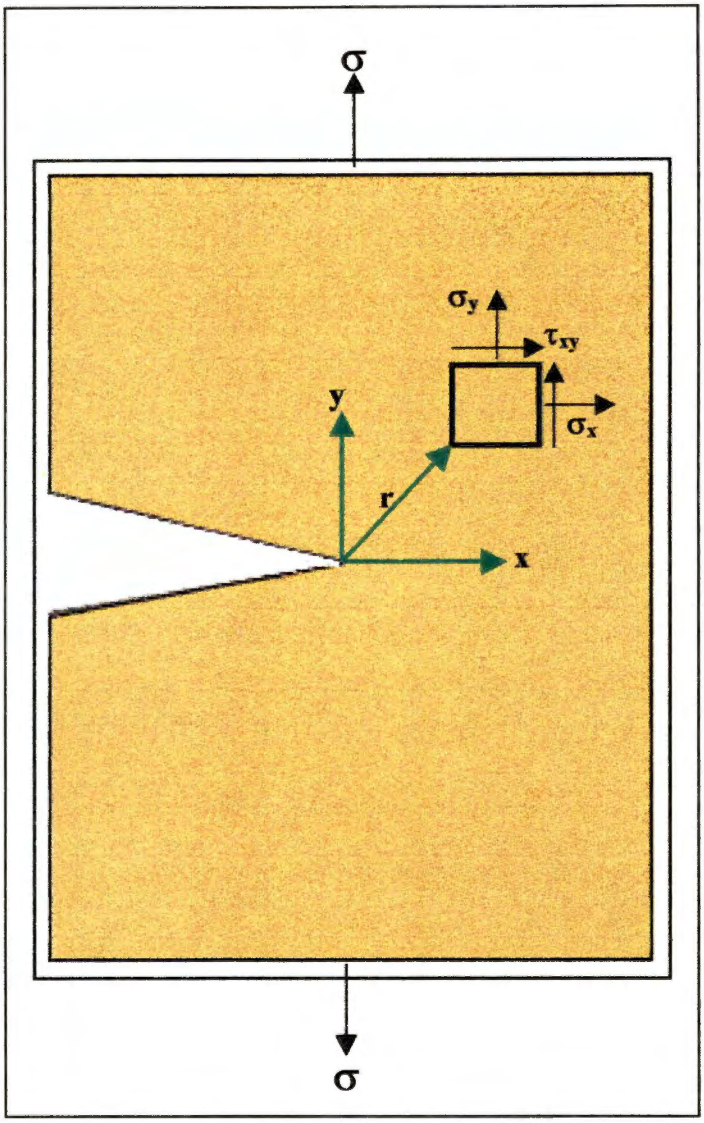

Figure 21. Planar conditions to determine stress distribution about a crack tip.[61]

$$\boxed{\sigma_x = \frac{K}{(2\pi r)^{\frac{1}{2}}}\cos\left(\frac{\theta}{2}\right)\left[1-\sin\left(\frac{\theta}{2}\right)\sin\left(\frac{3\theta}{2}\right)\right]}$$

Equation 7

$$\boxed{\sigma_y = \frac{K}{(2\pi r)^{\frac{1}{2}}}\cos\left(\frac{\theta}{2}\right)\left[1+\sin\left(\frac{\theta}{2}\right)\sin\left(\frac{3\theta}{2}\right)\right]}$$

Equation 8

$$\boxed{\tau_{xy} = \frac{K}{(2\pi r)^{\frac{1}{2}}}\cos\left(\frac{\theta}{2}\right)\sin\left(\frac{\theta}{2}\right)\cos\left(\frac{3\theta}{2}\right)}$$

Equation 9

$$\boxed{\tau_{xz} = \tau_{yz} = 0}$$

Equation 10

$$\boxed{\sigma_z \approx \upsilon(\sigma_y + \sigma_x)}$$

Equation 11

(Plane Strain)

$$\boxed{\sigma_z = 0}$$

Equation 12

(Plane Stress)

Where 'v' is Poisson's ratio and 'K' is the stress intensity factor which is a material parameter that is a function of the applied stress and crack geometry. It is important to note in these equations that stress is proportional to a geometry term (θ) and inversely proportional to $r^{1/2}$, thus the singularity at the crack tip is still present. This model is applicable to materials, which display linear elastic behavior under test conditions. This is often true of glassy polymers.

The critical stress intensity factor, K_{IC}, is the minimum value of 'K', which will cause a crack to propagate to failure instantaneously under normal stresses; the subscript 'c' denotes that 'K' is at a critical value. It is given by:

$$\boxed{K_{IC} = \sigma_{cr}\sqrt{\pi a_{cr}}\, f\left(\frac{a}{w}\right)} \qquad \textbf{Equation 13}$$

where 'σ_{cr}' is the critical stress for crack propagation. Values of K_{IC} are parameters unique for a material and specific crack geometry. K_{IC} is commonly used as a fracture criterion.

Another aspect of crack tip phenomena is the effect of crack tip radius. The crack tip as illustrated in Figure 20 is a mathematical response represented by the term K_t, stress magnification factor, shown in Equation 14. The crack length is referred to as '2a' and the stress as 'σ'. The crack tip radius is inversely proportional to the stress concentration observed at the crack tip. Therefore, there is an increase in the stress at the crack tip(s) due to the presence of a crack (Equation 14). The importance of Griffith's approach became evident in the 1940's when ships crossing the North Atlantic literally broke in half. Such failures were found to be caused by voids in the ship's welded hull. Since the 1940's, LEFM has become a widely accepted failure analysis for the engineering community and is in general use in many areas, including

$$\boxed{K_t = \frac{\sigma_m}{\sigma_o} = 1 + 2\left(\frac{a}{\rho_t}\right)^{\frac{1}{2}}} \qquad \textbf{Equation 14}$$

ASME Codes, Regulatory guides, material specifications, and industry design manuals.

5.1.4 K-Solutions

The use of fracture toughness as mentioned in the previous section deals with a single crack in a plate. Real life situations do not have such ideal cases, which is believed to have influenced the development of a series of possible crack configuration solutions by Tada, Paris and Irwin.[62] These solutions aid a designer in the stress analysis of a structure with a flaw and even a series of flaws. These solutions are known as K-solutions for which K_I, K_{II} or K_{III} can be evaluated. Equation 15 and Equation 16 are K-solutions for parallel and in-line crack configurations, respectively. These equations helped establish a possible predictive tool for the evaluation of K_{IC}, which will be discussed in greater detail in the discussion section.

$$\boxed{K_I = \sigma\sqrt{\pi a}F(s)}$$

Equation 15
Parallel cracks

$$\boxed{K_I = \sigma\sqrt{\pi a}\sqrt{\frac{W}{\pi a}\tan\frac{\pi a}{W}}}$$

Equation 16
In-line cracks

Where:

$$\boxed{F(s) = \sqrt{\frac{1-s}{\pi s}}}$$

$$\boxed{s = \frac{a}{a+h}}$$

2a = average void length
h = average distance between voids
W = the mean distance between voids

VI. EXPERIMENTAL

6.1 Sample Preparation

The Structural Reaction Injection Molding, SRIM, process, produced a 25 x 25 x 0.125 in. plaque. The matrix was formulated and designated by Dow Chemical Company as DOW MM364. These plaques were cut into specimens with the following dimensions 1 x 8 x 0.125 in. The specimens consist of an isocyanurate based polyurethane matrix and a continuous swirled E-glass mat. The mat, a Certainteed/Vetrotex Unifilo U750 reinforced mat consisted of approximately 300 monofilaments per bundle. The fibers are approximately 17μm in diameter. The mat used to make the plaque consisted of five individual layers resulting in a fiber content of approximately 40% by volume. The cut specimens had tabs attached using BF Goodrich A-1177-B1-B2 two part adhesive.

6.2 Testing

6.2.1 Ultrasound

Ultrasonic C-scans were performed using a SONIX ultrasonic scan system. The scans were conducted in a water bath at room temperature. A 15 MHz transducer was focused on the back surface of the specimen being probed. A 0.4 mm incremental scan was used to obtain the amplitude map. The amplitude map was then analyzed using Adobe PhotoShop ®.

6.2.2 Image Analysis

Video recording and still images were collect using a Sony CCD color camera with a video microscope lens. The video microscope had an adjustable magnification range from 1X to 5X.

Image analysis was conducted using NIH image and Adobe Photoshop® software packages. NIH image enabled the measurement of void content and void orientation as well as the real-time evaluation of crack initiation, propagation and termination.

Adobe Photoshop® was used to evaluate the digitized attenuation maps produced from Ultrasonic C-scans. The histogram function was used for same area measurements to obtain a single value for the average gray scale. This value is then related to the degree of damage.

6.2.3 Tensile Loading

Tensile tests were conducted at room temperature in air. A Hydraulic MTS axial-torsion mechanical testing machine together with an MTS digital TestStar material testing workstation was used for computerized testing and data acquisition. Displacement in the gage section was measured with an MTS clip-on extensomenter of 1.0 in. gage length. Samples were 1x 8 x 0.125 in. (W x L x T) straight edge specimens. The load, displacement, and time were measured and recorded. Sample dimension and testing was performed in accordance with ACC test methods and ASTM D638 and D882.

The purpose of the tensile tests is two fold. First, these test were conducted to obtain an overall response of the composite mechanical properties; and secondly, to introduce a controlled level of damage by incrementally loading the specimen. After each incremental loading the specimen would undergo ultrasonic C-scans.

6.2.4 Horizontal Hydraulic Tensile Tester

A horizontal hydraulic tensile tester, shown in Figure 22, was design and fabricated in the Material Science and Engineering Department at the University of Tennessee. The design allows for the real-time evaluation of crack propagation under the objective lens of a video microscope during Tensile and Creep tests. The design enables a 360° rotation of the specimen while under load as well as movement in the X-Y directions. This tensile tester uses a 10k lb. load cell and a double action hydraulic cylinder, which can generate loads up to 10k lb. The load cell is monitored by a PowerMac 7600/120 via Iomega InstruNet 100 or LabView software. The data acquisition occurs simultaneously during the real-time image capturing of damage events.

6.2.5 Creep Loading

Creep test were conducted at room temperature (approximately 75°F) and in ambient air (approximately 50% RH). Specimens are mounted in a calibrated lever creep machine having a lever arm ratio of about 12:1. Strain was measured using strain gages produced by Micro-Measurements Group, Inc. and designated as "CEA-13-500UW-350" a ½ inch gage length was used during testing.

6.2.6 Fatigue

Fatigue experiments were conducted using a servo controlled MTS testing workstation with data acquisition system. Two different fatigue tests were conducted.

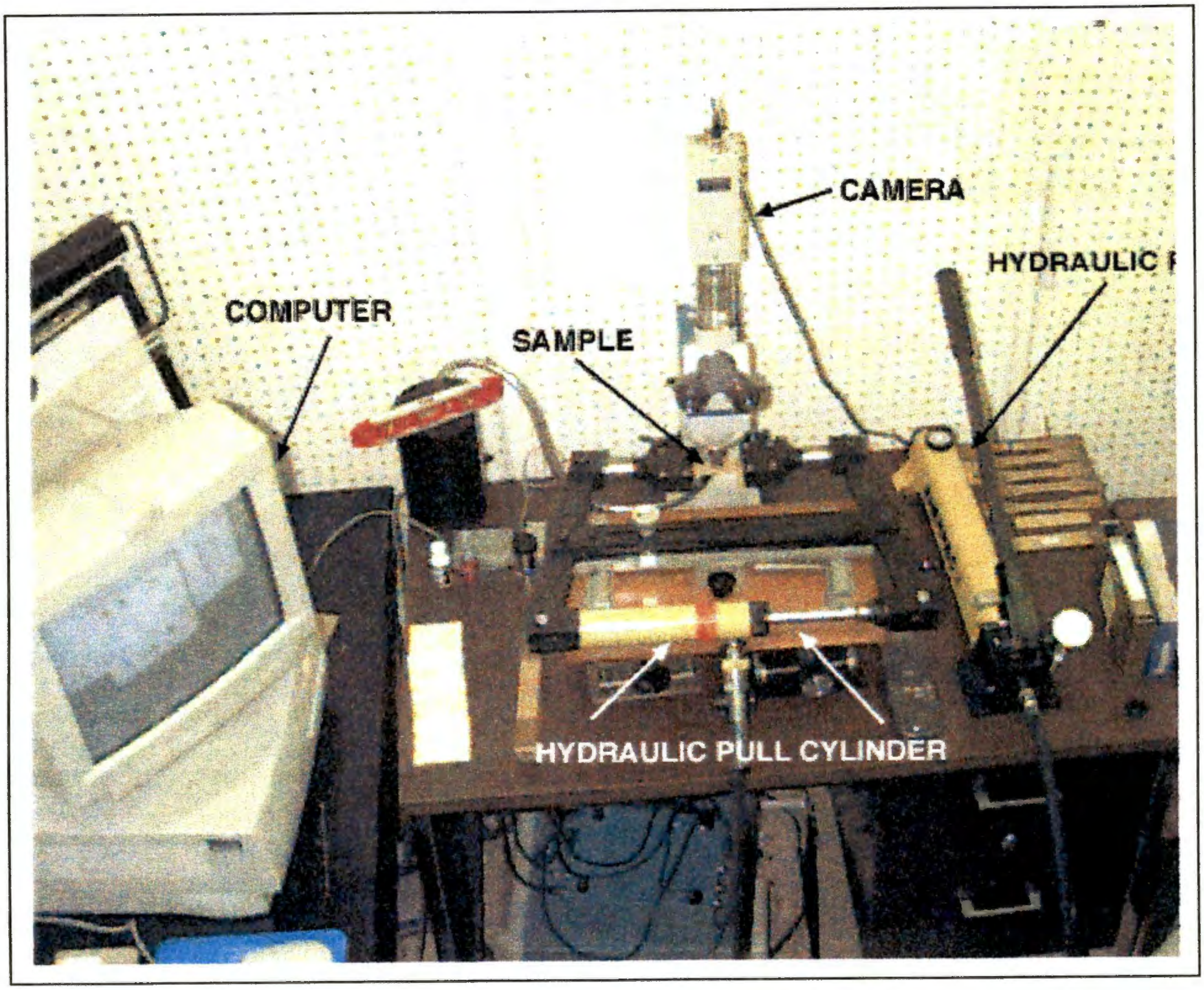

Figure 22. Hydraulic Tensile Tester and Setup.

First, normal tension-tension profiles from 0%-27.9% UTS, 0%-42% UTS, and 0%-55% UTS were performed on a series of specimens. The second tests were optical studies in which specimens were fatigue loaded with a tension-tension profile from 0%-40%UTS for 5, 100, 1000 and 3000 cycles. After each cycling segment the specimen was removed and inspected optically. The samples used in the latter experiments had the same geometry as other tensile test, however, a 0.25 in. hole was drilled in their center.

6.2.7 Fracture Toughness

An MTS 810 hydraulic test system was used to perform the fracture toughness measurements. This system is automated by Testware® software package, which also has data acquisition capabilities. The crosshead speed was 0.06 in/sec with 100 data points were collected per second. The specimens were held in place during testing by the 1/2T sample fixture. These tests were conducted at room temperature and a relative humidity of approximately 50%. Samples were fabricated using ASTM E 1820 and pre-cracked using a razor blade.

6.2.8 Void Volume

In order to obtain the void volume, a section of the continuous swirl mat composite was removed from the center gauge length of a tensile specimen. This section was thinned and length, width and thickness measured. The purpose for thinning the sample was to capture as much of the cross-section as possible using light microscopy. This thinned section was then placed under the video microscope and imaged. The collected image, which shows the presence of voids and fibers, was analyzed using NIH software. The software was set-up to select voids. The voids selected were then measured for their major and minor axes. The major and minor axes were then used to calculate the volume of the void assuming an ellipsoid or sphere using Equation 17.

$$\boxed{V = \frac{4}{3}\pi a^2 b}$$

Equation 17

a= minor axis
b=major axis

VII. RESULTS

7.1 Mechanical Properties

7.1.1 Tensile

Tensile tests showed that the average ultimate tensile strength, UTS, is 25.2 ksi in the 90° direction and 20.4 ksi in the 0° direction. An average stress strain curve, along with actual data points from a series of experiments for the CSMC in the zero direction, is shown in Figure 23. The direction refers to the take-up of the glass mat. Hence, the 0° direction refers to a sample that was cut from the plaque in the direction equal to the roll or conveyance of the fibrous mat. The 90° direction refers to a specimen cut out perpendicular to the roll direction.

The reduction in the modulus was determined by loading a specimen at a percentage of the UTS then unloading it followed by loading to complete failure. This process performed the controlled degradation of stiffness. The results of the experiments are summarized in Figure 24. It was found that an onset of modulus reduction occurred at approximately 30%UTS. There is roughly a 20% reduction in modulus as the UTS is approached.

7.1.2 Creep

The tests conducted at room temperature and a relative humidity of 50% had a creep response as shown in Figure 25. Figure 25 is the creep strain vs. time plot. The total strains are provided in Appendix D. The creep strain response produces a typical creep curve expected with increasing applied stress, that is, as the applied stress increases

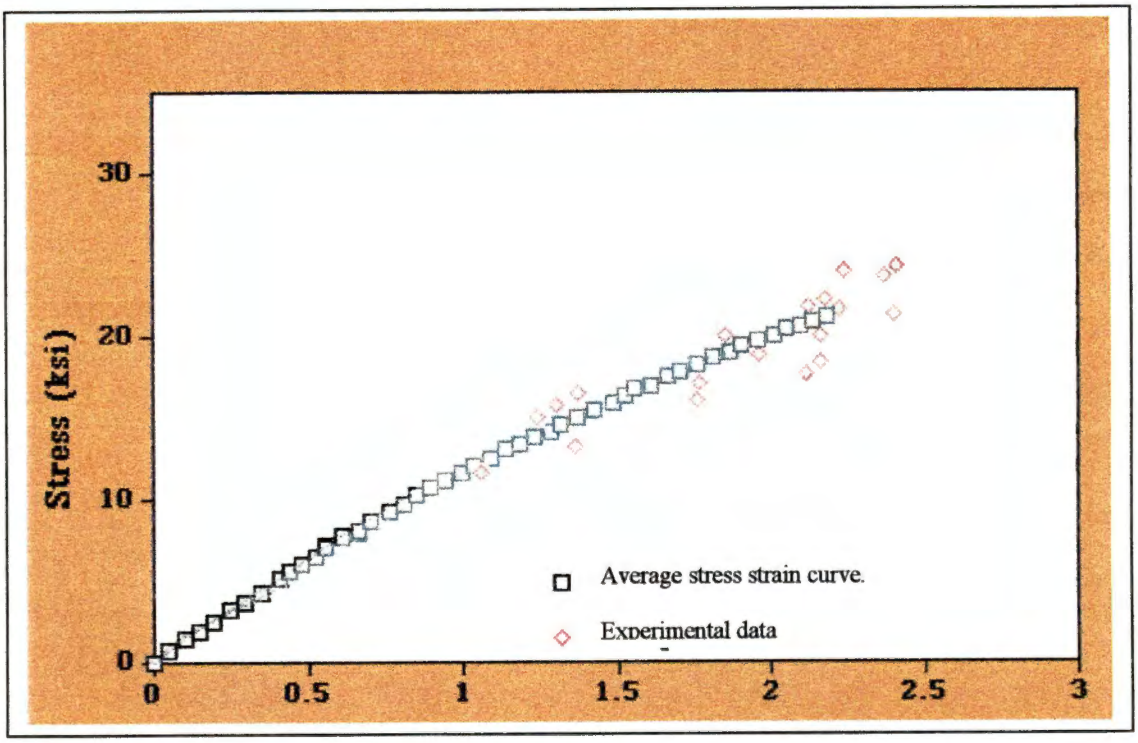

Figure 23. Typical stress-strain curve of a CSMC in the 0° direction.

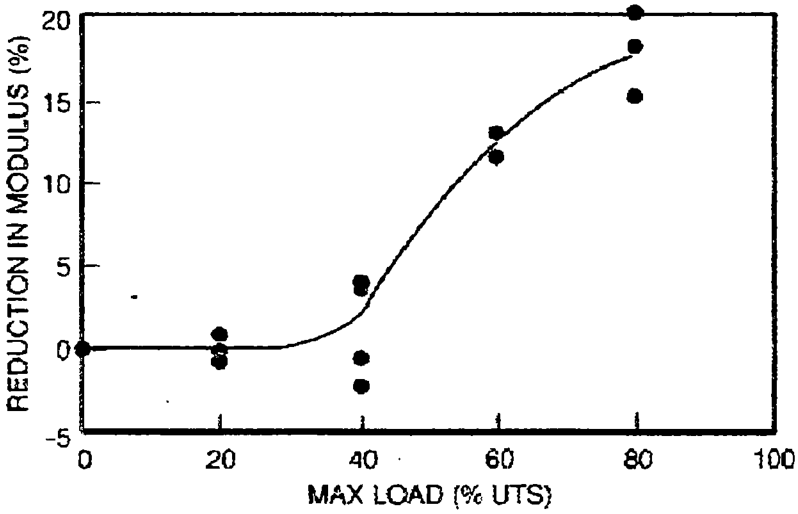

Figure 24. Modulus reduction as a function of load level[63]

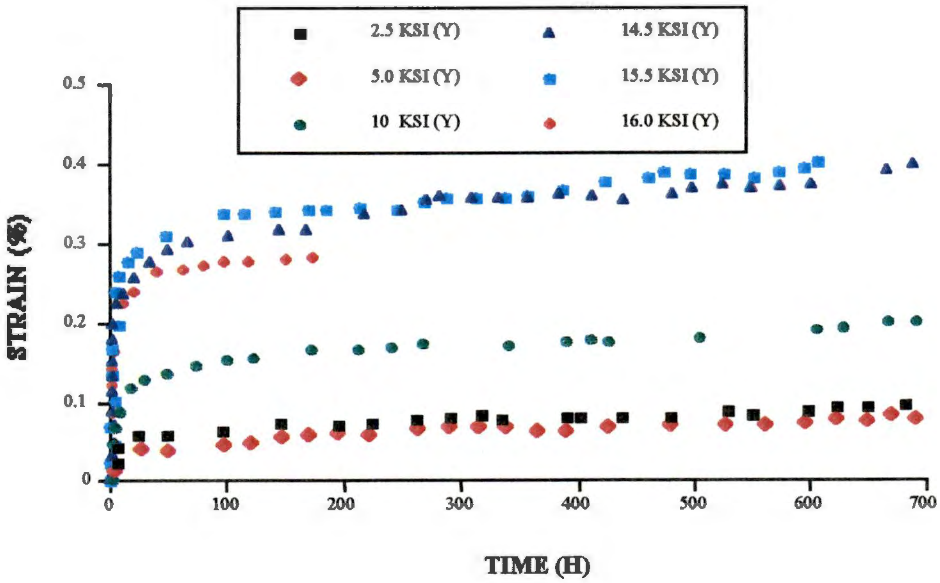

Figure 25. Creep response in air at room temp and 50% RH.

there is an increase in the creep strain. The development of a primary creep stage (STAGE I) occurs at approximately 5.0 ksi, which is ~25% of the UTS. Below 14.5 ksi the CSMC has unlimited creep capabilities as indicated by the secondary creep stage (STAGE II) and will not fail in creep at that stress level. Above 15.0 ksi rupture is shown to occur at ~600hrs. As the applied stress is increased there is a reduction in the time to rupture.

7.1.3 Fatigue Tests

The effect of increasing the tension -tension cycle is shown in Figure 26. The notable features are the steady state of the initial slope of each individual curve regardless of the applied cyclic load followed by a rapid increase in strain towards the end of the life cycle. A common point in each individual curve was determined by taking the slope of each segment of the curve, that is, the steady state and rapid increase segments. Where these two slopes intersect was termed the critical point. It should be noted that the critical point occurs at a different number of cycles for each percent UTS tension-tension curve. The critical point represents the onset of increased damage accumulation rate, which is thought to be associated with fiber breakage and pullout. It is also shown in Figure 26 that an increase in percent UTS results in a shift in the critical point to lower cycles to failure. To the right of the critical point and with increasing percent UTS there is an increase in the rate of damage.

A specimen with a 0.25 in hole drilled in its center was subjected to cyclic loading. A series of images with the applied load perpendicular to the radius of the drilled hole, which is the region of greatest stress were collected at 0, 100, 1000 and 3000

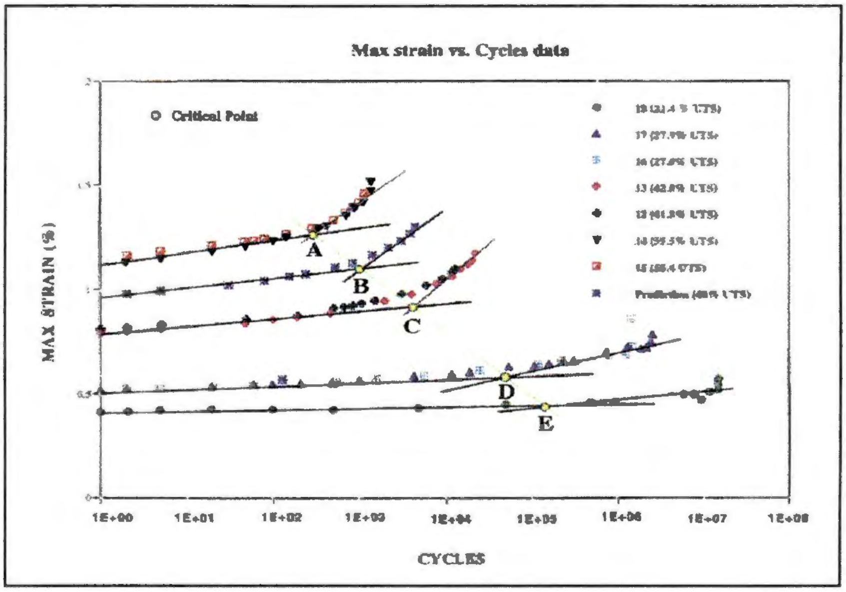

Figure 26. Maximum Strain vs. Cycles to failure.

cycles and are shown in Figure 27. This image shows the accumulation of damage around the drilled hole with increasing number of cycles, while A, B and C are reference markers indicating the same area of observation for each series. This sample allowed the early identification of damage events in regions of greatest stress shown pictorially in Figure 28. Damage was observed to be dependent on the number of cycles. The more noticeable damage was observed above 1000 cycles.

7.2 Ultrasound

7.2.1 Ultrasonic C-scan for Tensile specimens

The following results are from ultrasound showing the average attenuation map of tensile samples. It is shown in Figure 29 and Figure 30 that an increase in percent UTS from 20% - 80% UTS loading resulted in a decrease in the average grayscale value, AGV. A graphical representation of the change in AGV with percent UTS is shown in Figure 31. It indicates a continued decrease in AGV with increasing percent UTS. The percent difference of the AGV at 0% and 100% loading indicates the relative degree of damage to be approximately 29%.

7.3 Image Analysis

Observation of 1 x 8 x 0.125-inch specimens that were not subjected to any loading show common features under transmitted light microscopy. The most common feature is air voids. The voids in the matrix appear as spheres or agglomerations of spheres. Those voids that occur near the fiber bundles are elongated along the fiber axis.

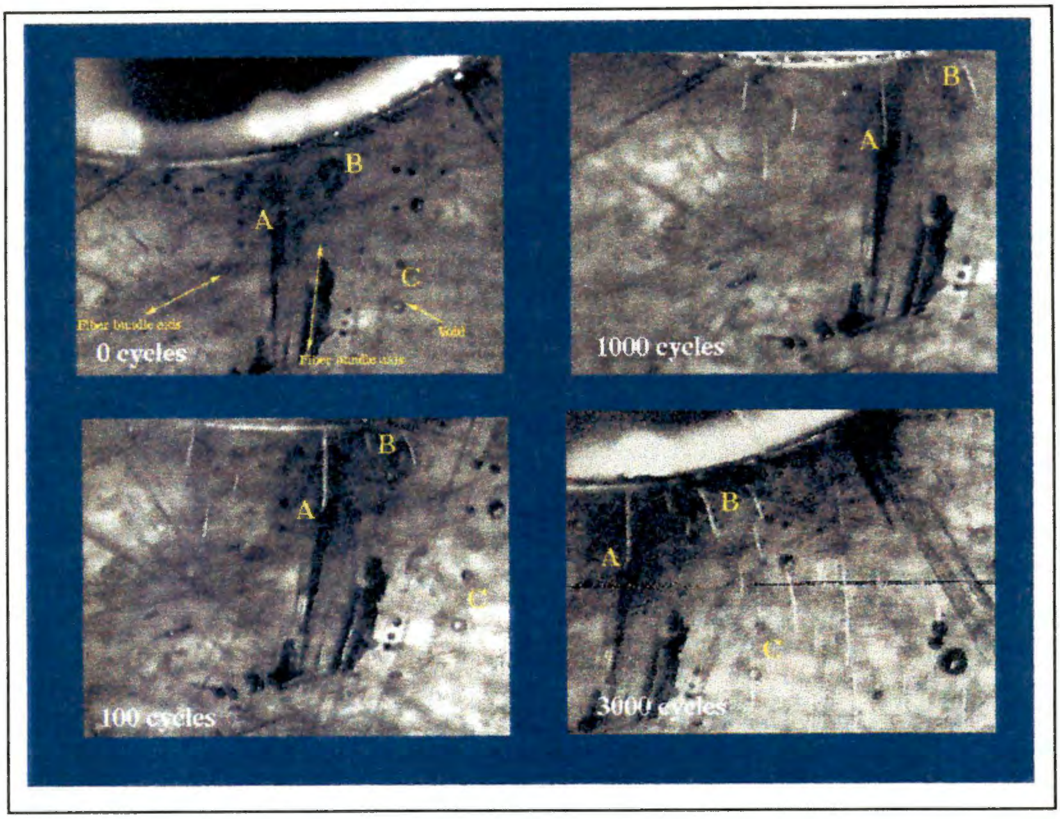

Figure 27. Observed damage using optical micrographs with increasing cycles.

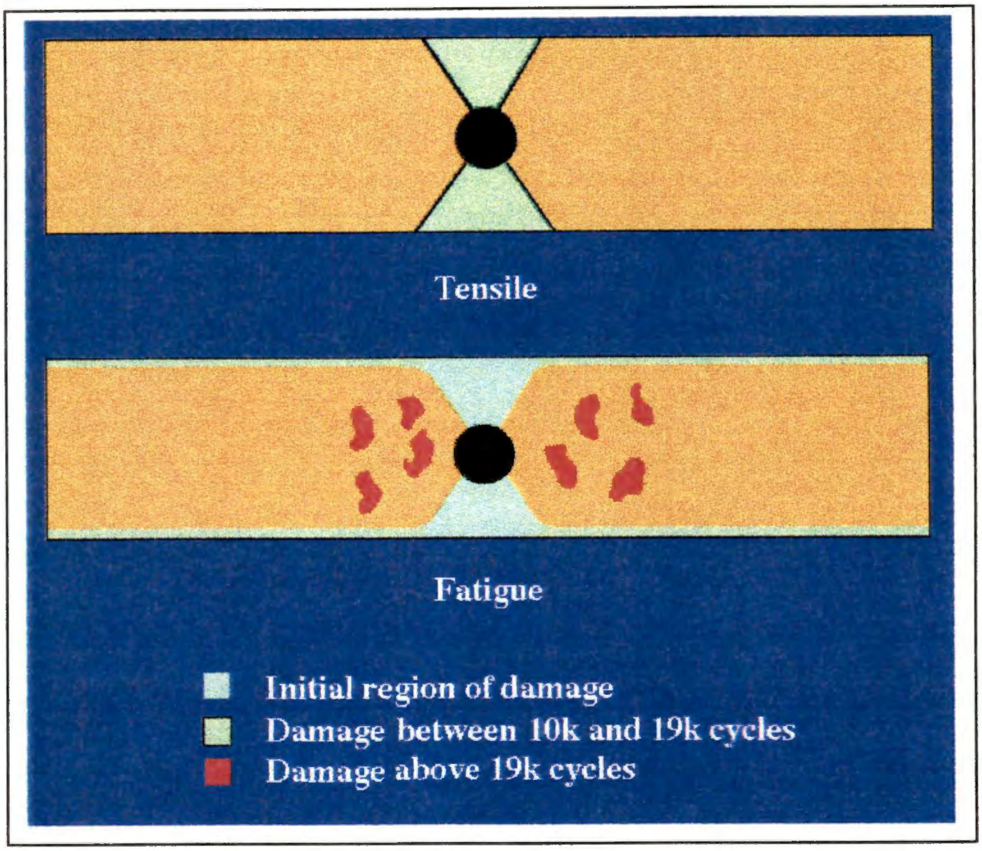

Figure 28. Regions of accumulated damage with increasing cycles.

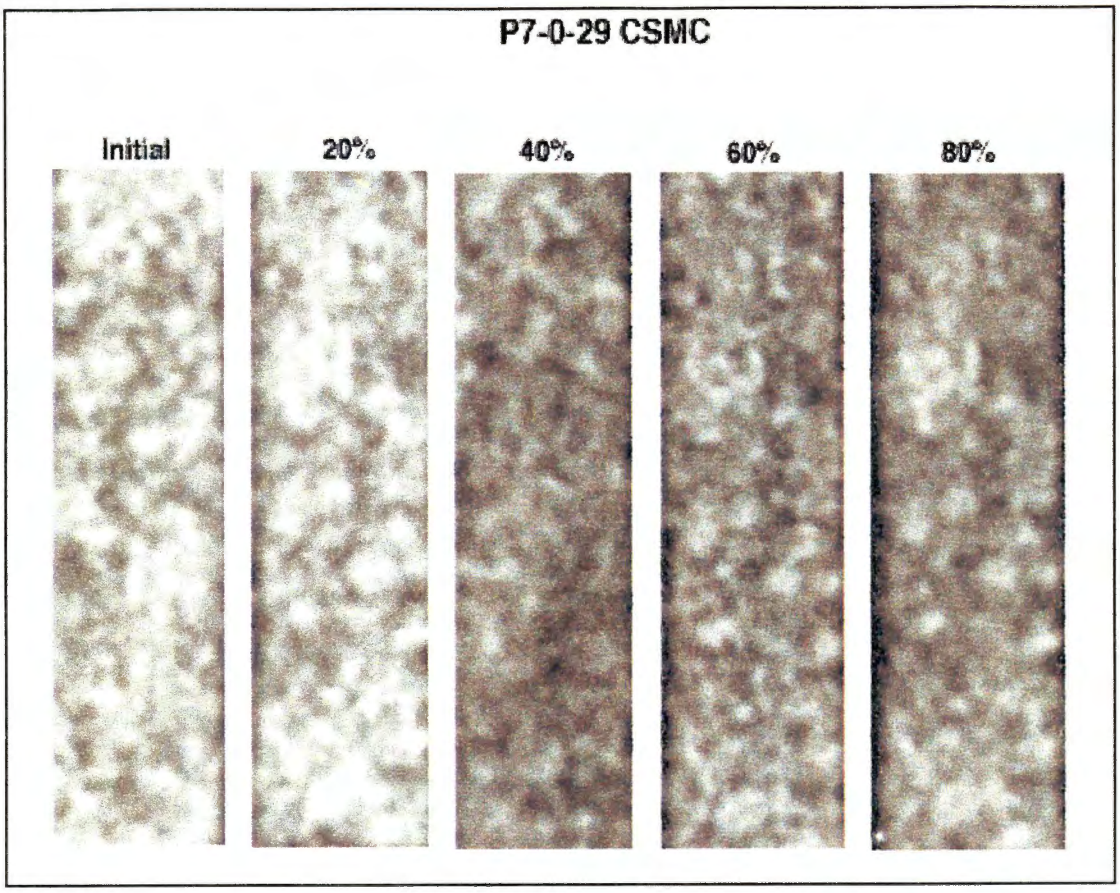

Figure 29. C-scans of incremental UTS tensile loading.

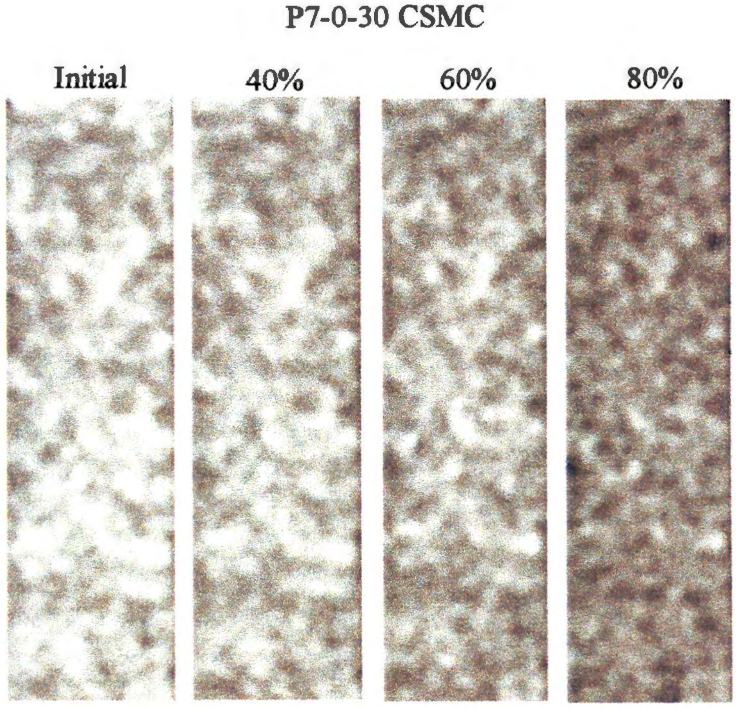

Figure 30. C-scans of incremental tensile loading.

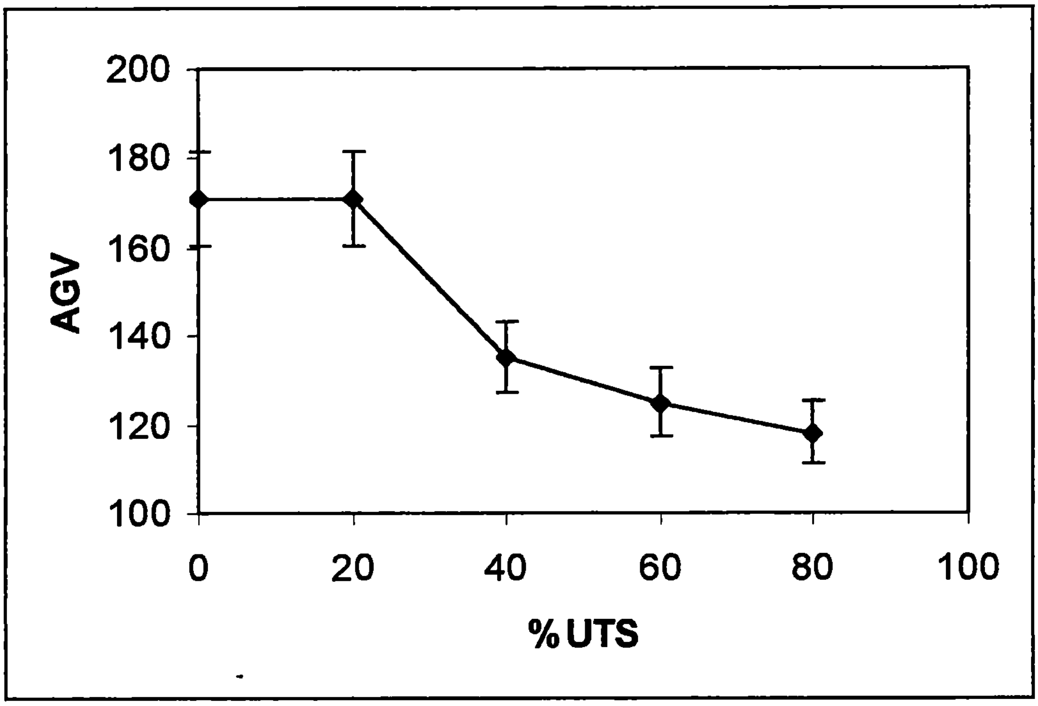

Figure 31. Plot of Average Grayscale value, AGV vs. UTS.

These intrinsic voids are due to off gassing during the SRIM process. The voids tend to act as stress risers, thus affecting the crack propagation in the CSMC.

The other feature to note is the elongated voids along the fiber bundles shown in Figure 32. The presence of elongated voids depicted by the dark area along the bundle axis is indicative of incomplete fiber wetting by the coating or coupling agent. The dark areas along the bundle axis are areas where fiber wet-out is incomplete. This was verified by imaging the mat using SEM. The bundles were coated prior to the SRIM process, yet the coating was not evenly distributed over the entire surface of the fiber see Figure 33 and Figure 34. Incomplete wetting of the fiber bundles and solidification of the coupling agent appears as globs along the bundle axis as shown in Figure 33 and Figure 34. These features make the identification of debonding difficult to verify after loading as well as with the virgin specimens. This difficulty arises from the initial condition of the glass mat, that is, defects as previously stated and shown in Figure 32. When the polymer encapsulates the mat and these features exist, they are technically points of debonding; however, they are intrinsic due to processing and are not due to the applied load.

7.3.1 Image Analysis and SEM

In some cases fracture areas were examined using scanning electron microscopy. In SEM, a beam of focused electrons moves across the sample, and the secondary electrons produced by the sample and the electrons scattered by it are collected to form a three-dimensional image. At low operating voltages (usually less than 2 KeV), the

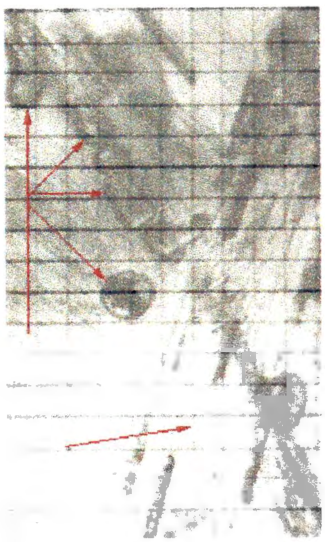

Figure 32. Voids and fiber bundle.

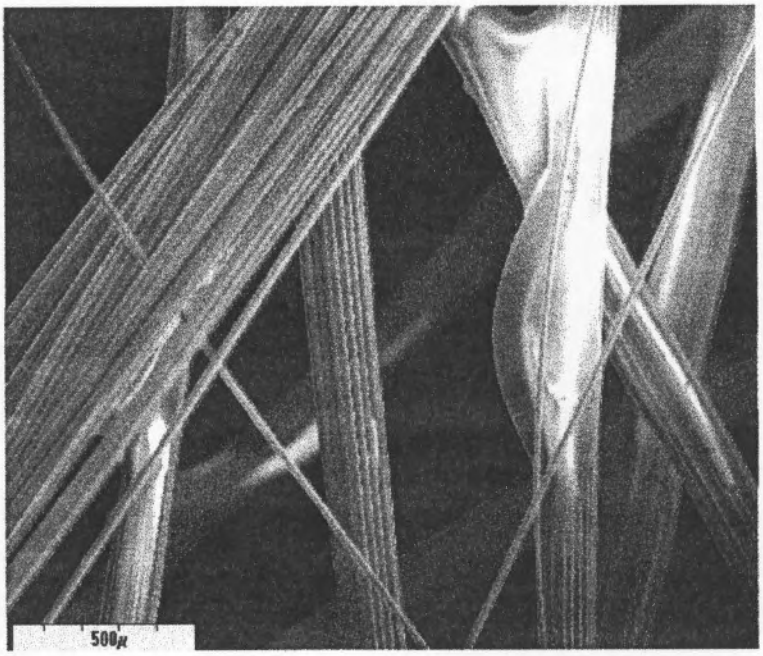

Figure 33. The incomplete fiber wetting and sizing globs prior to processing.

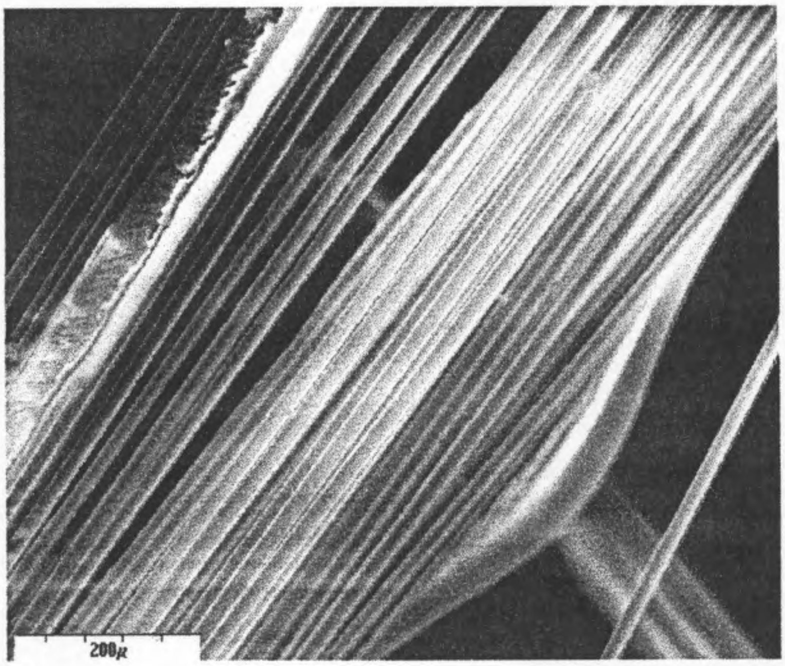

Figure 34. The glass mat prior to processing.

surface of an uncoated CSMC sample can be observed. Commonly observed characteristics of CSMC fracture include matrix cracking (sometimes in the form of river patterns), fiber/matrix interfacial debonding, fiber pull-out, and fiber breakage. The SEM images for CSMC sample P21-0-25 display some of these features. In Figure 35 and Figure 36, the fracture surface is viewed from the top of the sample. Some fiber breakage and matrix cracking are apparent in each of the images, and some debonding can be seen in Figure 36. Matrix cracking can be seen as river patterns at the edge of the fracture surface, emanating from fiber bundles in Figure 37 and Figure 38.

7.3.2 Image Analysis and Real-time observation

Real-time image analysis provided observations into the progression of damage. The formed crack as shown in Figure 39 was followed in real-time with load control in tension to determine what the path of progression or formation of damage is, and how it would assist in the development of a failure mechanism. Shown in the following images are reference markers 'A' and 'B' that can be followed from image to image. Figure 40 shows the opening of the crack pictured in Figure 39 until it is halted momentarily by the fiber bundle as indicated in Figure 40. Figure 41 shows the progression through and around the fiber bundle. This is indicated in the image by the dark regions in front of crack, which are associated with fiber/fiber and fiber/matrix debonding as well as fiber breakage. The specimens used in real-time studies enabled crack growth of only a few mm before unstable growth occurred, which would end the real-time observation.

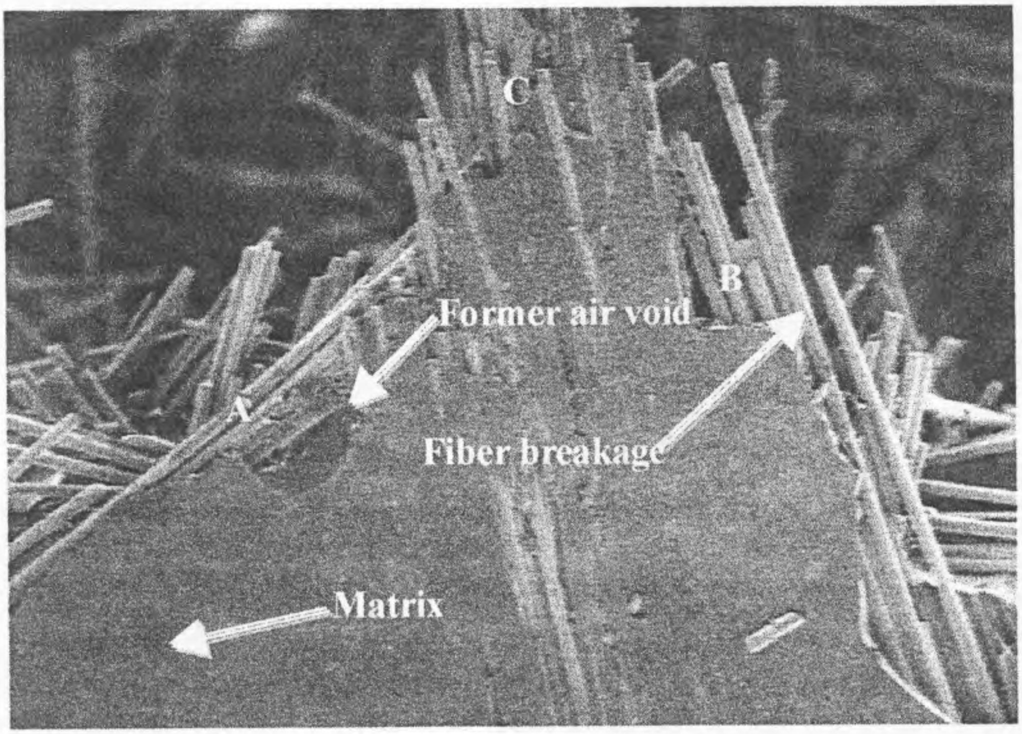

Figure 35. Fracture surface top view P21-0-25 1.5 KeV, 70x.

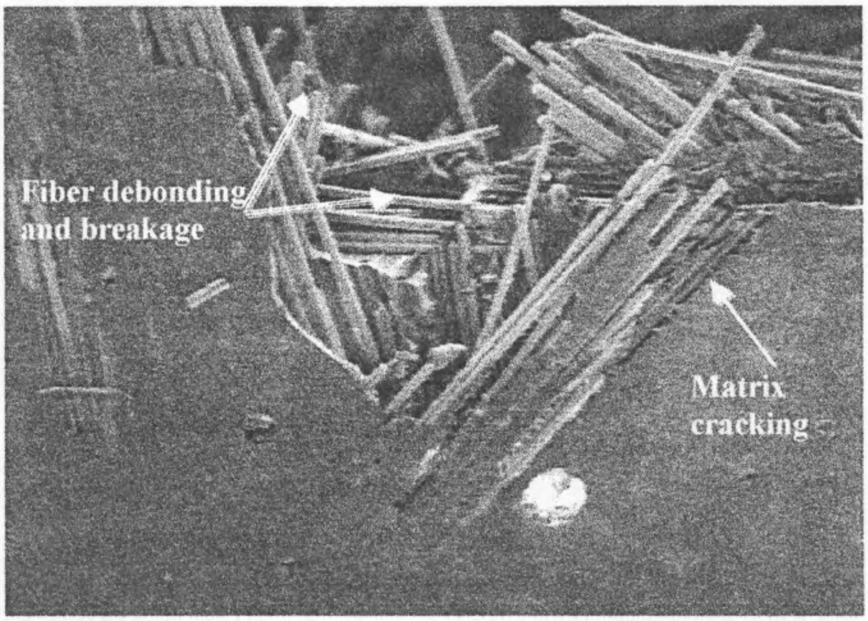

Figure 36. Continuation of fracture surface in Figure 29 P21-0-25, 70x.

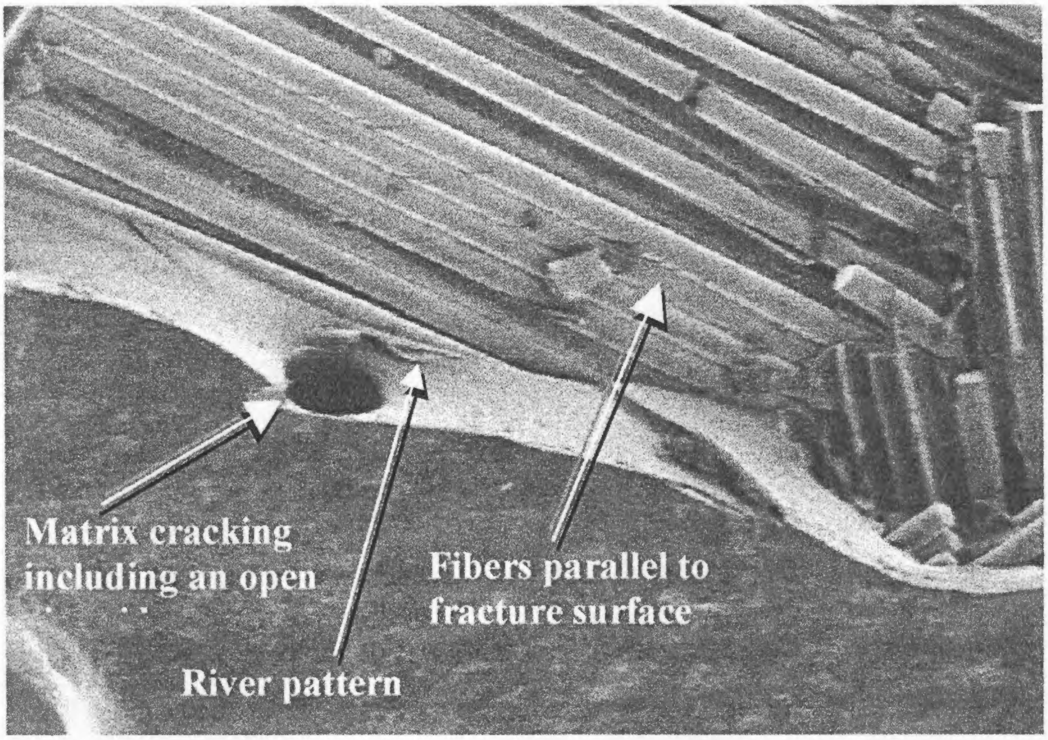

Figure 37. Void on fracture surface P21-0-25, 1.5 KeV, 300x.

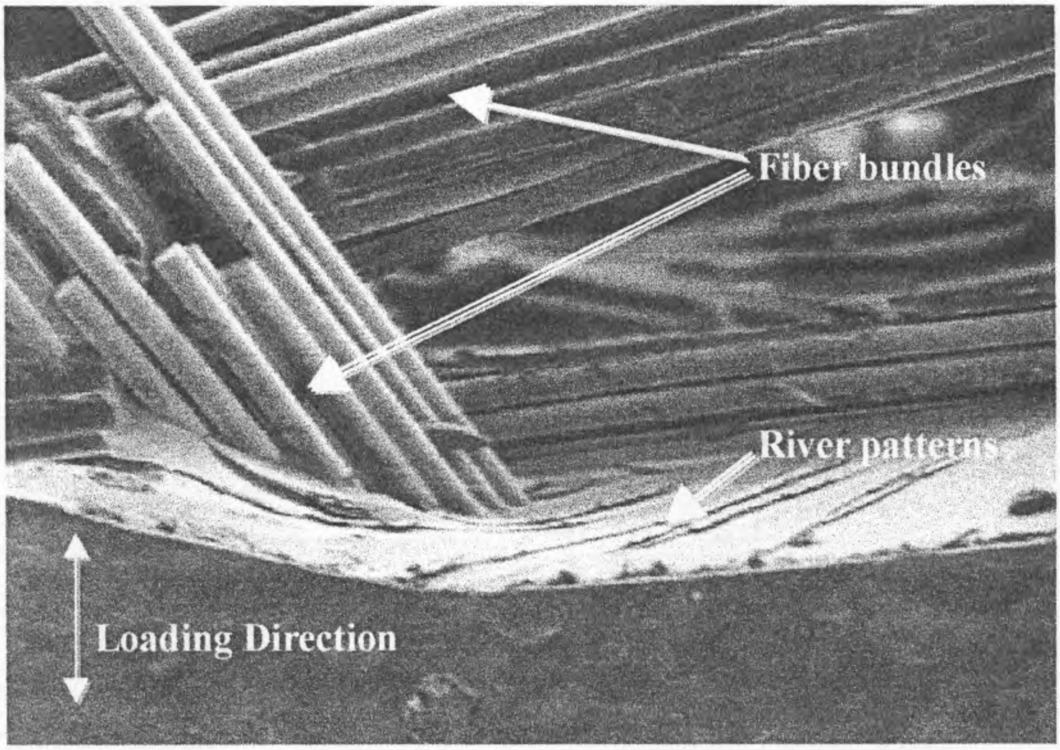

Figure 38. River pattern on fracture surface, P21-0-25, 1.5 KeV 300x.

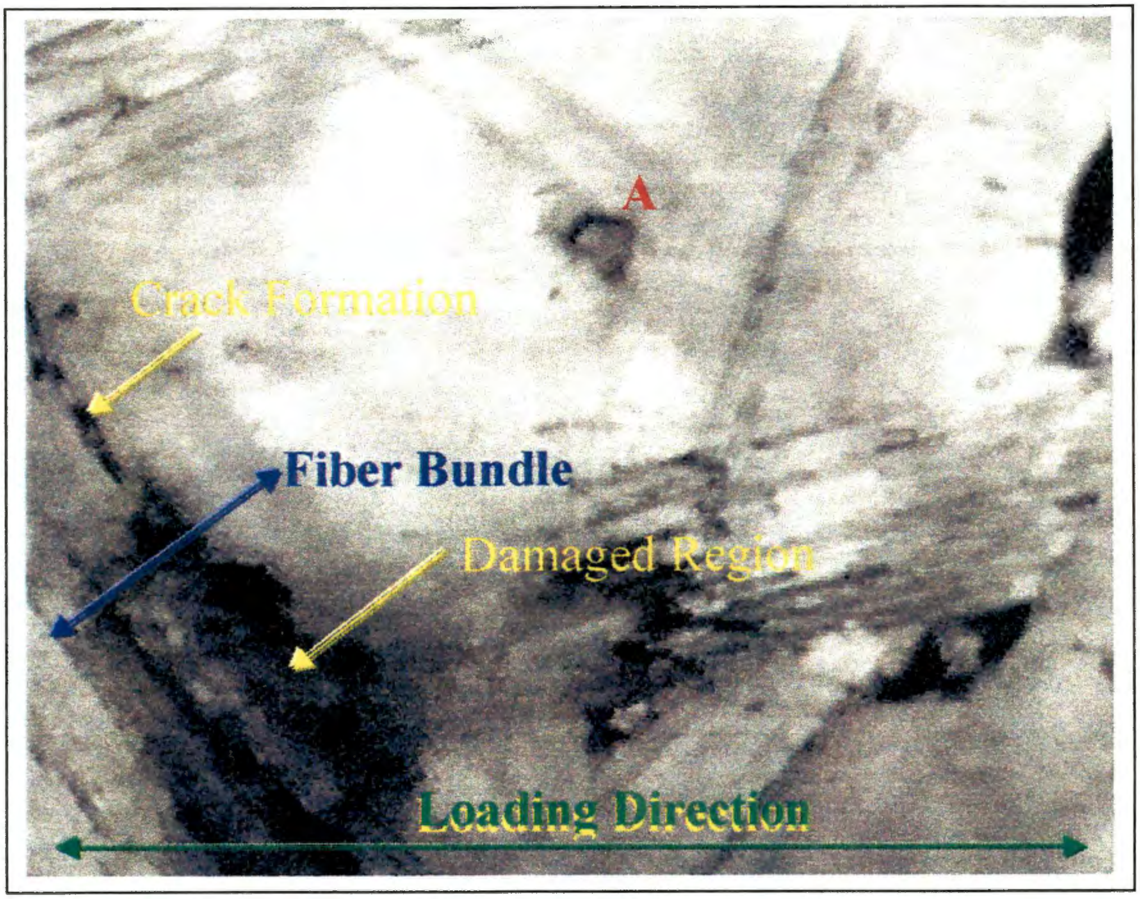

Figure 39. Initial observation of crack formation.

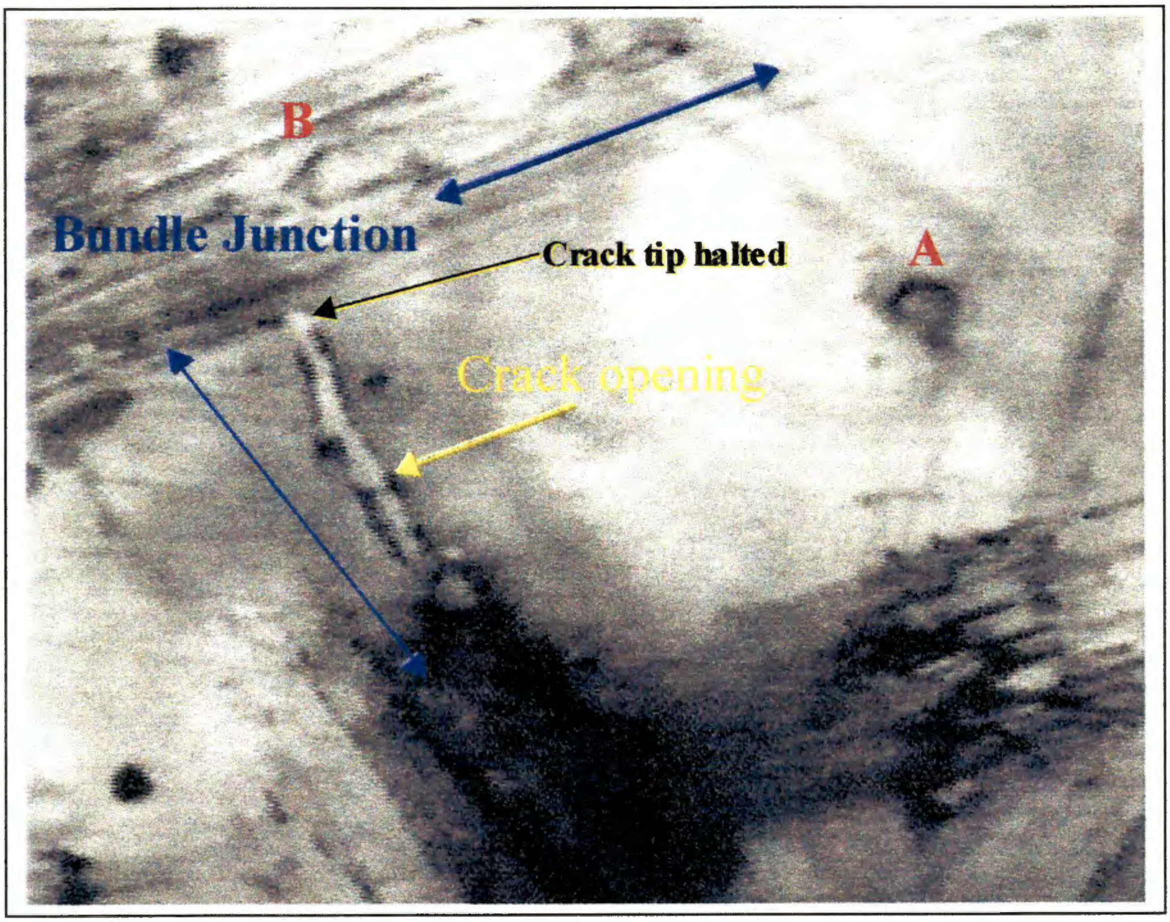

Figure 40. Continuation of crack growth and damage formation.

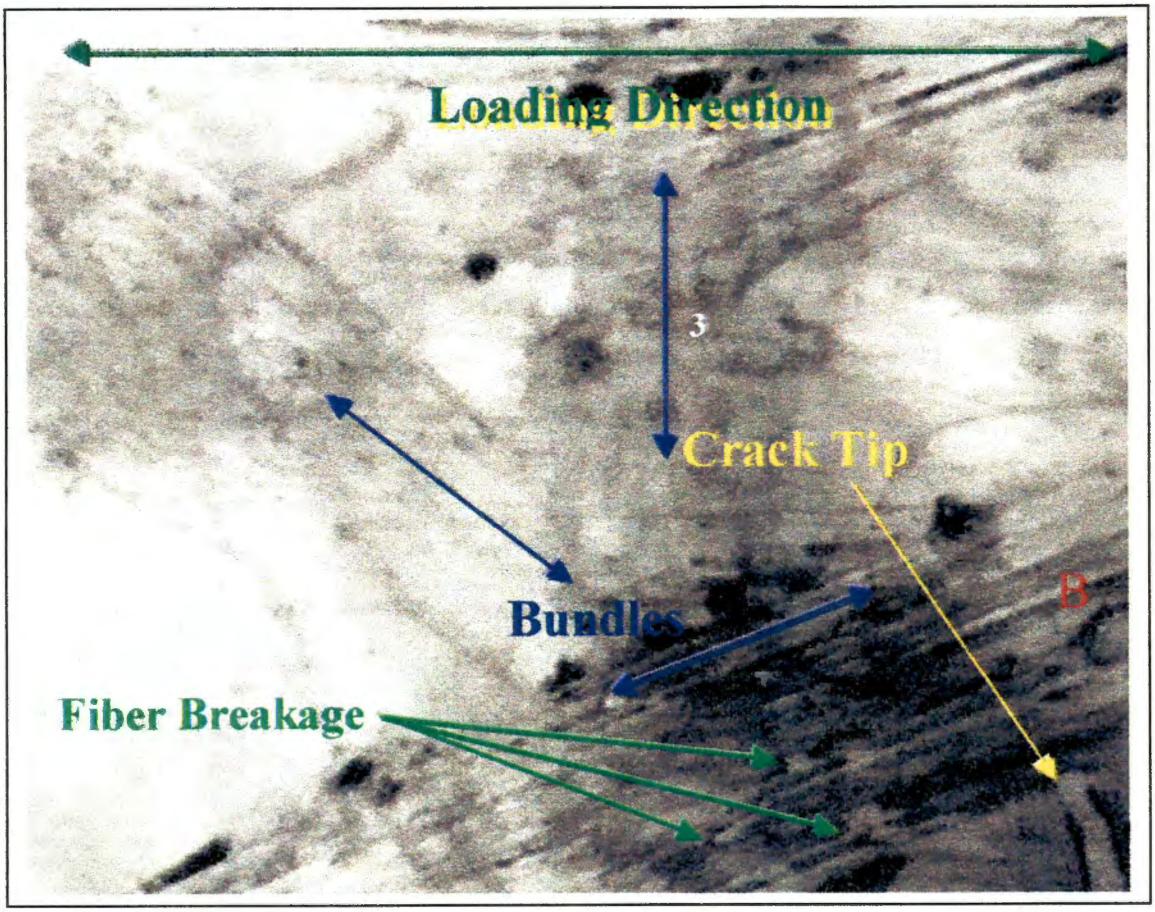

Figure 41. Continuation of crack growth and damage formation.

7.4 Failure Mechanism

The development of a failure mechanism was achieved by using the images obtained from SEM and real-time tensile loading. The SEM images revealed a surface of dominant crack propagation. These images as shown in Figure 35 to Figure 38 indicates that the path of the propagating crack was along the fiber/matrix interface, and changed direction due to fiber orientation, void content and size. Also shown in these images is that fiber pullout occurred. A more detailed discussion of the failure mechanism will be presented in the discussion section.

7.5 Void Volume

The following results are for the evaluation of percent void volume for this CSMC. The method as developed in our laboratory provides a relative measure of the percentage of volume occupied by voids. The major and minor axes of voids present in thinned gauge length sections of tensile specimens was measured using the NIH® software package. The results are shown in Appendix B. The values determined for the major and minor axis were applied to Equation 17, which is the volume of an ellipsoid. The average void size was obtained by collecting several images from different areas on a single specimen. This was performed on seven (7) different thinned sections. The average void volume calculated was multiplied by the number of voids present, which results in the volume of voids in a thinned section. The void volume for the sample was then obtained by multiplying the volume of voids in a thinned section by the number of thinned sections necessary to achieve the sample thickness of 0.125 inches, which was 3.84

thinned sections. A sample calculation for this method is shown in Appendix B. The resulting percent void volume, V_v, for the sample was determined to be approximately 12%. This of course is a relative measure of percent void volume, however, in unpublished work by the ACC the void volume measured was 10.4%.

7.6 Mathematics of Fracture Toughness

The desire to use predictive tools to evaluate material properties is the motivation in the following sections. The focus is to predict the stress and fracture toughness, K_I, for a continuous swirl mat composite, CSMC, using results from tensile tests of the individual components and imaging data of void content, size, and orientation. The correlation of tensile test results to the fracture parameter provides a way for designers and engineers to make better material choices, based on the stress-strain response and failure criterion. As mentioned earlier, this CSMC, produced from the structural reaction injection molding, SRIM, process resulted in a significant number of voids that formed in the matrix and along fiber and fiber bundle axis. The condition of the mat prior to processing also contributed to the void formation. The presence of voids and mat defects are incorporated into the mathematical calculation of K_{IC} via the stress prediction. The overall K_{IC} value is formulated by utilizing K-solutions. It is the objective of this evaluation to provide a possible approach in predicting K_{IC} for this CSMC.

7.6.1 Evaluation of Applied Stress

In order to predict the breaking stress of the composite, the "Rule of Mixtures", as shown in Equation 3, was applied. This rule takes into account the contribution the matrix and fiber, as a function of their volume fraction, has on the overall property to be evaluated. Before getting involved in the mathematics of the desired prediction let us look at the properties of the individual components.

The matrix material is an isocyanurate based polyurethane matrix, which has an ultimate tensile strength, UTS, of 70.3 MPa, tensile modulus of 2.1GPa, and a tensile elongation of 6.0%. The reinforcement in this composite is a continuous strand E-glass mat. These continuous strands consist of approximately 300 monofilaments per bundle, and are 17μm in diameter. The E-glass fibers have an average ultimate tensile strength of 1.7 GPa, a tensile modulus of 69 GPa, and an elongation of 0.2%. The importance of this information will be seen later in the mathematical development. However, knowing that both matrix and reinforcement undergo brittle failure is a key observation. One other initial observation is that the matrix has a larger elongation, but a lower ultimate tensile strength and modulus.

In general, there are two possible conditions for strain. One condition occurs when the strain at break for the fiber is greater than the strain of break for the matrix, and secondly, when the strain of break for the matrix is greater than the strain of break for the fiber. In this continuous swirl mat composite the latter is true. Within this case, there are two antagonists pathways for the onset of failure, low and high volume fiber content. Let us look at these two conditions, first, the low fiber volume content, that is $V_f \ll 1$, and its elongation being less than that of the matrix, it is possible that the fiber fails first. This results in an insufficient transfer of load from the matrix to the fiber, resulting in the matrix having to carry a greater load. Therefore, breakage will not occur unless the matrix failure load is exceeded. It can then be seen mathematically, as shown in Equation 18, that the breaking stress of the composite, σ_{BC}, is governed by the matrix term due to insufficient transfer of the load from the matrix to the fiber. As fibers fail there is a reduction in cross-section due to crack formation as well as a reduction in load carrying capacity of the matrix proportional to the fiber volume fraction. An understanding of the failure strength for this condition is imperative to the mathematical evaluation of this condition, that is; the matrix will control the strength of the composite.

$$\boxed{\sigma_{Bc} = \sigma_{Bm}(1 - V_f)}$$ **Equation 18**

σ_{Bc} = Breaking stress of the composite
σ_{Bm} = Breaking stress of the matrix
V_f= Fiber volume fraction

Secondly, at a large fiber volume fraction the transfer of load is more efficient than for low fiber volume fraction. This load transfer occurs at a much greater extent, due to increased interaction via the interface or traction forces between fibers and matrix. This more efficient transfer causes the matrix to fail when the fiber fails. The higher fiber volume forces the consideration of the fiber term in the evaluation for the overall changes in stress and is shown mathematically in Equation 19, where' σ_m^* ' is a point on the stress-strain curve of the matrix for which the failure strain of the fiber occurred.

$$\boxed{\sigma_{Bc} = \sigma_{Bf} Vf + \sigma_m^*(1 - Vf)}$$ **Equation 19**

When Equation 18 and Equation 19 are set equal to each other there is a point of significance at a specific fiber volume fraction. This point will be referred to as a "cross over point". The volume fraction, V'_f, at the cross over point is associated with the onset of matrix cracking and shown mathematically in Equation 20.

$$V_f' = \frac{\left(\sigma_{B_m} - \sigma_m^*\right)}{\left(\sigma_{B_f} + \sigma_{B_m} - \sigma_m^*\right)}$$ **Equation 20**

Equation 18, Equation 19 and Equation 20 come from work by Klaus.[64] However, in order to achieve an accurate contribution of the matrix to the overall stress component using the "Rule of Mixtures", it would have to be modified to account for the presence of voids. The modified "Rule of Mixtures" is shown in Equation 21. The consideration of voids should result in a further reduction in the matrix contribution to stress (due to the presence of voids). The use of image analysis enabled the evaluation of the void volume, V_v, which was evaluated using a procedure developed in our laboratory, which was discussed in detail in section 7.5. This technique resulted in a 12% void volume content.

$$\sigma_{BC} = \sigma_{Bf} V_f + \sigma_m\left(\left(1 - V_v\right) - V_f\right)$$ **Equation 21**

7.7 Mathematical Approach to Fracture Toughness, K_{IC}

In order to obtain a possible predictive tool for K_{IC} for this composite system the use of K-solutions for in-line and parallel crack configurations were considered due to the arrangement of voids in the CSMC. The following equations describe the K-solutions for in-line and parallel cracks. The use of these two configurations represents the arrangement of voids in the composite. It is the combination of these two equations that enabled the prediction of the fracture parameter.

$$K_I = \sigma\sqrt{\pi a}F(s) \qquad \text{Parallel cracks}$$

$$K_I = \sigma\sqrt{\pi a}\sqrt{\frac{W}{\pi a}\tan\frac{\pi a}{W}} \qquad \text{In-line cracks}$$

Where:

$$F(s) = \sqrt{\frac{1-s}{\pi s}}$$

$$s = \frac{a}{a+h}$$

2a = average void length
h = average distance between voids
W = the mean distance between voids

The evaluation of K_{IC} was performed using the combined expression shown in Equation 22,

$$\boxed{K_{IC} = \sigma_{BC}\sqrt{WTAN\left(\frac{\pi a}{W}\right)}F(s)D_\theta^W} \qquad \textbf{Equation 22}$$

which is the simplified result of the combined K-solution for in-line and parallel cracks with the orientation factor, D_θ^W, which takes into account the effect void orientation has on the applied stress, and is defined as '$\cos^2(\theta)$' where 'θ' is assumed to be approximately 45° for a random system due to the random nature of the glass mat and the formation of voids along the fiber bundle axis. The evaluation Mixtures" while 'a' and 'W' were evaluated from light microscopy and NIH® software to measure center-to-center distances of adjacent voids, and the major and minor axis of voids. The calculated values using Equation 22 for K_{IC} as a function of volume fraction of fiber is given in Figure 42. The predicted response shows a steady increase with fiber volume fraction and predicts for a 40% by volume of glass fiber and a void content of 12% a K_{IC} value of 11.4 $Pa\sqrt{m}$. The effect void orientations, fiber contents and void volumes have on the prediction is shown in Figure 43, Figure 44 and Figure 45 and a composite of each in Figure 46. As shown in Figure 46 there is an increase in K_{IC} with a decrease in void orientation relative to the applied load. It is also shown that an increase in fiber fraction results in an increase in K_{IC}, while void volume has the effect of lowering K_{IC} shown in more detail in Figure 47 to Figure 50.

7.8 Experimental Results of Fracture Toughness

The K_{IC} value was calculated using the ASTM standard E1820-96. The load vs. displacement curves used in the calculation of K_{IC} are shown in Appendix A, however, Figure 51 is a representative curve for the experimental results of the K_{IC} tests performed. As shown in the ASTM E1820-96, a 95% secant line is drawn to determine the value of P_Q and P_{max}. From Figure 51, P_Q and P_{max} were determined to be 169lbs and 175lbs,

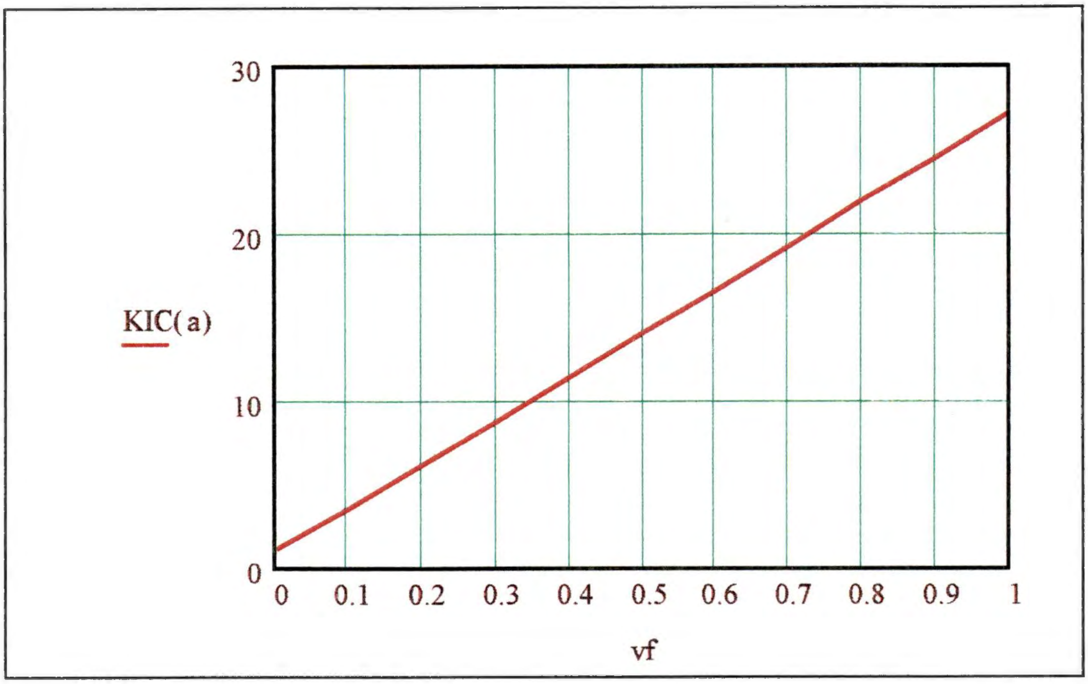

Figure 42. K_{IC} predicted as a function of fiber volume fraction.

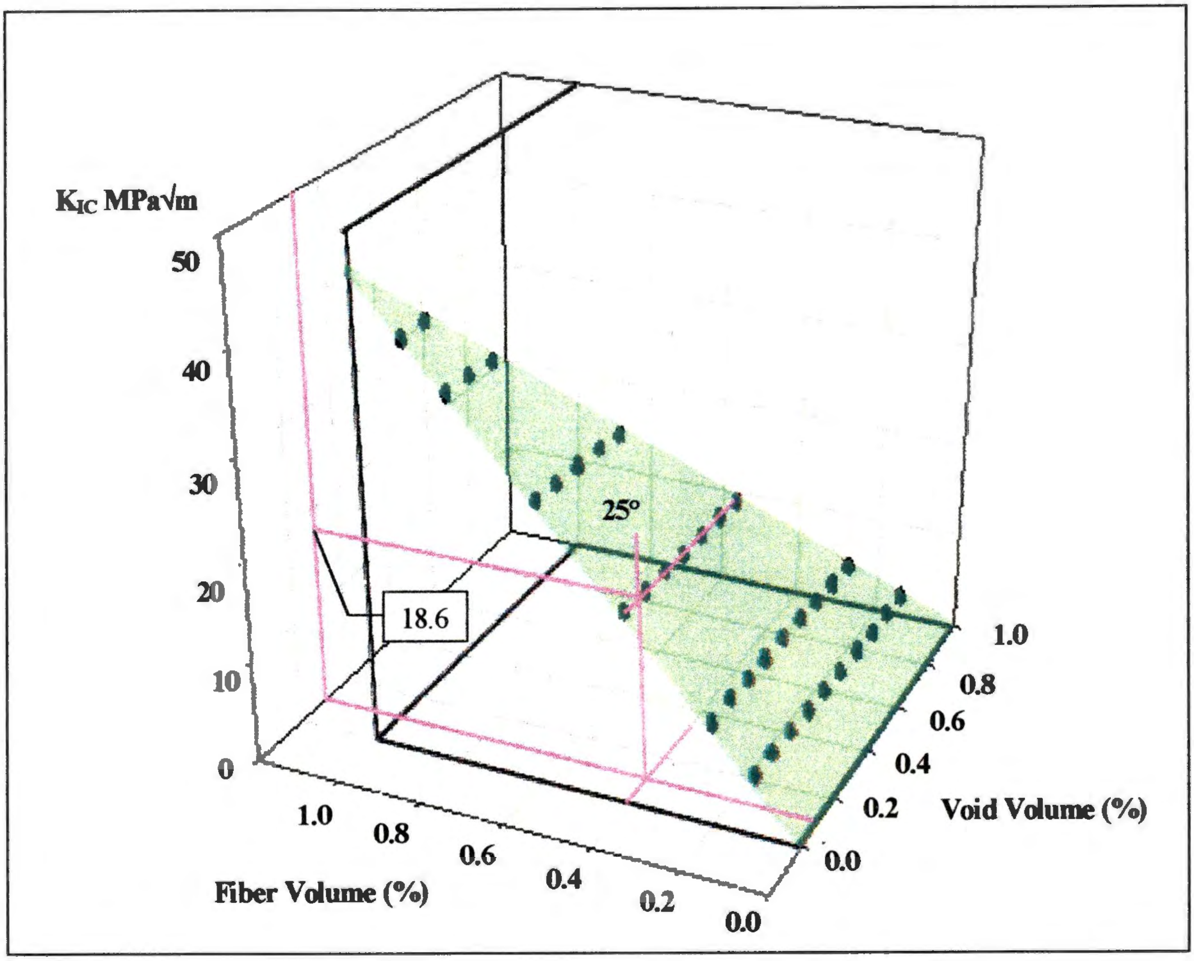

Figure 43. Three dimensional plot with a void orientation angle of 25°.

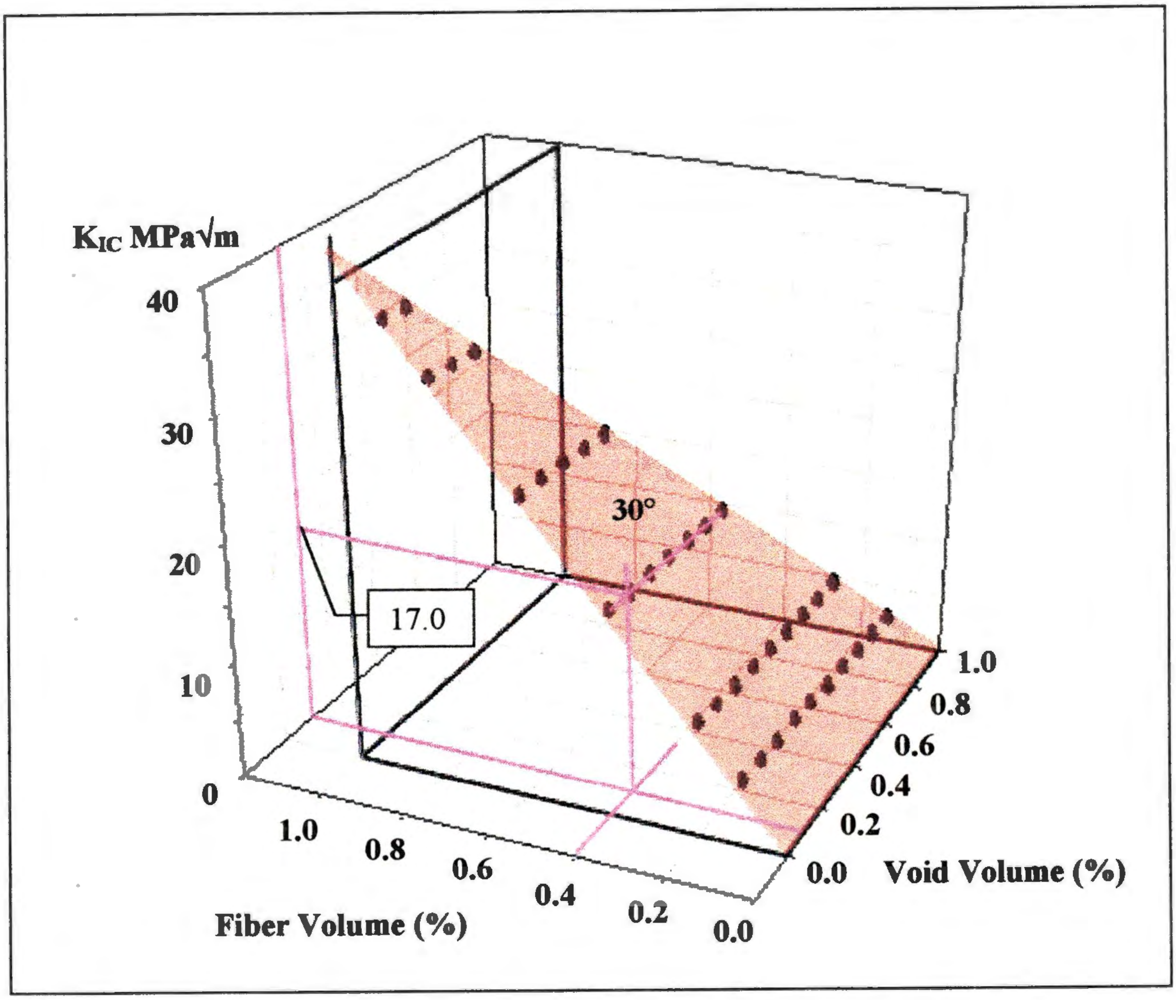

Figure 44. Three dimensional plot with a void orientation angle of 30°.

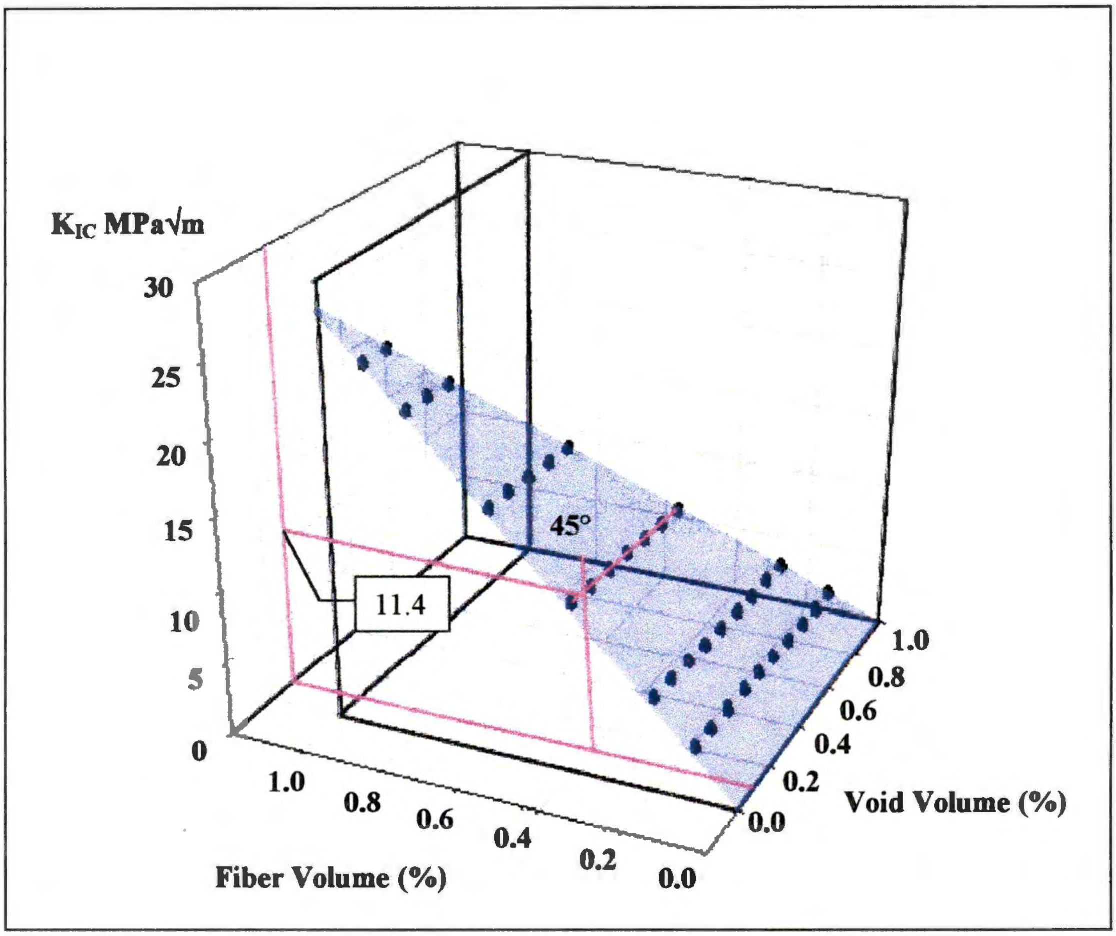

Figure 45. Three dimensional plot with a void orientation angle of 45°.

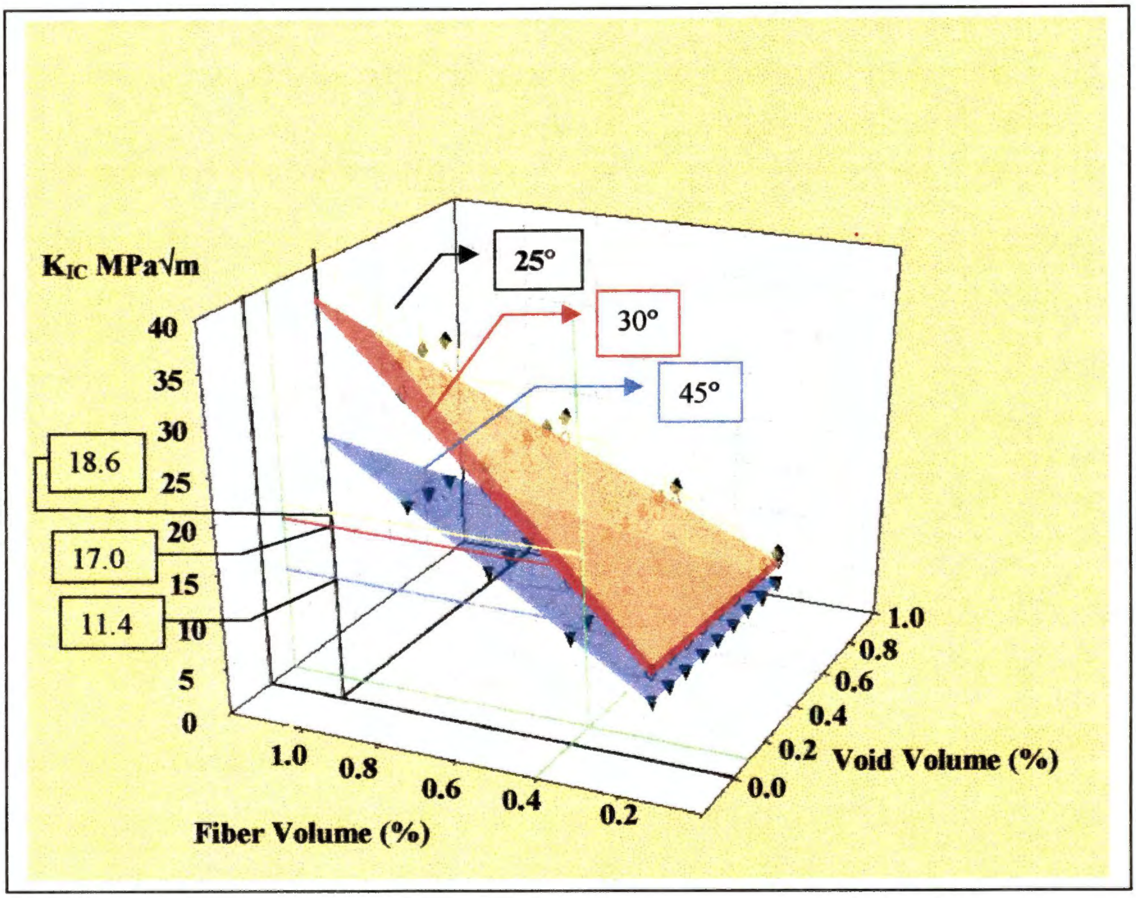

Figure 46. Composite plot of 25°, 30° and 45° void orientations.

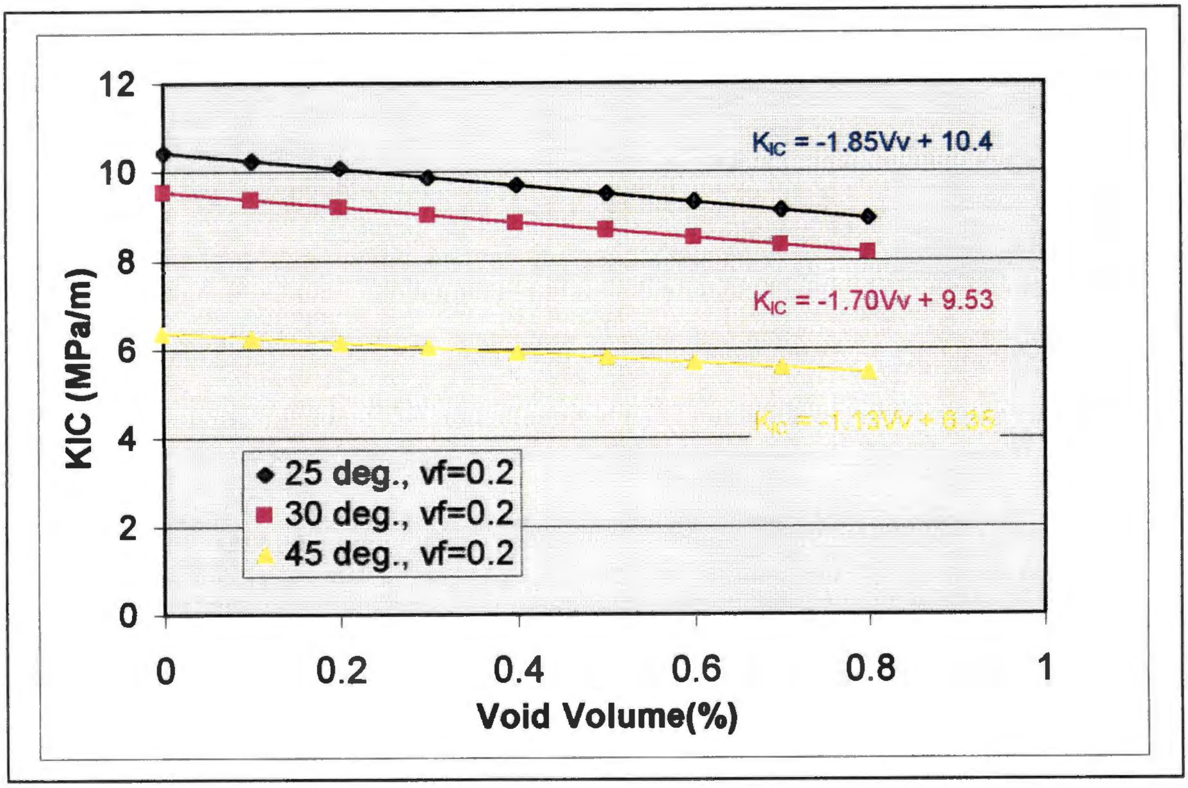

Figure 47. The effect of void volume on K_{IC} at a fiber fraction of 0.2.

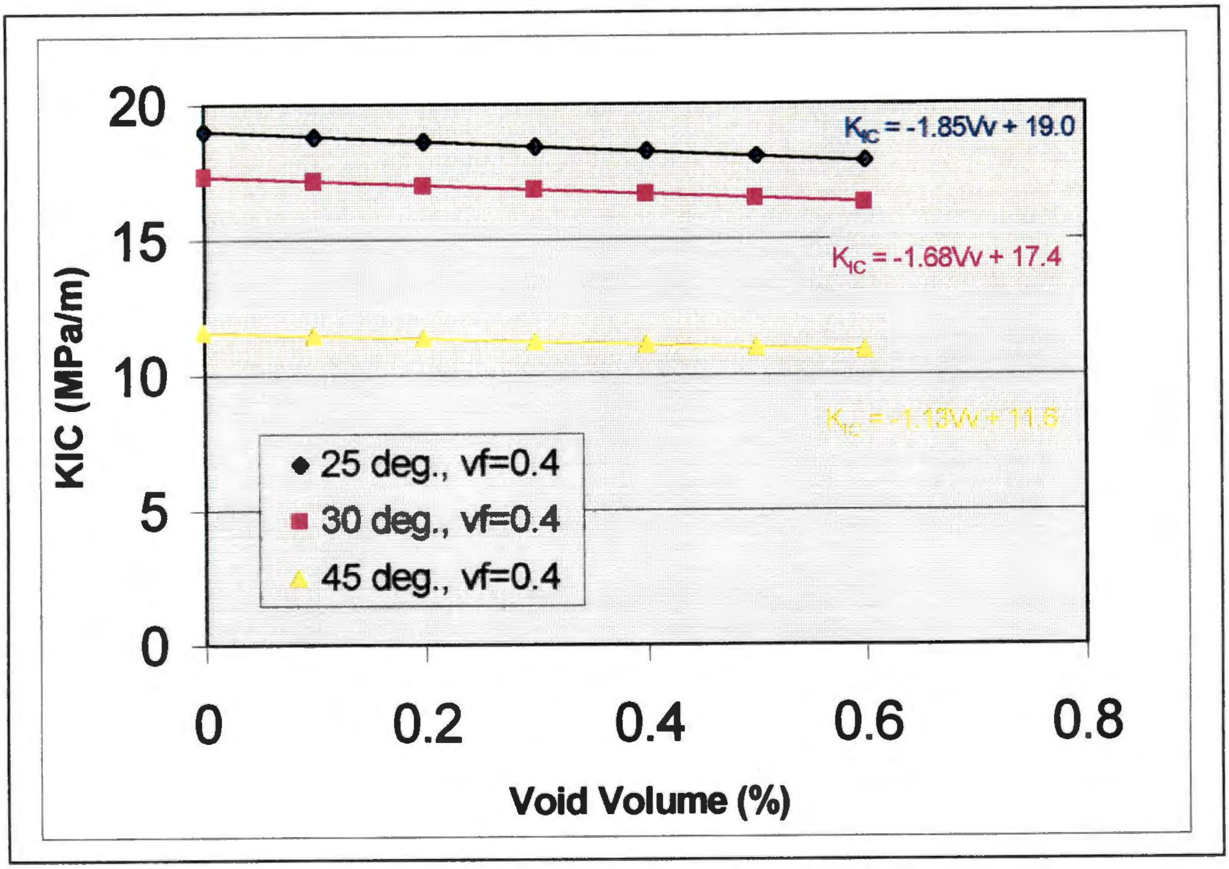

Figure 48. The effect of void volume on K_{IC} at a fiber fraction of 0.4.

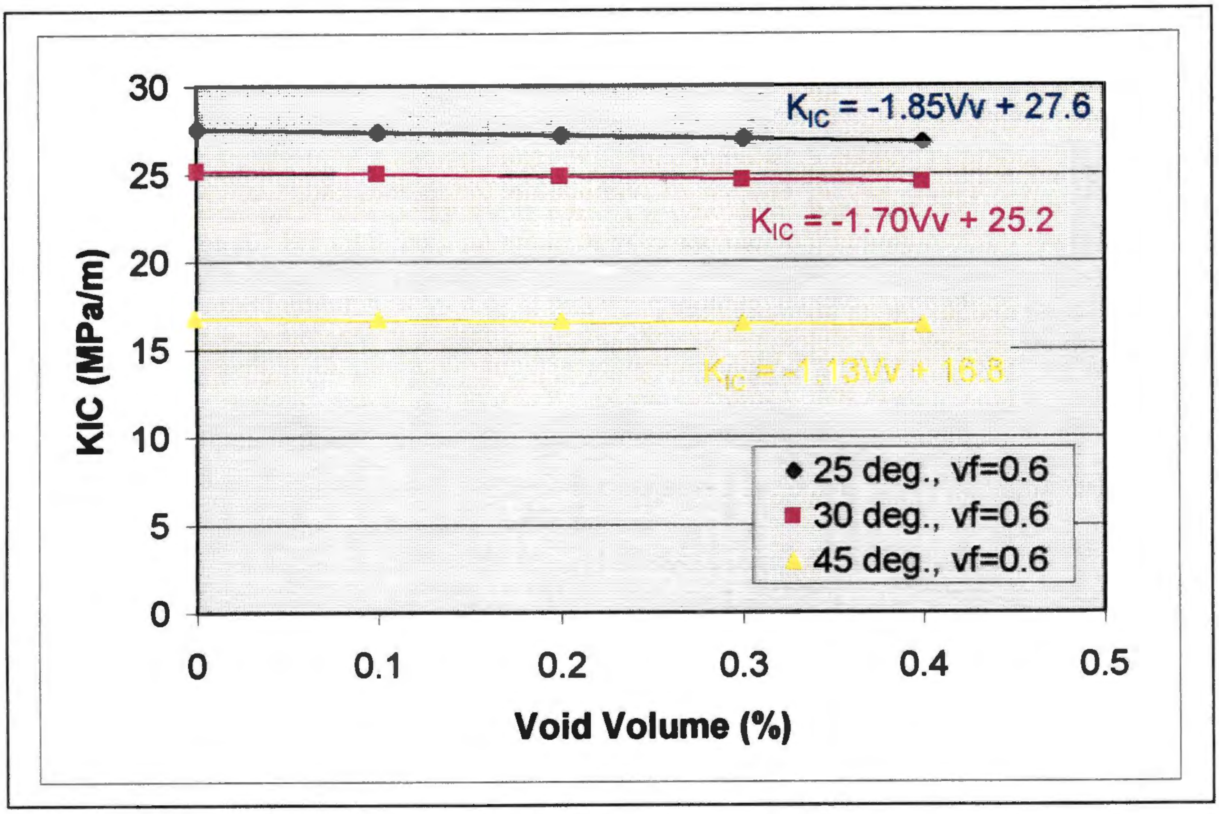

Figure 49. The effect of void volume on K_{IC} at a fiber fraction of 0.6.

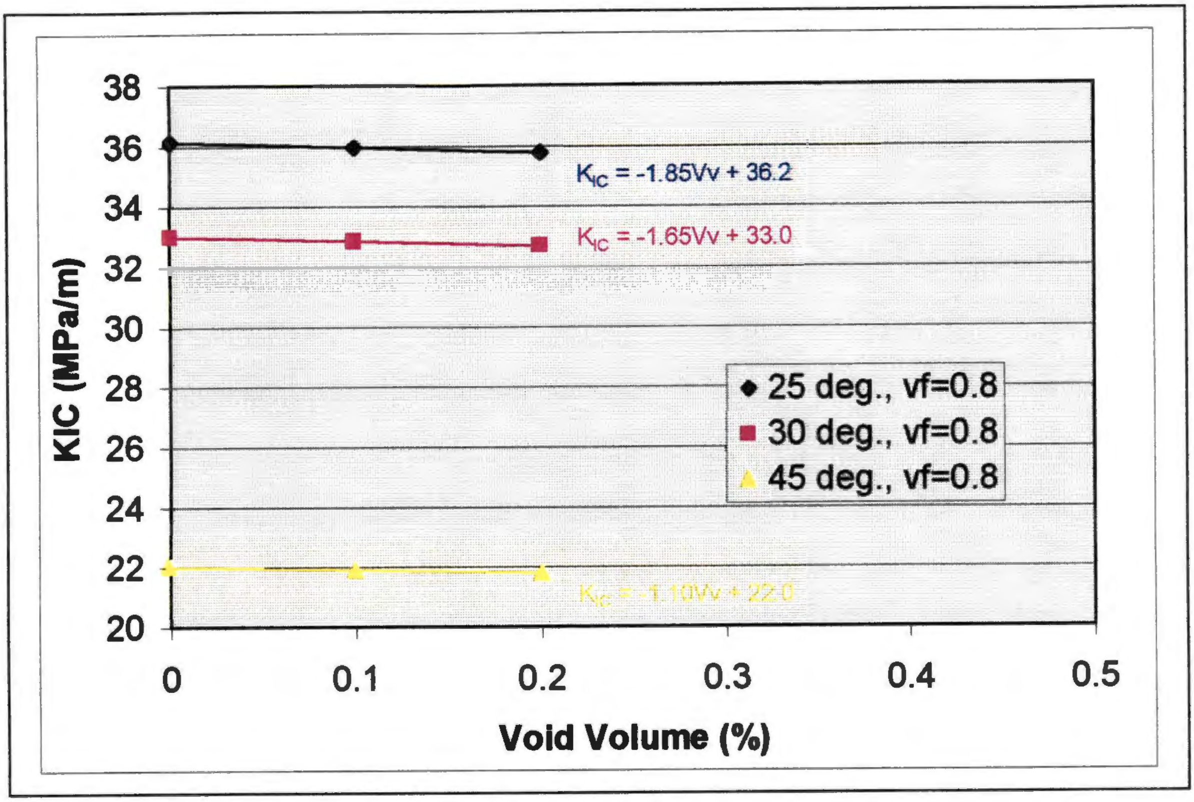

Figure 50. The effect of void volume on K_{IC} at a fiber fraction of 0.8.

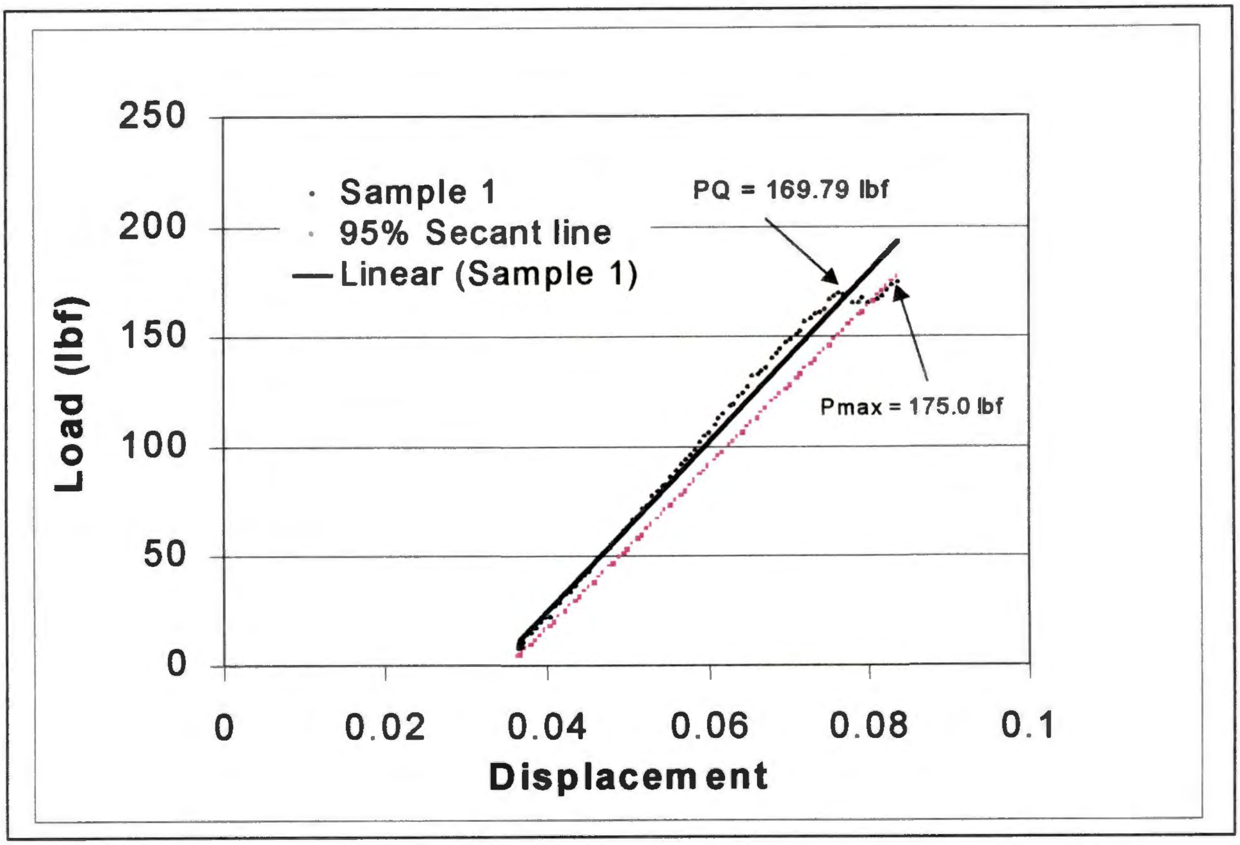

Figure 51. A representative Load vs. Displacement curve for K_{IC} evaluation.

respectively. The K_{IC} determined experimentally was 17.1 (±1.45) MPa$\sqrt{m}$. This value is in the range of predicted K_{IC} values at a 12% void volume and 40% fiber content for void orientations of 25°, 30°, and 45°, which are 11.4 MPa$\sqrt{m}$, 17.0 MPa$\sqrt{m}$, and 18.6 MPa$\sqrt{m}$, respectively.

VIII. DISCUSSION

8.1 Mechanical Response and Damage Assessment and Progression

The mechanical tests performed, tensile and creep, provided more than just the overall mechanical response of the CSMC under these loading conditions. It also provided a way to introduce damage at different percentages of the ultimate tensile strength (UTS). The reason for applying different percentages of the UTS was to control the amount of damage accrued by samples. This idea proved to be useful in the evaluation of damage progression and assessment as will be discussed. The property of great interest was the modulus. The modulus was shown in literature to be a property that changed consistently with accrued damage.[65] The work conducted here looked at the reduction of modulus as a function of UTS percentage. The modulus reduction showed an onset at approximately 30% of the UTS. The reduction in modulus is due to the formation of damage, which disrupts the continuity between the matrix and reinforcement. The formation of defects such as cracks, debonding, and fiber breakage form areas within the cross-section that no longer have the ability to contribute to the bearing of any applied load because the newly formed surface are no longer able to interact, therefore, no transfer of load.

The onset of modulus reduction correlated with the observed change in the ultrasonic amplitude map's average grayscale value, AGV. As shown in Figure 31 p. 83 in the result section the calculation of the AGV produced a value between 0, completely black, and 255, completely white. Samples scanned before loading and after each sequential loading showed a decrease in the AGV from ~171 to ~115 with an increase in the percent loading from 0% to 80%, respectively. The onset of the decrease in AGV is shown to occur between 20%UTS and 40%UTS, which correlates well with the onset in modulus reduction, which occurred around 30% UTS. The decrease in AGV is due to the formation of damaged regions over the entire cross-section, which are large enough to attenuate the ultrasonic signal resulting in a darkening of that area. Scattering of the ultrasonic energy occurs due to the formation of defects such as debonding, fiber breakage and matrix cracking, which occurs as a function of percent loading.

8.2 Mechanistic Approach to CSMC's and Damage

The mechanism is essentially a microanalysis of how different regions along the fiber axis should respond to the applied load in a matrix that has some defects. This is based on experimental observations and an understanding of the response of oriented fibers relative to an applied load. First, the research conducted by Tsai[66] on the development of a Strength Theory for a single laminate with uniaxially oriented continuous fibers should be mentioned in order to discuss the effect of fiber orientation on strength. The theory implies a dependence of the mechanical strength and stiffness as a function of fiber orientation relative to the loading direction. To better understand the idea, the load capability of the fiber along its principle axis has its greatest mechanical strength due simply to the strength of the fiber, see Figure 52 p.111. However, at 90° to that principle axis the fiber and matrix have to work together via the interface. This imperfect interaction between these three components (fiber, matrix and interface) that reduces the properties in this direction. This imperfection is manifested as the inability of the interface to effectively transfer the load from the matrix to the fiber. In light of Tsai's strength theory, the importance of fiber orientation must be taken into consideration. For this CSMC system the reinforcement is a randomly swirled glass mat consisting of continuous fiber bundles. The difference between Tsai's contribution and the present work, is the fact that orientation remains a major consideration. The orientation of the mat, however, is viewed in this mechanism as segments of a continuous bundle being oriented in a given direction relative to the load.

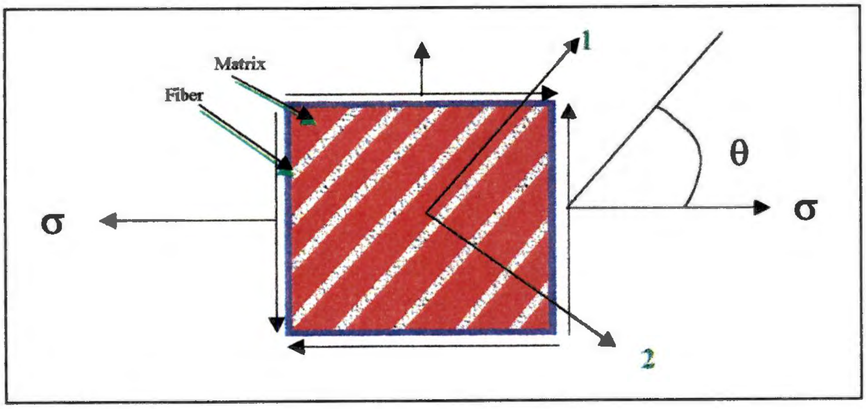

Figure 52. Fiber orientation relative to applied load.

The randomly swirled reinforcement presents a case where segments of fibers are oriented at different angles to the applied load. A schematic illustration of the swirl mat is presented in Figure 53. A comparison of the reinforcement in Figure 53a and Figure 53b, suggests that several segments of a single fiber can be oriented in any of the suggested orientations as shown in Figure 53. Due to the variations in fiber orientation with respect to the loading direction, it can be expected from the familiar case of uniaxially oriented composites, and their properties relative to fiber orientation, that those

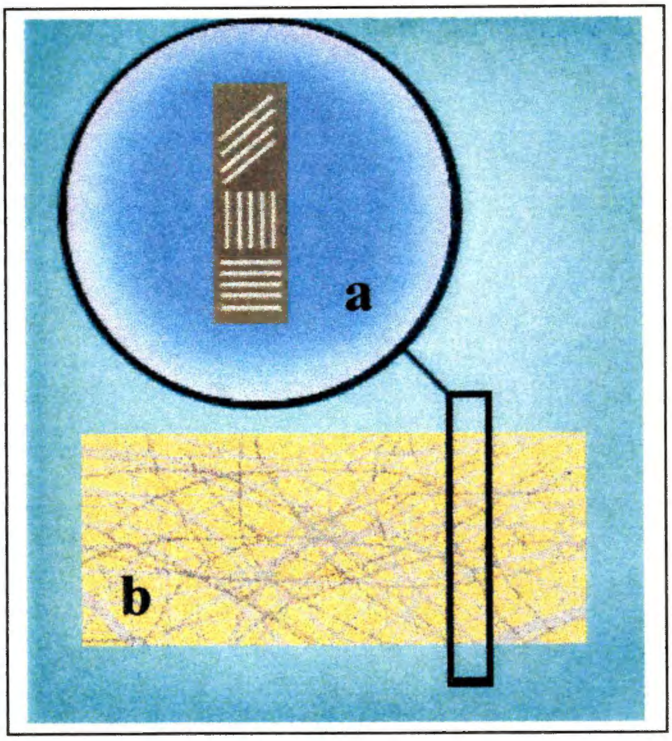

Figure 53. Swirl mat orientation simplified.

fibers aligned in the direction of loading can carry the largest load. These same fibers would likely undergo fiber pullout under tensile and creep loads. The fibers normal to the loading direction are in their least load carrying orientation and would contribute to fiber/matrix debonding; while the fibers at some angle to the load can undergo tensile and shear failure producing fiber/matrix debonding and fiber pull-out. The mechanism suggested for the initiation of failure under tensile and creep loading occurs in one of four ways. Cracks are introduced in the matrix due to voids or impurities, fiber/matrix debonding, fiber/fiber debonding, or fiber failure at low loads. If the initial crack forms in the matrix, it will propagate along a path of least resistance, this is often the fiber/matrix interface. As proposed in the mechanism and shown in the SEM images Figure 35 p. 84 through Figure 38 p. 87 the crack follows the interface until complete failure. The simplification of the fiber's orientation relative to loading suggests that there should be evidence of a path of crack propagation along the weak axes. The observations with SEM, see Figure 38 p. 92, showed signs of cracking along those fibers oriented perpendicular and then along those at some angle to the applied load resulting ultimately in the failure of fibers parallel to the loading direction. As shown in SEM images in Figure 36 p. 90 there is a relatively clear picture of the direction of crack propagation that follows the above stated relationship to failure and fiber orientation.

The real-time studies of crack propagation also showed that cracks once formed follow fiber matrix interfaces (see Figure 55 p.121 and Figure 56 p.121), which ultimately results in complete failure with the fracture surfaces being perpendicular to the loading direction. It can also be said that due to the relationship between load and fiber orientation in the CSMC the damage should also be distributed. This supported by the C-scans shown in Figure 29 by the increase in attenuation over the entire sample, which is due to the formation of damage. Damage is assessed from C-scan by evaluating the increase or decrease in the amplitude maps. An increase in attenuation is directly associated with the formation of cracks, debonding, fiber breakage, or pullout. It is the scattering of energy due to the interaction of the ultrasonic signal with the formed defects that causes the increase in attenuation. Therefore, the attenuation maps presented as a function of UTS shows a definite change in attenuation over the entire cross-section of the specimen and it is this observation that clearly shows that damage events occur over the entire specimen. This analysis does show that damage occurred. However, it does not provide any information as to the damage events such as matrix cracking, fiber matrix debonding, etc.

8.2.1 Failure Mechanism

Damage progression in the CSMC was evaluated using real-time video analysis of tensile loading with subsequent C-scans. The video collected during loading, as shown in Figure 39 to Figure 41, contain the damage features suggested earlier, that is, matrix cracking, fiber breakage, fiber pullout, debonding and coalescence of voids. In addition, they show the effect voids have on crack growth and the effect of fiber orientation on the direction of crack growth. All of these features affected the progression of damage in the CSMC.

The initiation of failure was the most difficult characteristic to identify. However, once a dominant crack formed it would control the failure process. The CSMC failed in a brittle fashion, yet under controlled loading cracks could be grown for approximately 3mm before complete failure occurred. It was within the 3mm window that crack formation and growth was followed. Some cracks would initiate near the edge of a specimen either at a surface defect or at a fiber bundle. The bundle segment most susceptible to initiate damage was either perpendicular or at some angle to loading. The growth of the formed crack followed paths described for other fiber composite systems.[67,68] That is, the crack would propagate along the fiber/matrix or fiber/fiber interface that was oriented relatively perpendicular to loading. The crack would move away from the interface, if a void of adequate size were at a reasonable distance from the tip of the growing crack, the crack would change direction toward the void. This suggests that the voids act as stress risers, which contribute to a path of least resistance for the crack, therefore, the crack would propagate through the void. The orientation of the fibers around the dominant crack as well as the density of voids in that area controls the mechanism.

The assessment of damage once observable can be reconstructed. As with any type of failure, there is a point at which the damage initiates, and propagates to complete failure. The formulation of a failure mechanism as shown in Figure 54 indicates that fibers perpendicular to loading are most vulnerable to failure. Fibers that are at some

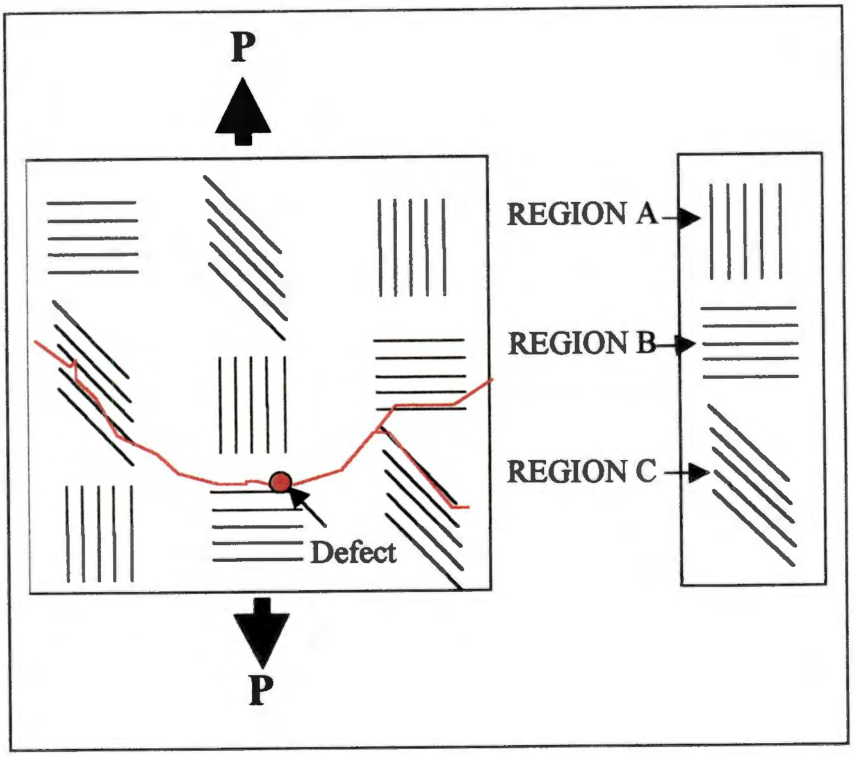

Figure 54. Failure mechanism for CSMC.

angle to the applied load follows while fibers parallel to the loading direction fail last. Initiation of the failure process is presumed to occur at a material defect or fiber orientation effect. Propagation, however, follows the fiber/matrix interface unless a void of reasonable size lures the growing crack towards another bundle. These results are verified from SEM images.

8.2.2 The Failure Mechanism and SEM

The most notable feature in the SEM images is how well the top surface follows the proposed mechanism shown in Figure 54. Region A represents the fibers oriented in the loading direction. Region B is associated with fibers that are aligned normal to the loading axis. Region C is for those fibers that are at some angle, θ, to the load. These regions are a simplified characterization of a localized area of the CSMC to demonstrate a possible path for crack propagation, which is supported by SEM images shown in Figure 35 to Figure 38. Figure 37 indicates the presence of a void next to a fiber bundle perpendicular to the loading direction. Propagation of this crack along the fiber matrix interface is obvious due to the presence of the remaining fibers. Figure 38 also shows fibers perpendicular to loading direction, however, it is also indicated here that the fiber interface at an angle to the loading direction are susceptible to crack growth along its interface. Figure 35 and Figure 36 show a larger area of fiber damage and matrix cracking, again fibers at some angle to the loading are exposed, which indicates the crack propagated along that fiber matrix interface. As shown in Figure 35, the junction where two fiber bundles 'A' and 'B' cross and another fiber bundle 'C' is practically parallel to the loading direction indicates that the fiber bundle parallel to the loading direction was not as susceptible to crack propagation. The crack does travel along its interface, but only after a significant amount damage occurred around it. Notice that the fiber bundle 'C' is practically severed from the matrix. Taking into consideration the SEM images and looking at the real-time images Figure 39, Figure 40 and Figure 41, which shows the formation of a crack and eventual opening, which is shown in Figure 40. The formed crack in Figure 40 is along a fiber bundle relatively perpendicular to loading direction. A fiber bundle near the landmark 'B' shown in Figure 40 encounters the growing crack causing a momentary delay in crack progression. Figure 41 shows the damage accrued in front of the growing crack, which is at the junction of three fiber bundles. This particular sample failed catastrophically along the fiber bundle, 3, perpendicular to the applied load.

8.2.3 Tensile and Creep

Damage Progression during Tensile and Creep

The progression of damage in the CSMC in Tension and Creep was evaluated using real-time video analysis. The video collected during loading provided information concerning the progression of damage in these composites. Before getting into specifics for each loading type a quick explanation into the general or common character of progression is presented. First, initiation will be discussed followed by progression. Propagation is so rapid that the concept of termination is essentially the end of propagation. The formulation of a mechanism was possible by putting together all of the imaging information available from failed specimens as well as real-time image analysis.

Initiation

The initiation of failure in the continuous swirl mat composite has been observed in both the matrix and interface. Initiation is the most difficult characteristic to observe due to the vast number of locations at which failure can begin. The failure of any composite material having a fiber reinforcement is dependent in part on the direction that load is being applied relative to the orientation of the reinforcement as well as the integrity of the interface between the matrix and the fibers. The CSMC follows the same failure criterion as uniaxially oriented composites, that is, the fiber segments oriented in the direction of load are in their greatest load carrying position while those segments perpendicular to load are in their weakest load bearing position.

The initiation of failure occurs in one of four ways. A series of possible initiation locations are mentioned because each has been observed. The crack is introduced by voids, by fiber/matrix debonding, fiber/fiber debonding, surface pits, or incomplete wetting of fiber bundles at the surface or specimen edge (edge effects).

Propagation

The propagation of a formed crack in the CSMC is in competition with other formed cracks. Because there are several locations where cracks initiate, there will result a primary dominant crack. It is thought that the dominant crack is one that has found a path of least resistance. The path of least resistance has few dense junctions of fiber bundles and a dense population of voids at or near the bundle junctions. However, once the dominant crack is formed it can channel its way around and through bundles and void spaces. Propagation in the majority of cases remains at the fiber matrix interface unless the crack moves towards voids near the path of propagation. The void space tends to lure the crack into the matrix and then back to the fiber/matrix interface, which could be along a different bundle, see Figure 55 p.121 and Figure 56 p.122. These images were captured using real-time video recording and by adjusting the load level to avoid catastrophic failure. These two images are of the same area; however, Figure 55 shows the crack in a closed position while Figure 56 shows the crack in an opened position. As indicated on each image fiber bundles, matrix and voids can be identified. For the crack in an open position the yellow line shows its path. As it is shown the path is along the fiber/matrix interface and changes directions in the presence of voids only to return to the fiber/matrix interface.

The glass mat for simplicity sake is random. However, it should not be overlooked that the propagation of the crack is along a preferred orientation direction controlled by the local orientation of the swirled mat and is most likely the reason for the anisotropic mechanical properties observed for 0 and 90 specimens. The dominant crack once formed will propagate along a zigzag path changing direction at the bundle junction or due to voids as mentioned earlier. This zigzag path is the path of least resistance for the dominant crack and occurs along interfaces that are relatively perpendicular to the applied load. The most interesting aspect of propagation is the evidence observed of fiber breakage and pull-out after a significant amount of interfacial failure has occurred in that area. The propagation of the crack perpendicular to loading is the most detrimental due to the fiber being in its weakest load bearing position. Often times prior

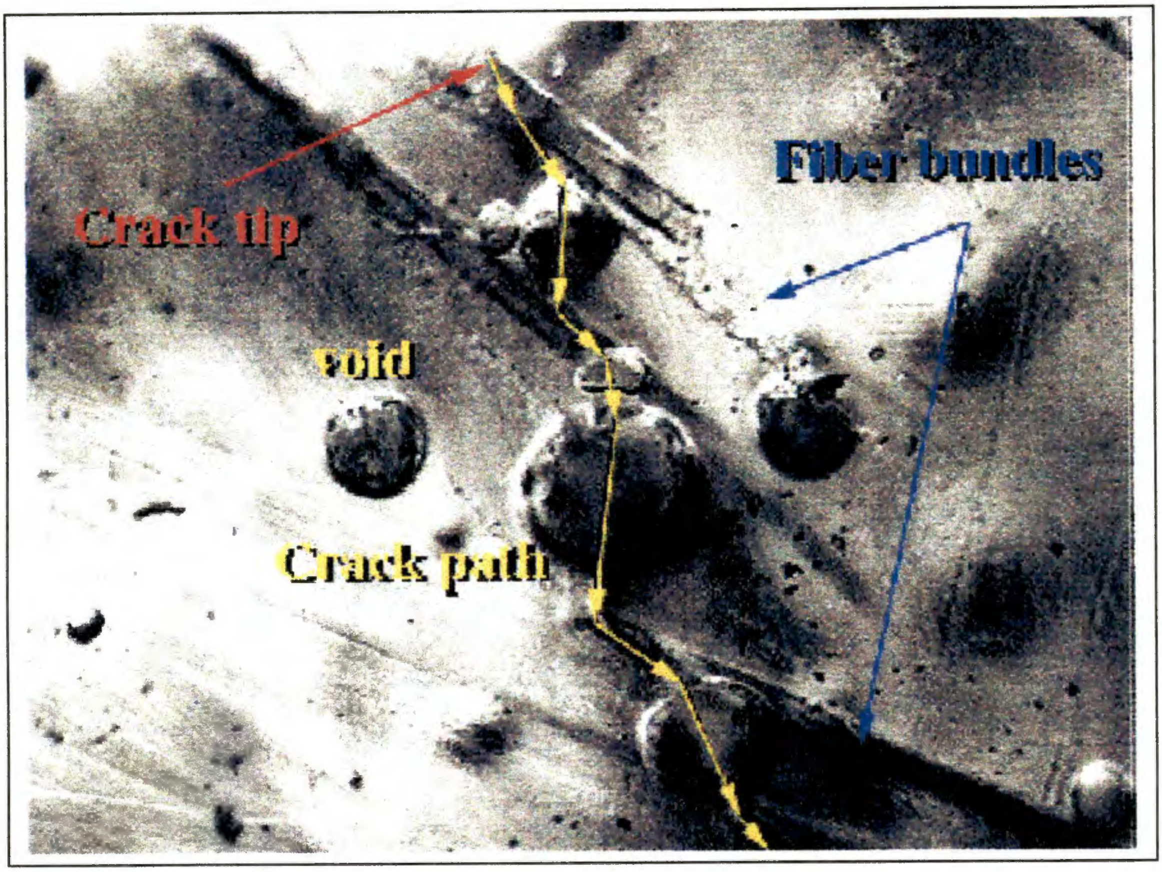

Figure 55. Crack Propagation through voids and along bundle.

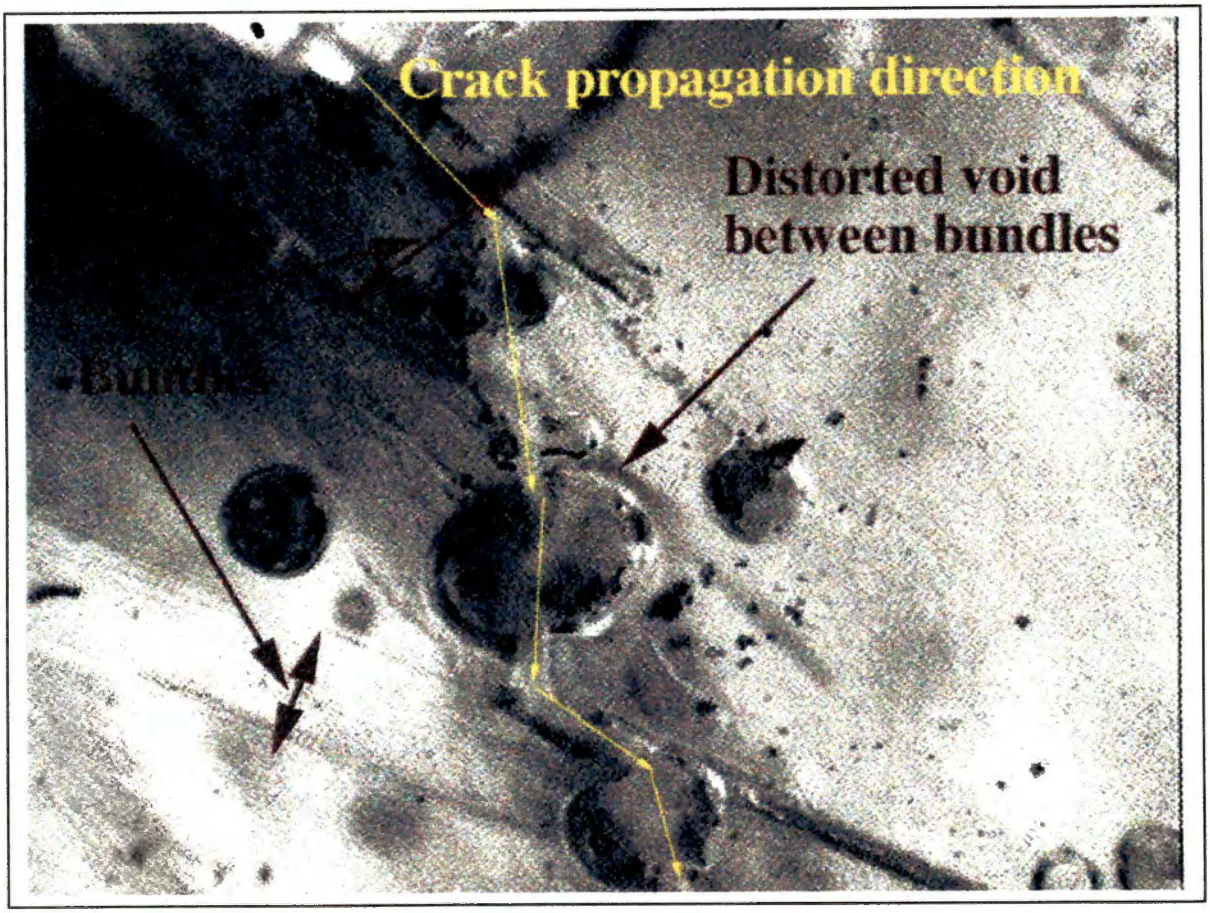

Figure 56. The opened crack through voids and along bundle.

to failure during static loading a crackling sound is heard. This sound appears to come from a mixture of fiber breakage, fiber/matrix and fiber/matrix/fiber tearing within a bundle. A fiber /matrix/fiber path is essentially a crack propagating such that the bundle is being split into two pieces. The finality of propagation is complete failure.

8.2.4 Fatigue

The crack initiation in fatigue is considered to be the same as in tensile and creep due to the applied load acting in a uniaxial direction on the same defects and fiber orientations. However, crack growth appears to be different. The difference lying in the frequency used to carry out the experiment. The tension-tension load level decreases the number of cycles needed to reach the critical point (see Figure 26). As shown in Figure 26, there is a decrease in the number of cycles to failure with an increase in load. The investigation of damage under fatigue was observed initially within the matrix. The early stages of damage occurred mainly around voids and surface defects as shown in Figure 27 p.77. This does not preclude some fiber/matrix debonding. However, it does suggest that debonding is either not as prominent as matrix cracking, or it is just difficult to detect outside of a real time investigation in the first few thousand cycles. The increase in the slope in Figure 26 is presumed to be caused by continuation of matrix cracking, fiber/matrix debonding, fiber breakage and fiber pullout, which is supported by Figure 27 in that it showed fiber/matrix debonding and matrix cracking at 3000 cycles and below. The only events not observed up to that point was fiber breakage and pullout. For there to be an increase in strain, fiber breakage and pullout would have to occur, which suggests that the critical point may be an exchange between matrix dominated properties to fiber dominated properties.

For example, the evaluation of CSMC specimen P36-0-43 was performed under fatigue loading with optical inspections taking place after 0, 100, 1000, 3000 cycles. The specimen was loaded to 48% of its UTS (1247psi) for each tension-tension cycling sequence and shown in Figure 26 curve 'B'. The purpose for making this observation was to provide further understanding to the damage events that occur in the percent strain vs. cycles plot. At 5 cycles no evidence of microcracking was observed, see Figure 27. However, at 100 cycles microcrack formation is observable in a distributed fashion in the matrix. That is, there are several locations in the specimen's gauge length where damage occurred. Damage was found to exist at fiber/fiber and fiber/matrix interfaces and was not severe. These interfaces were perpendicular to the loading direction. At 1000 cycles crack formation in the matrix extended to surface pits and internal voids while the interfaces were more noticeable. At 3000 cycles, which is slightly beyond the critical point, there was an increase in the length of formed microcracks as well as the continued formation of microcracks, cracking off of voids, and continued debonding. The distribution of this observation extended across the entire specimen in varying degrees of severity. The specimen failed at 5175 cycles.

The gradual increase in strain is due to the formation of cracks that formed mainly in the matrix. The increase in the percent strain vs. cycles beyond the critical point is probably due to the difference in allowable strain to failure of the matrix when compared to the glass mat. Note that the glass fibers will fail in a brittle fashion, however, as they debond from the matrix the response will be an increase in strain. The rapid increase in strain followed by failure leads to the conclusion that there is a transition from matrix dominated properties to fiber/matrix interface dominated properties. Therefore, the fibers parallel to the loading direction are the final load bearing component prior to complete failure under fatigue loading.

8.3 C-Scans

The observation of C-scans for virgin specimens, before and after failure showed an increase in its attenuation. The scattering of energy due to the introduction of damage causes the increase in attenuation either in the form of matrix cracking, fiber/fiber debonding, fiber/matrix debonding, or fiber breakage. The increase in attenuation is associated with a decrease in the color range value. The attenuation as shown in Figure 18 suggests that damage in this material is distributed over the entire cross-section. The limiting factor in the evaluation of attenuation is the size and shape of the flaw. If the defect, in the specimen, is smaller than the wavelength then the imperfection will not be detectable do to its size relative to the wavelength. Therefore, if the shape of the crack relative to the ultrasonic pulse is smaller than the wavelength the crack, again, will go undetected.

8.3.1 Ultrasound approach to Damage

Representative C-scan images presented in Figure 29and Figure 30 provides only a qualitative comparison between samples. The potential of C-scan as an NDE technique to study distributed damage hinges on quantification of the images. The quantification of

C-scan images enables an investigation of distributed damage in a progressive manner. The use of digitized data in conjunction with image analysis produces a color range value that when related to damage shows a general decrease. A decrease in color range is due to an increase in attenuation. While an increase in attenuation is caused by the introduction of damage either in the form of matrix cracking, fiber/fiber debonding, or fiber/matrix debonding. This method is only effective if the same areas scan can be matched. Figure 29 shows tensile specimen P7-0-29's digitized C-scan results for the initial state, and incremental loads, in percentages of the ultimate tensile strength, of 20% UTS, 40% UTS, 60% UTS, and 80% UTS, respectively. As loading increased, there was a shift to darker grayscale. Shown in Figure 30 are the C-scan results for tensile specimen P7-0-30. Again, the progressive shift to a darker grayscale is observed. Because the same area for each sequential loading can be obtained, an image analysis was performed. This analysis measured the average color range in grayscale for matched areas of incrementally loaded specimens. This value was then plotted against percent loading. The results as shown in Figure 31 p. 83 exhibited a general trend towards a decreasing color range value, which corresponded to an increase in damage.

8.3.2 Tensile Mechanical Response

The results obtained from tensile measurement supported the ultrasound data. The mechanical response in tension is similar to the C-scan results when comparing the onset of change in attenuation with changes in the modulus reduction. It is clear from ultrasound that an increase in attenuation occurred between 20%-40% UTS. From Figure 24, which is a representative curve for tensile loading, a departure from linearity occurred at approximately 30% - 40% UTS. Therefore, the onset of damage occurred around 30% of UTS. The relative degree of damage at 100% of the UTS as indicated by modulus reduction is ~20% and is supported by the AGV results where the relative degree of damage was determined to be 29%.

8.4 Evaluation of Fracture Toughness

The ability to predict a materials response to loading conditions is an advantage for the design engineer and scientist. The designer of rigid structures is generally concerned with macroscopic properties such as strength and stiffness. These two aspects have therefore been studied to great extent in composite research by Hull, Folkes, and others.[69,70] However, the fracture toughness, K_{IC}, evaluated using **Linear Elastic Fracture** Mechanics, **LEFM**, is also important in engineering materials. In order to apply LEFM to composite materials an essential requirement is that the material must accrue damage under load without failing catastrophically yet not undergo yielding. The LEFM approach will be used here due to the brittle nature of this matrix material, hence, the material meets the LEFM requirements.

In most polymer composite cases, K_{IC} is a difficult parameter to obtain and has no simple correlation to bulk properties, strength and stiffness. The difficulty in evaluating the fracture toughness, K_{IC} , for composite materials is due to the localized events that occur in front of the growing crack in the composite. These localized events alter the crack tip stress field, hence, the fracture toughness prediction. Therefore, the evaluation of K_I cannot be conducted using the traditional approach of a single crack perspective due to the random void and fiber content of the CSMC.

The methodology for predicting K_{IC} for composites has not been approached, as determined to date, using combined K-solutions formulated by Tada, Paris, and Irwin.[23] The work conducted by Tada for the interpretation of K_I for a variety of possible crack configurations is compiled in Tada's handbook and presented in section "7.7 Mathematical Approach to Fracture Toughness, K_{IC}". [71] This compilation contains what is known as K-solutions. The usefulness of K-solutions is that a variety of solutions exist and can be combined mathematically to obtain a single expression that describes the stress field of a growing crack in the presence of other cracks. Therefore, the use of K-solutions that are associated with parallel and in-line crack configurations can be applied to this CSMC. There are two consideration necessary in describing the fracture parameter for this composite using K-solutions, defect size and applied stress.
The challenge associated with this approach is the observation and measurement of defect size. From preliminary images, obtained from video microscopy, it is evident that the cross-section is not only composed of fiber and matrix, but is also inhabited by voids. These voids depending on their size and density in a given region can and do act as stress risers.

The following figures and equations describe the approach for evaluation of the fracture parameter, K_I. The void/crack configurations used to develop a single fracture expression are shown in Figure 57 and Figure 58. In Figure 57 the geometry associated with the parallel crack configuration is shown. The mathematical evaluation of K_I for this arrangement is shown in Equation 23, Equation 24 and Equation 25. While Figure58

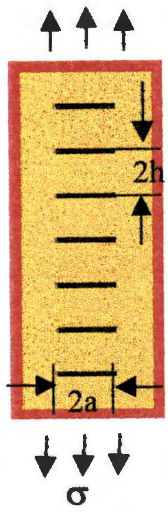

Equation 23. $$K_I = \sigma\sqrt{\pi a}F(s)$$

Equation 24. $$F(s) = \sqrt{\frac{1-s}{\pi s}}$$

Equation 25. $$s = \frac{a}{a+h}$$

2a = average void length
h = average distance between voids

Figure 57. Parallel cracks.

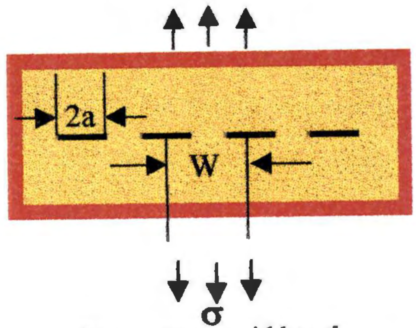

2a = average void length
W = the mean distance between voids

Equation 26. $$K_I = \sigma\sqrt{\pi a}\sqrt{\frac{W}{\pi a}\tan\frac{\pi a}{W}}$$

Figure 58. In-line cracks

is the in-line formation of voids/cracks followed by Equation 26, which is the expression for K_I for this arrangement.

In both cases K_I is dependent on crack length, 'a', applied stress, 'σ', and average separation between voids, 'W' for in-line and 'h' for parallel configurations. The interpretation of crack length and distance between cracks is determined from images obtained and calibrated from microscopy. The voids major and minor axis and distance between adjacent voids were used for the crack length and average separation between cracks, respectively.

The combining of these two expressions, Equation 23 and Equation 26, is a result of recognizing that both expressions contain the solution for a thru crack, $\sigma\sqrt{\pi a}$, multiplied by a geometry correction factor, F(s) and for parallel and in-line configurations, respectively. Therefore, by multiplying the thru-crack solution by both correction factors result in the final expression, Equation 27, and is the expression that will be used to evaluate, K_I for this CSMC. This equation is essentially an average effect of the distributed voids in an array of parallel and inline cracks having an average void size and distance between voids.

$$\boxed{K_I = \sigma\sqrt{WTAN\left(\frac{\pi a}{W}\right)}F(s)}$$

Equation 27.

As shown in Equation 27, which yields a probable value for K_{IC} can then be rewritten using the stress obtained from Equation 21. Equation 21 is used because it is believed to better describe the stress state of this system. The effective load due to the presence of voids is dealt with mathematically by introducing D_θ^W. The D_θ^W accounts for the orientation of the voids, which acts on the stress. In this case, the random orientation is assumed to corresponds to a θ=45°. Therefore, Equation 27 becomes

$$\boxed{K_{IC} = \sigma_{BC}\sqrt{WTAN\left(\frac{\pi a}{W}\right)F(s)D_{\theta}^{W}}}$$

Equation 28

where: $\mathbf{D_{\theta}^{W} = \cos^2(\theta)}$

The experimental results for the evaluation of K_{IC} resulted in an average value of 17.1 MPa√m, where the predicted results, shown in Figure 47, at 25°, 30°, and 45° at 40% glass fiber content and 12% void volume is 11.4 MPa√m, 17.0 MPa√m and 18.6 MPa√m, respectively. These predicted results suggest that there is some preferred orientation in the glass mat corresponding to approximately 30° of the major axis relative to the applied load rather than the assumed 45° angle. The most interesting note to make about the prediction equation is that by using two equations designed to individually describe a homogeneous system when combined mathematically has great probability in evaluating a heterogeneous system.

8.5 Fracture Toughness Prediction

Shown in Figure 59 are predictions of K_{IC} for various void orientations from 0°-90° relative to the applied. Other sample parameters necessary for the calculation were void spacing with a 0.001 m mean distance between in-line voids, 0.001 m as the average distance between parallel cracks and a sample thickness of 0.003 m. The stresses used for the fiber and matrix are 1700 MPa and 70.3 MPa respectively. The void volume, V_v, was 12% and σ_m* was 5.0 MPa. Equation 21 was used to evaluate the breaking stress.

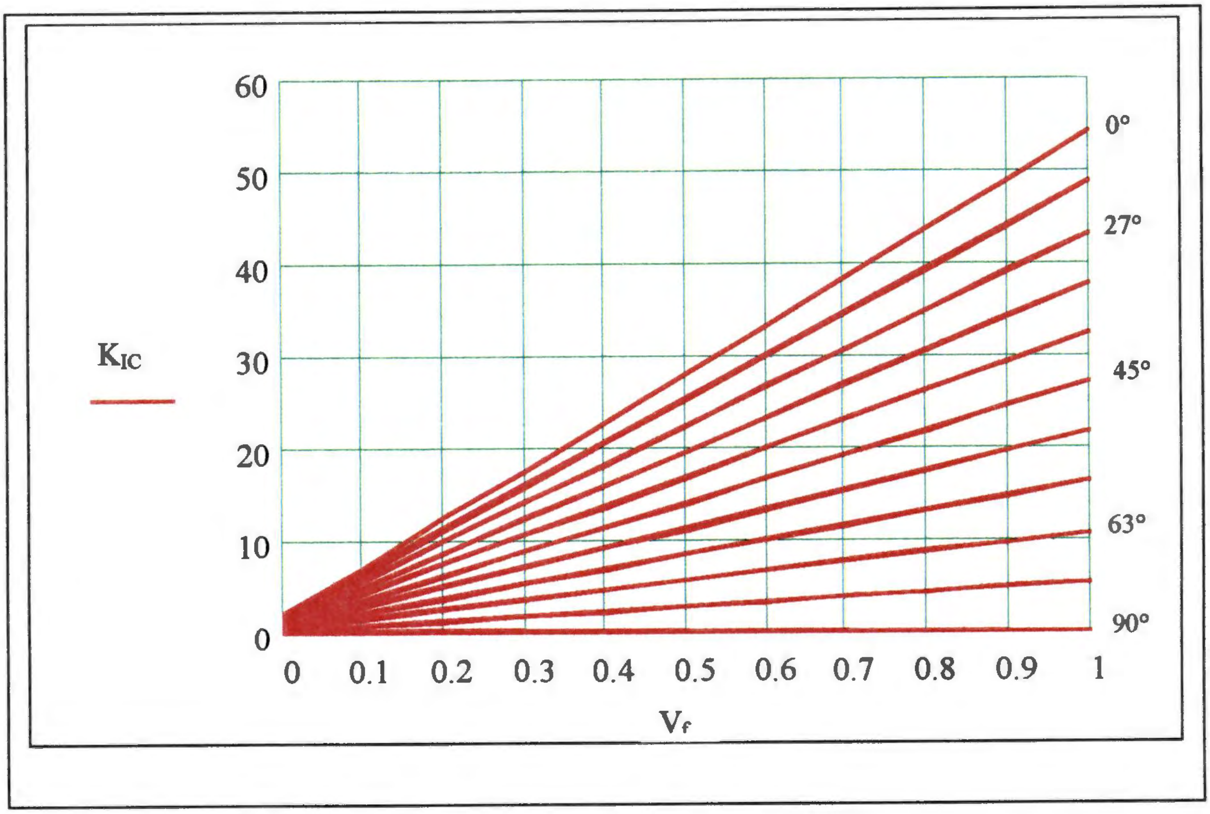

Figure 59. Fracture toughness as a function of fiber fraction, void orientation and a constant void volume of 12%.

Therefore, it is shown that the expected K_{IC} value ranges from 0.950 to 26 MPa√m for an angle theta of 45° using Equation 22. Theta is the angle between the void major axis and the applied load, and is assumed to be 45° due to the random orientation of voids. For the system at approximately 40% glass fiber, which this CSMC is, it is expected to yield a K_{IC} value of 11.4 MPa√m. However, looking at a range of possible orientations of voids as shown in Figure 59 the K_{IC} value could range from 0 to 22.8 MPa√m at a glass content of 40%. Shown in Table 5 are predicted values of K_{IC} at 40% for other possible angles of void orientation, which shows that as theta increases there is a decrease in the predicted value of K_{IC}.

The random orientation of the mat was assumed to produce a random orientation of voids that could be represented using an angle theta of 45°, however, what would be the expected response of K_{IC} at different void orientation, void content and fiber content. Shown in Figure 46 is a three dimensional plot that indicates the expected change in K_{IC} with changes in void orientation, void content and fiber content. K_{IC} is shown to increase with a decrease in the angle between the applied load and the long axis of the voids. There is also an increase in K_{IC} with an increase in fiber content. The effect of increasing the void content at constant fiber fraction results in a decrease in K_{IC}, this is shown in further detail Figure 47 to Figure 50 and . Therefore, by slight changes in theta there is a corresponding change in K_{IC}, which leads to the idea that 45° may not be the best representation for void orientation. By looking at a glass fiber content of 40%, void content of 12% and a theta of 30° and 25° a K_{IC} value of 17.0 MPa√m and 18.6 MPa√m would be achieved, respectively. The experimentally determined value on average was

Table 5. Variation of K_{IC} With Void Angle.

K_{IC} (MPa$\sqrt{m}$)	Angle (deg)
22.8	0
20.6	18
18.3	27
16.0	33
13.7	39
11.4	45
9.15	50
6.86	57
4.58	63
2.30	72
0	90

17.1 MPa$\sqrt{m}$, which suggests that there may be some preferred orientation in void content equivalent to approximately 30° relative to the applied load.

A final comparison is the predicted K_{IC} value at zero (0) fiber content and zero (0) void content to other homogeneous systems and is shown in Figure 60. At the above stated condition, the predicted K_{IC} value ranged from 1.1 - 1.9 MPa$\sqrt{m}$. Polyester, Epoxy and Polyethylene have K_{IC} values of 0.6 MPa$\sqrt{m}$, 0.6 MPa$\sqrt{m}$ and 1.0 - 6.0 MPa$\sqrt{m}$, respectively. While 50% glass filled polyester had a K_{IC} of 42 - 60 MPa$\sqrt{m}$.[72] The values obtained form literature for K_{IC} of different homogenous systems when compared to the CSMC's matrix and the comparison of the glassed filled polyester system suggests that the developed equation for K_{IC} has great potential as a empirical tool for predicting K_{IC}.

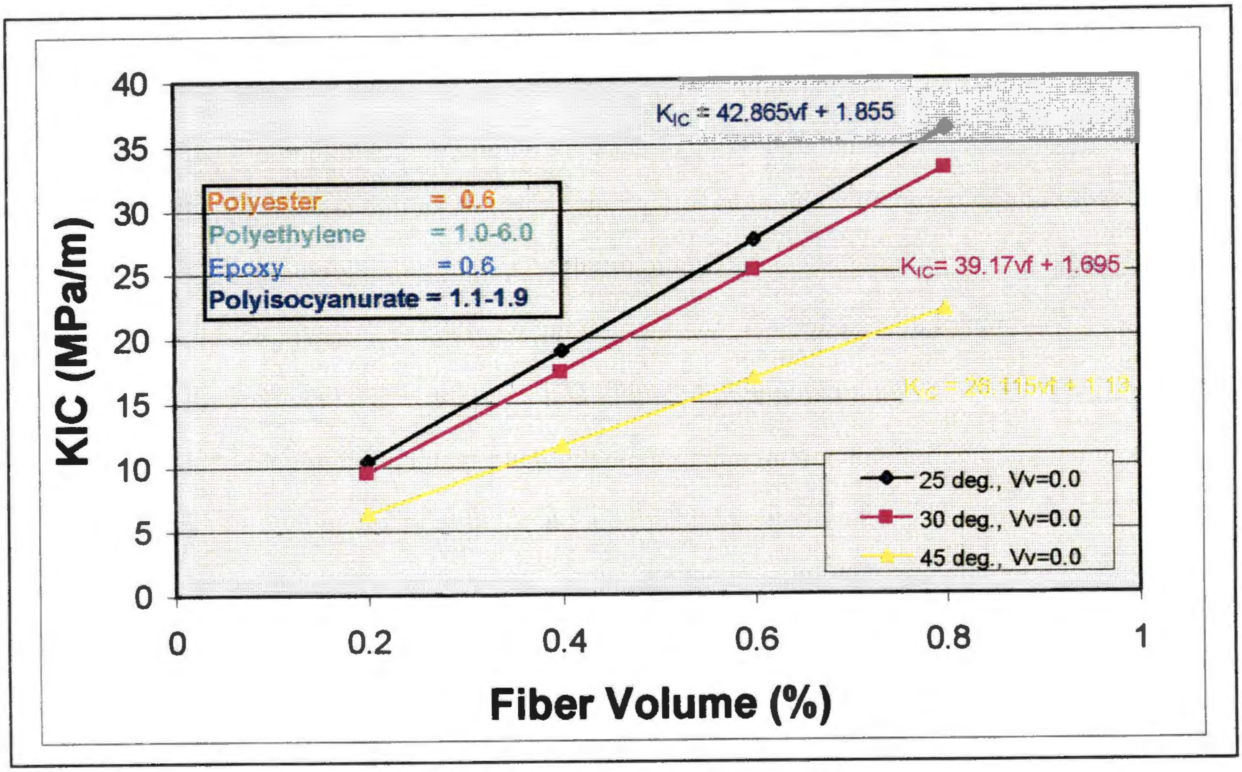

Figure 60. Comparison of Polyisocyanurate K_{IC} with Polyester, Epoxy and PE.

IX. CONCLUSIONS

The useful employment of the research issues provided herein is one aspect of dealing with damage and its progression in CSMC. This research showed:

- Damage can be identified using real-time video recording in conjunction with light microscopy. The observable damage was in the form of matrix cracking, fiber/matrix debonding, fiber breakage and fiber pullout.
- The progression of damage can be evaluated using ultrasonic C-scans by examining the initial state of the sample followed by repeat examination after the specimen has undergone loading. The obtained C-scans can then be quantified using the Average Grayscale Value method developed in this research.
- The use of the Rule of Mixture for the evaluation of breaking stress and the combining of K-solutions for in-line and parallel crack configurations provided a mathematical tool for the prediction of the Linear Elastic Fracture Mechanics parameter, K_{IC}, for this continuous swirl mat composite.

X. FUTURE WORK

- Apply prediction to a series of fiber volume fractions, and other material systems.
- Determine if the frequency emitted when a damage event occurs can be correlated with degree of damage using acoustic emissions.
- Determine what other material characteristics can be applied to the present prediction to reduce the percent difference.
- Determine the correlation between fiber and void orientation on K_{IC}.

LIST OF REFERENCES

LIST OF REFERENCES

[1] SPI Composite Institute.

[2] Modern Plastics, Nov. 1997, v. 74, no. 12

[3] Schwartz, M.M. Composite Materials Handbook, McGraw-Hill 2.35, 1.10-15, 2.29 (1984).

[4] Peter J. McCamley, "Modern Plastics Encyclopedia Handbook", p.128, McGraw Hill, 1994.

[5] R.J Diefendorf and E.W. Tokarsky, "The Relationships of Structure to Properties in Graphite Fibers, Part I," AFML-TR-72-133, Air Force Materials Laboratory, 1971.

[6] R.E. Wilfong and J. Zimmerman, Strength and Durability Characteristics of "Kevlar" Aramid Fiber, J.Apl. Polym. Sc., 31st Applied Polymer Symposium, John Wiley & Sons, 1977, p 1-21

[7] Willard D. Bascom, University of Utah, Other Continuous Fibers, Engineering Materials Handbook, Vol. 1, 1987 p 117-118.

[8] D.E. Campbell and H.E. Hagy, Glass and Glass-Ceramics, in Handbook of Material Sciece, Vol II, CRC Press, 1975, p. 323-338

[9] W.W. Wolf and S.L. Mikesell, The Glass Fiber Industry-- The Reason for the Use of Certain Chemical Compositions," Seminar presented at University of Illinois, Urbana, IL, Oct 1982.

[10] J.G. Mohr and W.P. Rowe, Fiber Glass, Van Nostrand Reinhold Company, 1978, p. 207

[11] P.F. Aubourg and W.W. Wolf, "Glass Fibers-Glass Composition Research" Paper presented at Glass Division Meeting, American Ceramic Society, Grossinger, NY, Oct 1984.

[12] David M. Miller, "Glass Fibers", Composites ASM International vol. 1, p. 45, 1987

[13] A. rose and E. Rose, Ed., The Condensed Chemical Dictionary. 6th ed., Reinhold, 1956, p 497.

[14] M. Basche, Interfacial Stability of Silicon Carbide Coated Boron Fibalment Reinforced Metals, in Interfaces in Comoisites, STP 452, American Society for Testing and materials, 1968, p 130

[15] J. B. Donnet and R.C. Bansal, Carbon Fibers, Marcel Dekkaer, 1985.

[16] W.D. Bascom, Structure of Silane Adhesion Promoter Films on Glass and Metal Surfaces, Macromlecules, Vol 5, 1972, p.792

[17] H. Ishida and Y. Suzuki, Hydrolysis and Condensation of Aminosilane Coupling Agents in High Concentration Aqueous Solutions: A Simulation of Silane Interphase, in Composite Interfaces, H. Ishida and J.L. Koenig, Ed., North Holland, 1986

[18] K. Hoh, H. Ishida, and J.L. Koenig, The Diffusion of Epoxy Resin Into a Silane Coupling Agent interphase, in Composite Interfaces, H.Ishida and J.L. Koenig, E., Elsevier, 1986, p 251

[19] Willard D. Bascom, Fiber Sizing, p 121-123 Composites ASM International vol. 1, p. 122-124.

[20] "Encyclopedia of Polymer Science and Engineering", Vol. 12, Wiley Interscience Pub., John Wiley & Sons New York, p.418 (1985)

[21] Schwartz, M.M. Composite Materials Handbook, McGraw-Hill 2.35, 1.10-15, 2.29 (1984).

[22] S. W. Tsai, Mechanics of Composite Materials, Air Force Materials Lab. Rept. AFML-TR-66-149 (1966)

[23] Christopher W. Macosko, "RIM Fundamentals of Reaction Injection Molding", Hanser Publishers, (1989) Chapter 1.

[24] W.S. Pellini, Principles of Structural Integrity Technology, office of Naval Research, 1976.

[25] J. N. Yang, R.K. Miler, and C.T. Sun, Effect of High Loads on Statistical Fatigue of Unnotched Graphite/Epoly Laminates, J. Compos. Mater., Vol 14, 1980 p 82-94.

[26] Delasi, R., and Whiteside, J.B. 1978, " Effects of Moisture on Epoxy Resins and Composites," ASTM STP 658, American Society for testing and materials, Philadelphia p 2-20.

[27] D. C. Worley II, P.K. Liaw, R.S. Benson, W. A. Simpson Jr., J. M. Corum, "Microscopy and Ultrasound as an NDT Technique for Polymer Composites", Cincinnati, OH. TMS, 1996.

[28] Engel, L., H. Klingele, G. W. Ehrenstein, and H. Schaper. An Atlas of Polymer Damage, Wolfe Publishing, 114, 190, 226, 193, 230, 177, 188 (1981).

[29] Karger-Kocsis, J. and T. Czigany. J. Materials, 28:2440 (1993)

[30] Karger-Kocsis, J. and Zs. Fejes-Kozma. *Mechanics of Composite Materials*, v. 30, no. 1, 8-13 (1994)

[31] Karger-Kocsis, J. *Journal of Applied Polymer Science*, v. 45, 1595-1609 (1992)

[32] Fejes-Kozma, Zs. And J. Karger-Kocsis. *Journal of Reinforced Plastics and Composites*, v. 13, 823-834 (1994)

[33] Czigany, T. and J. Karger-Kocsis. *Polymer and Polymer Composites*, v. 1, no.5, 329-339 (1993)

[34] Karger-Kocsis, J. *Journal of Materials Science Letters*, v. 13, 1422-1425 (1994)

[35] V.K. Stokes, "Random Glass Mat Reinforced Thermoplastic Composites", Part I, "Phenomenology of Tensile Modulus Variations.", Polymer Composites 11 (1) 32-44.

[36] V.K. Stokes, "Random Glass Mat Reinforced Thermoplastic Composites", Part II, "Analysis of Model Material.", Polymer Composites 11 (1) 45-55.

[37] V.K. Stokes, "Random Glass Mat Reinforced Thermoplastic Composites", Part III, "Characterization of Tensile Modulus.", Polymer Composites 11 (6) 342-353

[38] J. Karger-Kocsis, "Dynamic Fracture Mechanics of a RIM Polyamide Block Copolymer Reinforced with a Glass Strand Mat" Poly, Bull. v. 24, 341-348, 1990.

[39] J. Karger-Kocsis, "Fracture and Failure Behavior of Glass Fiber Mat Reinforced Structural Nylon RIM Composites", Journ. Polymer Engr. 11(2), 153-173.

[40] C.A. Bergund and M. L. Ericson in Polypropylene: Structure Blends and Composites", Chapman & Hall, London, 1994, Chpt. 21.

[41] J. Karger-Kocsis, Poly, Bull., v. 31, 235 (1993).

[42] J. Karger-Kocsis and Z. S. Fejes-Kozma, J. Reinf. Plast. Compos., v. 13, 122 (1994).

[43] M.J. Owen and R.J. Howe " The Accumulation of Damage in a Glass-Reinforced Plastic Under Tensile and Fatigue Loading.", J. Phys. D:Appl. Phys. Vol. 5, 1972.

[44] R.J. Howe and M.J. Owen "Cumulative Damae in Chopped Strand Mat/Polyester Resin Laminates", University of Nottingham, UK. 1972.

[45] M.J. Owen, T.R. Smith, and R. Dukes, "Failure of glass reinforced plastics, with

special reference to fatigue", Plastics and Polymers JUNE 1969.

[46] Corum, J. M. "Durability of Lightweight Composite Structures for Automotive Application: Annual Progress Report for period ending Sept 30, 1995", Oak Ridge National Laboratory (Mar. 1996).

[47] Corum, J. M. "Durability of Lightweight Composite Structures for Automotive Application: Annual Progress Report for period ending Sept 30, 1996", Oak Ridge National Laboratory, 1-30, 1-31 (Jan. 1997).

[48] Anders, O.U. *SAMPE Technical Conference,* v. 23, 1084-1087 (Oct. 21-24, 1991)

[49] Huang, X. and R.R. Bresee. *INDA J. Nonwovens Research,* v.5, no. 1-3; v. 6, no.4 (1993, 1994).

[50] Bradley, G. F., Jr. "Electron Beam Charging of Polymers in a Scanning Electron Microscope" Master's Thesis, The University of Tennessee, Knoxville, TN, 12 (1992).

[51] Goldstein, J. I., et al. Scanning Electron Microscopy and X-Ray Microanalysis, Plenum Press, 91, (1992).

[52] Martuscelli, E., R. Palumbo, and M. Kryszewshi, "Polyer Blends Processing, Morphology and Properties", Plenum Press, New York p.25 (1979)

[53] Utracki, L., "Polymer Alloys and Blends", Thermodynamics and Rheology", Hanser Publishers, Munich p.13 (1983)

[54] Griffith, A. A. Phil. Trans. Roy. Soc. London A 1921, 221, 163.

[55] Griffith A. A. Proc. 1st Int. Congress. Appl. Mech. 1924, 55.

[56] Inglis, C.E. Proc. Inst. Naval Architects 1960,60.

[57] Bartenev, G.M.; Zuyev, Y.S. Strength and Failure of Visco-elastic Materials;Pergammon: Oxford, 1968.

[58] Orowan, E. Phys. Soc. Rep. Prog. Phys. 1948, 12, 186.

[59] Irwin, G.R. Fracture, Handbuck der Physick VI, Flugge Ed., Springer: Munich, 1958, p. 551-590.

[60] Westergaard, H.M. J. Appl. Mech. 1939, 61, A49.

[61] Broek, D. Elementary Engineering Fracture Mechanics, 4th ed.; Martinus Nijhoff: Dordrecht, 1986.

[62] H.Tada, P. Paris, and G. Irwin, " The Stress Analysis of Cracks Handbook", Del Research Corporation, Hellertown, Pennsylvania, 1973.

[63] ORNL Publication, Engineering Technology Division, 1998.

[64] Klaus, F. "Fracture mechanical Behavior of Short Fiber Reinforced Thermoplastics", Fortschritt-berichte der VDI Zeitschriften, no. 18, vol 18, 1984.

[65] A.F. Johnson, "Engineering Design Properties of GRP", BPF Reinforced Plastics Group, p. 21-35 1973.

[66] S. W. Tsai, "Fundamental Aspects of Fiber Reinforced Plastic Composites", Interscience Publishers, p. 3-10, 1968.

[67] Kanninen, M.F., Rybicki, E.F., and Brinson, H.F.: Composites, 8 (1977), 17.

[68] W.D. Dascom, D.J. Foll, B. Fuller, P.J. Phillips, "Fractography of the interlaminar fracture of carbon-fibre epoxy composite", Journal of Mat. Sci. 20 p. 3184-3190, 1985.

[69] Hull, D., An Introduction to Composite Materials, Cambridge University Press, Cambridge (1981)

[70] Folkes, M.J., Short Fiber Reinforced Thermoplastics, Research Studies Press, Letchworth (1982)

[71] H.Tada, P. Paris, and G. Irwin, " The Stress Analysis of Cracks Handbook", Del Research Corporation, Hellertown, Pennsylvania, 1973.

[72] Richard A. Flinn, Paul K. Trojan, "Engineering Application and Their Applications", Houghton Mifflin Company, p 660-662, 1990.

APPENDIX

Appendix A

SAMPLE
calculation from experimental results

Variables obtained from microscopy and caliper or micrometer measurements:

$P = 857.62$ N
$a = 0.013$ m
$B = 0.003$ m
$B_N = 0.003$ m
$W = 0.025$ m

The following calculation takes care of the geometry affect, and is called the geometry correction factor.

$$\boxed{f\left(\frac{a}{w}\right) = \frac{\left[\left(2+\left(\frac{a}{w}\right)\right)\left[0.886+4.64\left(\frac{a}{w}\right)-13.32\left(\frac{a}{w}\right)^2+14.62\left(\frac{a}{w}\right)^3-5.6\left(\frac{a}{w}\right)^4\right]\right]}{\left(1-\left(\frac{a}{w}\right)\right)^{\frac{3}{2}}} = 10.331}$$

K_Q is equivalent to K_{IC}. This equivalency can only be done when $P_{max}/P_Q \leq 1.10$.

$$\boxed{K_Q = \frac{P}{\left(BB_N W\right)^{\frac{1}{2}}} f\left(\frac{a}{w}\right) = 18.67 MPa\sqrt{m}}$$

SAMPLE
calculation from predictive results

Variables obtained from microscopy and caliper or micrometer measurements:

$\sigma_{bf} = 1700$ MPa
$\sigma_{bm} = 70.3$ MPa
$\pi = 3.141592$
a = 0.00009 m
h = 0.001 m
W = 0.001 m
$V_f = 0.4$
$V_v = 0.12$
$\theta = 45°$

The following calculation is a geometry correction factor, which takes into consideration the configuration of cracks.

$$\boxed{s = \frac{a}{a+h}}$$

$$\boxed{F(s) = \sqrt{\frac{1-s}{\pi s}}}$$

Next, calculate the prediction of the composite's breaking stress
from the
"Rule of Mixtures"

$$\boxed{\sigma_{BC} = \sigma_{bf} v_f + \sigma_{bm}\left((1-V_v)-V_f\right)}$$

The Prediction of KIC is then obtained using the following equation;

$$\boxed{K_{IC} = \sigma_{BC}\sqrt{WTAN\left(\frac{\pi a}{W}\right)}F(s)D_\theta^W = 11.4MPa\sqrt{m}}$$

D_θ^W corrects for stress distribution for randomly oriented voids. This term comes from basic mechanics of materials for a distributed stress acting on a plane at some angle to the applied load

$$\boxed{D_\theta^W = \cos^2(\theta)}$$

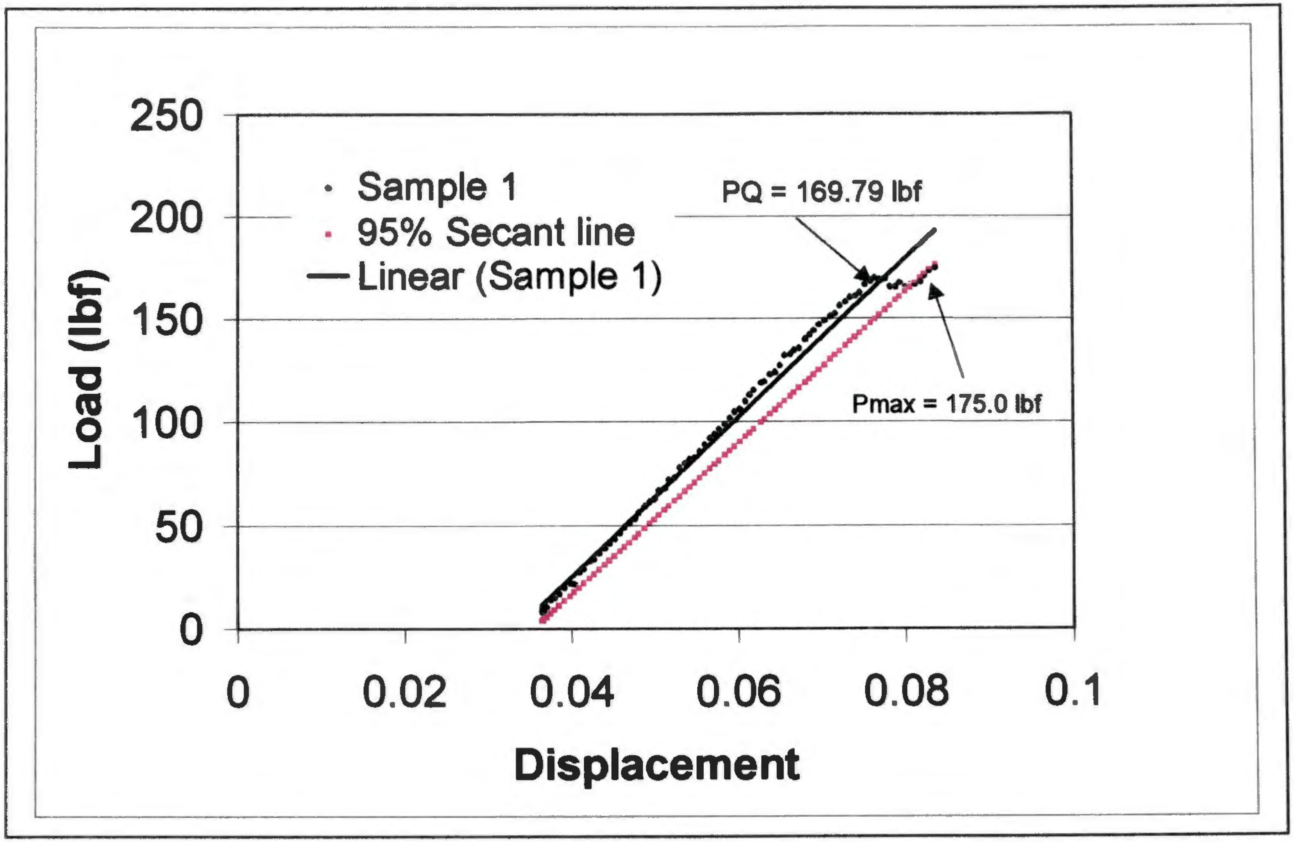

P_Q = 169.79 lbf
P_{max} = 175.0 lbf
KQ = 1.03

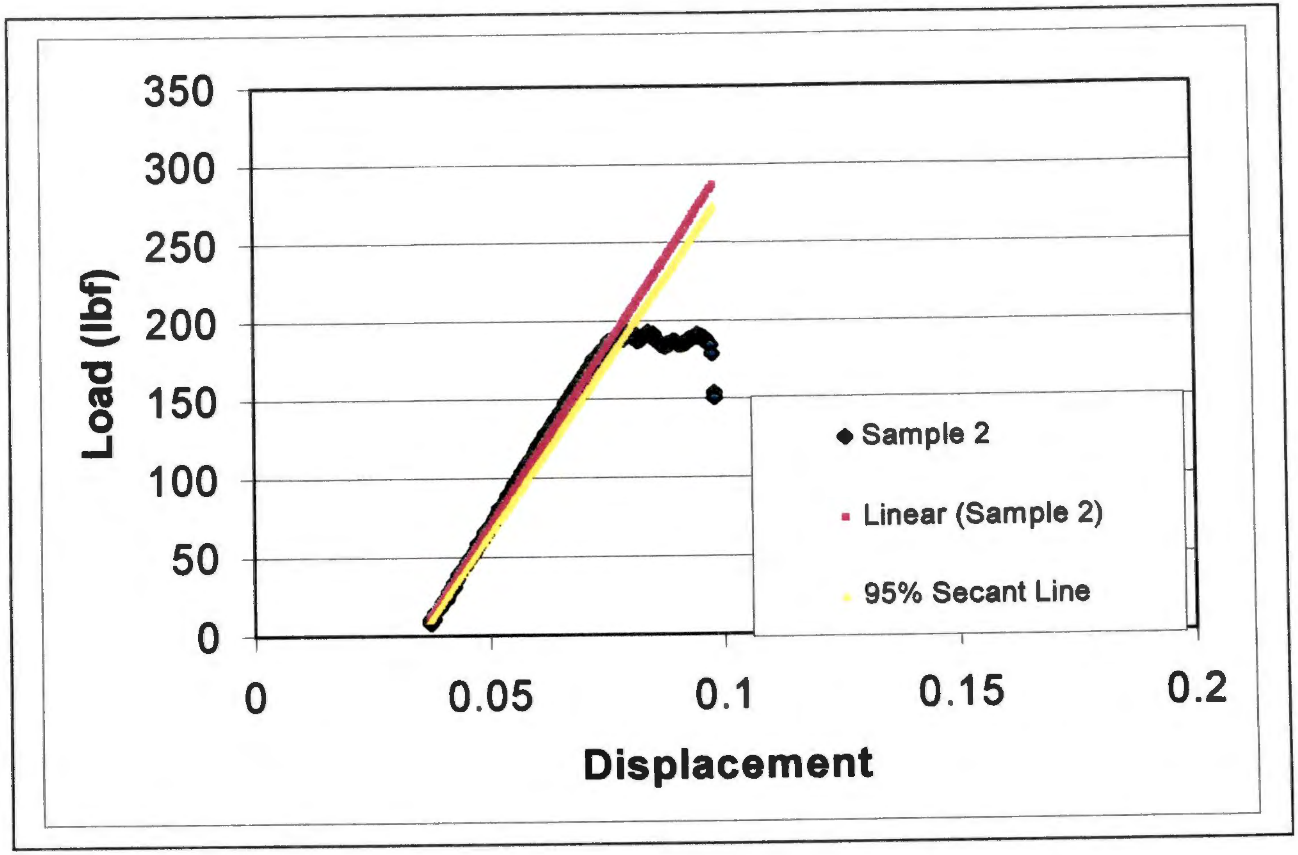

$P_Q = 192.8$ lbf
$P_{max} = 192.8$ lbf
$KQ = 1.00$

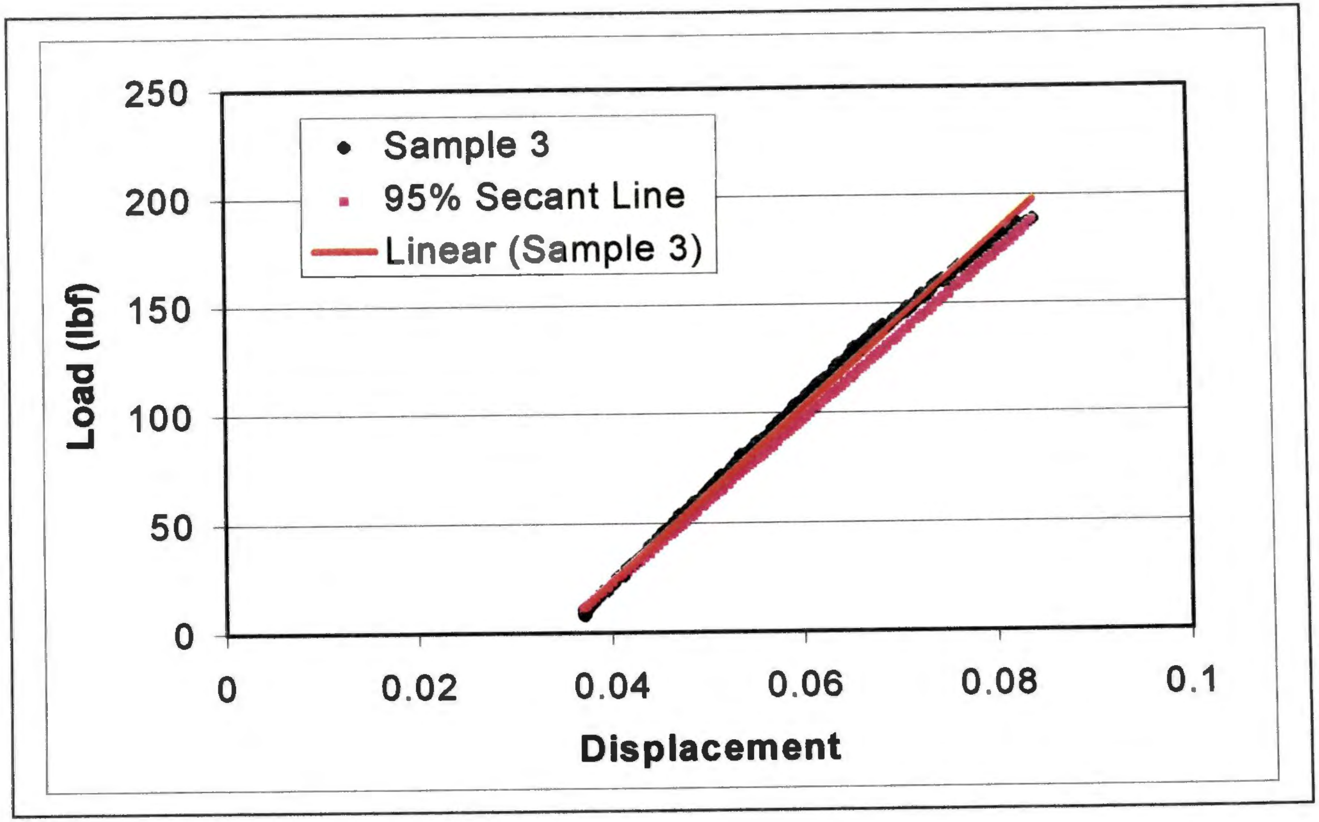

$P_Q = 188.7$ lbf
$P_{max} = 188.7$ lbf
$K_Q = 1.00$

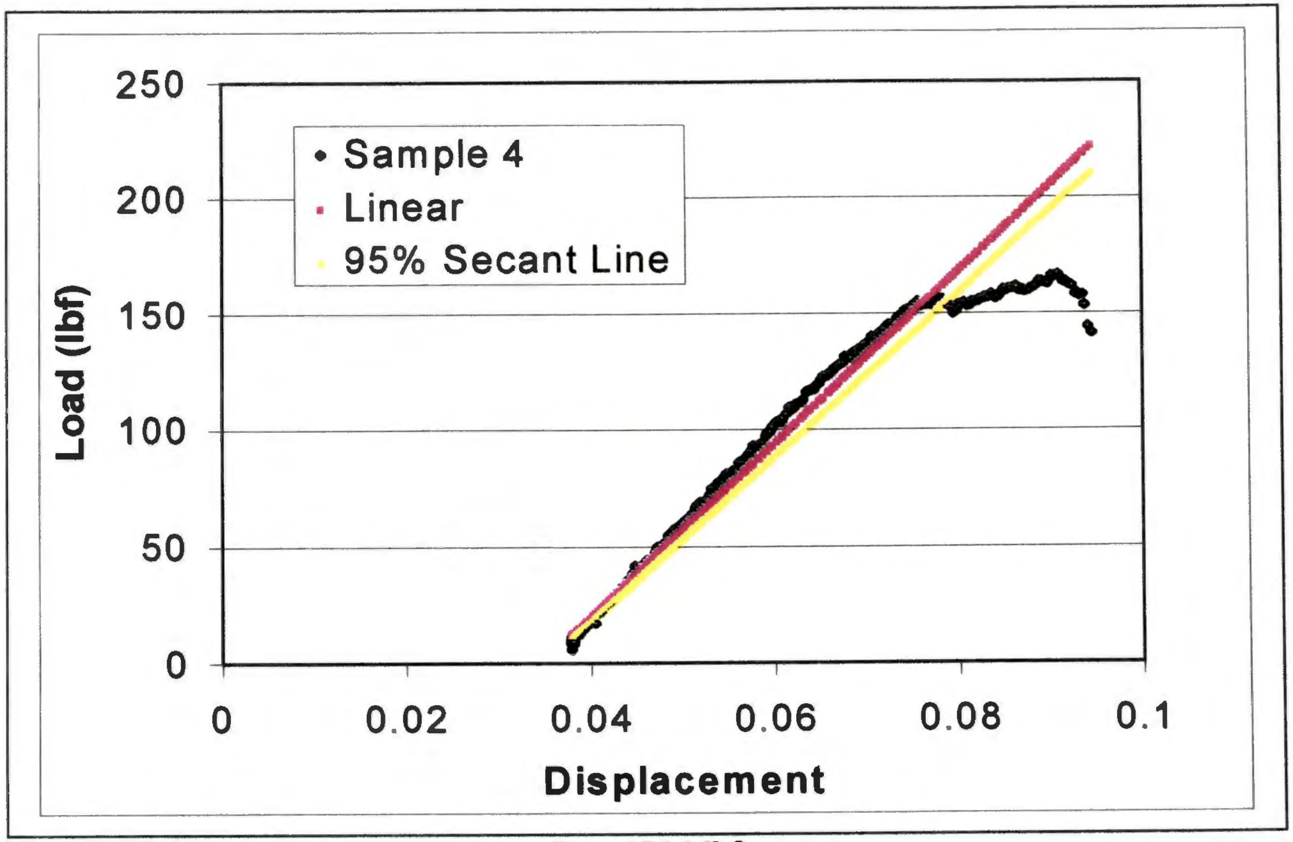

$P_Q = 156.0$ lbf
$P_{max} = 166.47$ lbf
$K_Q = 1.07$

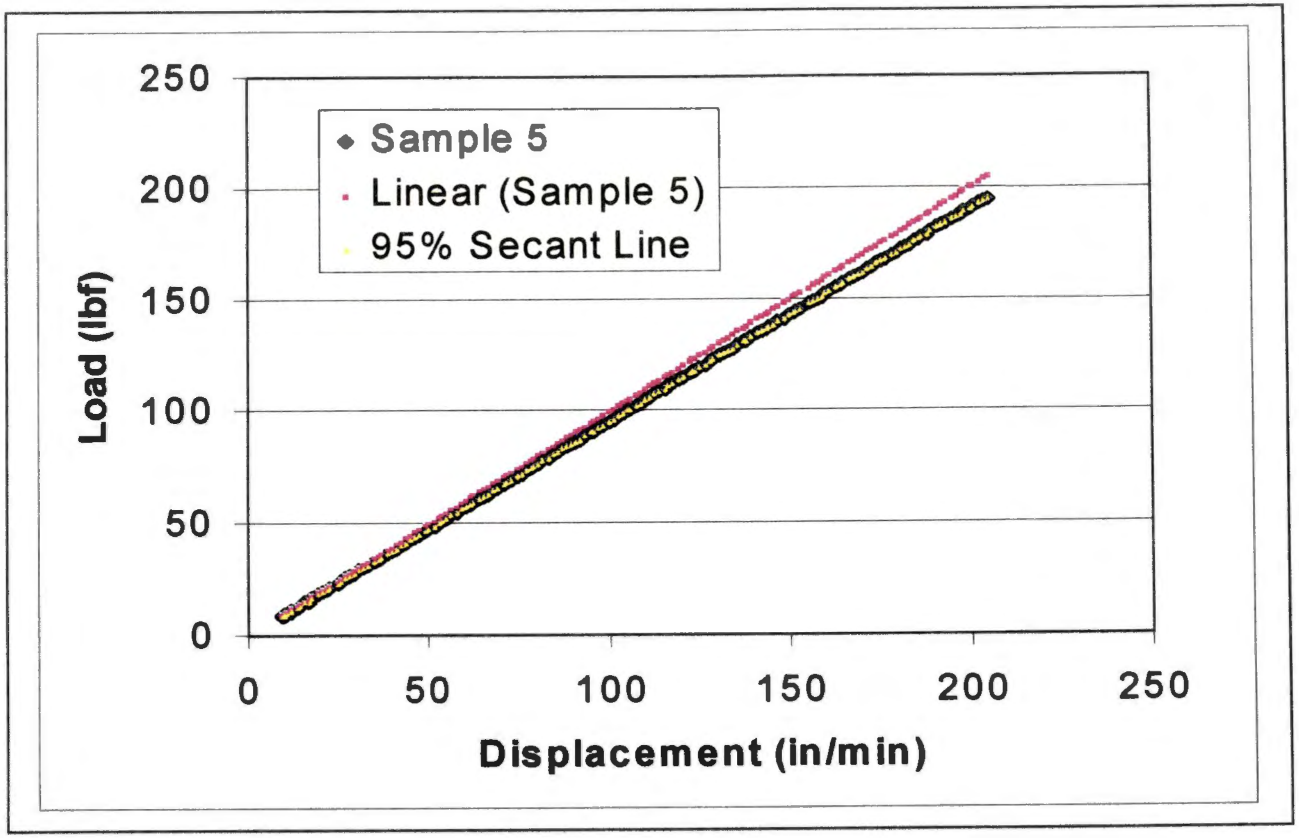

P_Q = 172.3 lbf
P_{max} = 172.3lbf
K_Q = 1.00

Appendix B

Sample Calculation
of Percent Void Volume

(b) in mm	(a) in mm	mm^3		(b) in mm	(a) in mm	mm^3
Major axis	Minor axis	Ellipse volume		Major axis	Minor axis	Ellipse volume
0.110	0.072	0.002		0.080	0.078	0.002
0.112	0.086	0.003		0.130	0.110	0.003
0.081	0.078	0.002		0.072	0.042	0.002
0.077	0.677	0.147		0.088	0.052	0.147
0.107	0.088	0.004		0.113	0.107	0.004
0.114	0.079	0.003		0.171	0.085	0.003
0.079	0.071	0.002		0.100	0.084	0.002
0.074	0.074	0.002		0.096	0.089	0.002
0.056	0.043	0.000		0.103	0.095	0.000
0.064	0.053	0.001		0.105	0.080	0.001
0.110	0.097	0.004		0.133	0.112	0.004
0.115	0.101	0.005		0.115	0.068	0.005
0.100	0.090	0.003		0.086	0.084	0.003
0.093	0.082	0.003		0.102	0.092	0.003
0.012	0.072	0.000		0.039	0.036	0.000
0.118	0.090	0.004		0.054	0.050	0.004
0.098	0.070	0.002		0.171	0.079	0.002
0.084	0.060	0.001		0.086	0.064	0.001
0.083	0.075	0.002		0.065	0.048	0.002
0.106	0.096	0.004		0.093	0.080	0.004
0.088	0.067	0.002		0.091	0.064	0.002
0.069	0.062	0.001		0.081	0.059	0.001
0.114	0.103	0.005		0.111	0.074	0.005
0.118	0.103	0.005		0.086	0.071	0.005
0.058	0.054	0.001		0.073	0.055	0.001
0.106	0.064	0.002		0.067	0.053	0.002
0.114	0.094	0.004		0.148	0.138	0.004
0.096	0.090	0.003		0.063	0.059	0.003
0.085	0.081	0.002		0.139	0.108	0.002
0.076	0.072	0.002		0.049	0.043	0.002

Number of Voids Present =	6
No. of slices for thickness =	3.84
0.005	**average void volume**
0.031	**volume of voids in a slice**
0.119	**Samples void volume**
11.9	**Percent Void Volume**

Appendix C

Graph data
obtained from K_{IC} prediction

Vf	Vv	25	30	45
0.1	0	6.14	5.61	3.74
	0.1	5.95	5.44	3.63
	0.2	5.77	5.27	3.51
	0.3	5.58	5.1	3.4
	0.4	5.4	4.93	3.29
	0.5	5.21	4.76	3.18
	0.6	5.03	4.6	3.06
	0.7	4.84	4.43	2.95
	0.8	4.66	4.26	2.84
	0.9	4.47	4.09	2.73
0.2	0	10.43	9.53	6.35
	0.1	10.24	9.36	6.24
	0.2	10.06	9.19	6.13
	0.3	9.87	9.02	6.01
	0.4	9.69	8.85	5.9
	0.5	9.5	8.68	5.79
	0.6	9.32	8.51	5.68
	0.7	9.13	8.34	5.56
	0.8	8.95	8.17	5.45
0.4	0	19.01	17.36	11.58
	0.1	18.82	17.19	11.46
	0.2	18.64	17.02	11.35
	0.3	18.45	16.86	11.24
	0.4	18.27	16.69	11.12
	0.5	18.08	16.52	11.01
	0.6	17.9	16.35	10.9
0.6	0	27.55	25.2	16.8
	0.1	27.37	25.03	16.69
	0.2	27.18	24.86	16.57
	0.3	27	24.69	16.46
	0.4	26.81	24.52	16.35
0.8	0	36.16	33.03	22.02
	0.1	35.98	32.87	21.9
	0.2	35.8	32.7	21.8
0.9	0	40.4	36.95	24.64
	0.1	40.22	36.78	24.52

Appendix D

Creep Data
Load Strain, Creep Strain
and
Total Strain

Creep Load (ksi)	Load Strain (%)	Creep Strain (%)	Total Strain (%)
16.0	1.42	0.28	1.70
15.5	1.24	0.4	1.64
14.5	1.20	----	1.20
10.0	0.66	----	0.66
5.0	0.29	----	0.29
2.5	0.10	0.12	0.22

VITAE

The author of this text was born in Frankfurt, Germany on March 25, 1966 to Mrs. Mitzi M. (Heibel) Worley and Darnell Carlton Worley. He graduated from Northeast High School in Clarksville, Tennessee. After graduation he attended the University of Tennessee at Knoxville in pursuit of a B.S. degree in Material Science and Engineering which was completed December 1991. A Masters Degree in Polymer Engineering was pursued under the Minority Graduate Fellowship. The research conducted addressed the characterization of crystalline-crystalline polymer blends and was completed July 28, 1994. A Ph.D. in Polymer Engineering at the University of Tennessee Knoxville was conducted under the Southern Regional Education Board Fellowship, and it is the research found herein completed in 1999. As of this date he has been married for four and a half years. A time for which he has truly been given a gift of a lifetime, LOVE.